October 2010

Atomic Force Microscopy for Better Probing Surface Properties at Nanoscale: Calibration, Design and Application

Yu Liu, *The University of Western Ontario*

Supervisor: Jun Yang, *The University of Western Ontario*

A thesis submitted in partial fulfillment of the requirements for the Doctor of Philosophy degree in Mechanical and Materials Engineering

Atomic Force Microscopy for Better Probing Surface Properties at Nanoscale: Calibration, Design and Application

(Spine Title: Atomic Force Microscopy Probing Surface Properties)

(Thesis Format: Integrated-Article)

By

Yu Liu

Department of Mechanical and Material Engineering

Faculty of Engineering

A thesis submitted in partial fulfilment

of the requirements for the degree of

Doctor of Philosophy

The School of Graduate and Postdoctoral Studies

The University of Western of Ontario

London, Ontario, Canada

THE UNIVERSITY OF WESTERN ONTARIO
School of Graduate and Postdoctoral Studies

CERTIFICATE OF EXAMINATION

Supervisor

Dr. J Yang

Co - Supervisory

Dr. J M Floryan

Examiners

Dr. S F Asokanthan

Dr. Z F Ding

Dr. G K Knopf

Dr. J T W Yeow

The thesis by

Yu Liu

entitled:

Atomic Force Microscopy for Better Probing Surface Properties at Nanoscale: Calibration, Design and Application

is accepted in partial fulfilment of the
Requirements for the degree of
Doctor of Philosophy

Date

Chair of the Thesis Examination Board

ABSTRACT

As one of most important imaging techniques in nanotechnology, atomic force microscopy (AFM) must be explored to characterize physical and chemical properties of materials.

To measure force by AFM with high resolution requires accurate calibration of optic – lever detection sensitivity and spring constant. On biological AFM force mode, the coupling effects of the liquid environment, spot size of laser beam and laser spot location on AFM cantilever backside, must be considered to correlate the static sensitivities from force curves in air and in liquid for calibration. An effective model has been developed first and experimentally elucidated to calibrate the static sensitivity in liquid. The proposed model eliminates inconvenience of static sensitivity calibration in liquid with possible contamination sources.

The static sensitivity based on force curve can not be directly applied on dynamic modes. The second part of our work analyzed optimization of the dynamic sensitivity of an AFM vibrating at different flexural modes. We have proposed a calibration method to determine the dynamic sensitivity by the force curve, and further developed amplitude sensitivity as the dynamic sensitivity at tapping frequency to calibrate the spring constant of the cantilever by the thermal method.

In contrast to the calibration at normal direction, there are main difficulties for the lateral sensitivity and spring constant of a cantilever. A new friction mode is developed in the third part to bypass the difficulties and directly measure friction force or friction coefficient instead, by applying a special T–shape cantilever. An effective method has been proposed to minimize possible errors with this friction mode. We also demonstrate the validation of the mode to distinguish hydrophobic and hydrophilic groups on nanoscale self assembled monolayers.

The final part of the thesis is organized to apply AFM as an efficient tool to characterize a low-energy hydrogen bombardment process. Physical properties of alkane thin film

have been studied before and after bombardment, including morphology and mechanical properties. AFM results reveals that the hydrogen bombardment process shows great potential in modification of morphological, mechanical and tribological properties of organic thin films for a broad range of applications, esp. on MEMS/NEMS devices.

KEYWORDS

Atomic Force Microscopy, Optical Lever Detection Sensitivity, Higher – order Flexural Mode, Tip – sample Interaction, Lateral Friction Force, Force Modulation, Torsional Tapping, Low-energy Hydrogen Molecule Bombardment

CO-AUTHORSHIP

This doctoral thesis has been prepared according to the regulations for an integrated-article format thesis stipulated by the Faculty of Graduate and Postdoctoral Studies at the University of Western Ontario and has been co-authored as follows:

CHAPTER 2: DETECTION SENSITIVITY OF AFM IN LIQUID

All the theoretical analyses and experiments were conducted by Y. Liu under the supervision of Dr. J. Yang. A draft of Chapter 2 was prepared by Y. Liu and reviewed by Dr. J. Yang. A paper co-authored by Y. Liu and J. Yang has been published in Nanotechnology.

CHAPTER 3: DETECTION SENSITIVITY OF DYNAMIC FLEXURAL AFM MODE

All the theoretical analyses and experiments were conducted by Y. Liu under the supervision of Dr. J. Yang. A draft of Chapter 3 were prepared by Y. Liu and reviewed by Dr. J. Yang. One paper co-authored by Y. Liu, Q.Q. Guo, H.Y. Nie, W.M. Lau and J. Yang has been published in Journal of Applied Physics. Another paper co-authored by S. Naeem, Y. Liu, H.Y. Nie, W.M. Lau and J. Yang has been published in Journal of Applied Physics.

CHAPTER 4: A NEW AFM NANOTRIBOLOGY MODE FOR FRICTION

All the theoretical analyses and experiments were conducted by Y. Liu under the supervision of Dr. J. Yang. A draft of Chapter 4 were prepared by Y. Liu and reviewed by Dr. J. Yang. K.M. Leung collaborated on preparation of the PDMS stamp according to Y. Liu's design. One paper co-authored by Y. Liu, K.M. Leung, H.Y. Nie, W.M. Lau and J. Yang has been published in Tribology Letters.

CHAPTER 5: AFM CHARACTERIZATION OF THIN FILMS UNDER LOW – ENERGY HYDROGEN BOMBARDMENT

All the theoretical analyses and experiments were conducted by Y. Liu under the supervision of Dr. J. Yang. A draft of Chapter 5 was prepared by Y. Liu and reviewed by Dr. J. Yang. One paper co-authored by Y. Liu, D.Q. Yang, H.Y. Nie, W.M. Lau and J. Yang has been submitted to ACS Applied Materials & Interfaces for review (Submission # am – 2010 – 005833).

ACKNOWLEDGEMENTS

The dissertation would not have been possible without the many people who took part in my life as a graduate student. They made this time special and memorable for me.

I would like to express sincere gratitude to Prof. Jun Yang, my immediate supervisor, for his introducing me into this fantastic research area. He is generous and patient for guiding me in the research from the beginning to the end. “Actions speak louder than words”, he always spoke to me. He provided me with friendly encouragement and assistance during my daily life.

I sincerely thank my co-supervisor Prof. J. M. Floryan. Without his careful proof and valuable comments, this thesis can not go for the final. Thanks to his dedicated organization on our department seminars, I can have the greatest opportunities to learn from other researchers, and present my personal researches and get wealthy feedback from others.

I am deeply indebted to Prof. Leo W.M. Lau for his continuous guidance in the industry project with LANXESS. He pioneered the design and development of low-energy hydrogen bombardment system. His expertises and valuable suggestions help me to finish my researches, esp. the topic related to application of atomic force microscopy.

I would like to express my sincere thanks to Dr. Heng-Yong Nie, who is a specialist on atomic force microscopy. He taught me how to understand phenomena in depth. Our up to four – year discussion on AFM helps me being familiar with the related techniques and trends.

My sincere thank goes to Dr. Derry Yang, who had a one-year close co-work with me in the industry project. Several aspects of my work there definitely came from his help and suggestion.

I would like to appreciate the help and friendliness from my colleagues. They are: Qiu-quan, Mei, Edmond, Jin-long, and Xue-yin.

Special thanks are given to my co-workers in the industry project: Fengzhou, Wei, Yan, Patrick, Solmaz, Colin, Jie and Jane.

I would like to appreciate the financial supports from National Science and Engineering Research Council, LANXESS Inc., Ontario Centre of Excellence, Canada Foundation of Innovation, and my personal PhD fellowship from Ontario Graduate Scholarship.

My highest gratefulness goes to my parents, my wife Xiaoyu and my sister Haifeng, who have caringly supported me. Words cannot just describe how valuable your love, encouragement and patience have been to my completion of this work. It simply would not have been possible without you.

此论文献给所有关心我的人！

This Thesis Is to All Who Being Care of Me in My Life!

TABLE OF CONTENTS

LIST OF TABLES

LIST OF FIGURES

CHAPTER 1
INTRODUCTION AND LITERATURE SURVEY

1.1 INTRODUCTION

In 1959, the Nobel Laureate Professor Richard Feynman delivers the signal of “there is plenty of room at the bottom” at his lecture in Caltech[1]. He described the perspectives of our capability to manipulate individual atoms and/or molecules in the next periods. The people could design one set of precise tools to build up and operate another proportionally smaller set, and so down to the needed scale. In the following decades, the miniaturization of sensors and actuators has been perceived as one dominate trend in science and technology. Stepping into this century, our society is in high demand of these miniature components to be highly integrated as advanced systems to ensure comfort, safety and high quality of our lives. Present systems have been scaled down to micron/submicron, and further down to nanometer scale, in which atoms and molecules are dimensioning. At these small scales especially nanometer scale, there is a great deal of beauty with the system performances, which are more advantageous than its bulk properties, in mechanical, electrical, chemical, thermal, and optical domains [2-7]. Nanotechnology is becoming indispensable in every segment of our society, including automotives, medicine [8, 9], energy harvesting [10] and storage [11, 12], and avionics to name a few.

As one of most important imaging techniques in nanotechnology, atomic force microscopy (AFM) must be explored to characterize physical and chemical properties of materials. AFM was invented in 1986 by Binnig, Gerber and Quate [13] to broaden the usefulness of its precursor scanning tunnelling microscopy (STM) [14] to insulating samples. Within two and half decades, AFM has been quickly developed as a multi-functional tool to probe rich information related to mechanical, electrical, magnetic, chemical and capacitive properties of surfaces at nanometer scale [15]. AFM systems and its extended prototypes have been widely used in diverse areas: data storage[16], life science[17], MEMS/NEMS[18], nanolithography [19, 20], and so on, as shown in Fig.

1.1[15]. To serve for the development of nanotechnology and related techniques, full capabilities of AFM must be in depth explored with well-defined information about surface properties. However, due to high nonlinearity of interactions between AFM tip and sample surface, the interpretation of such interaction in a standard way has not been established. Therefore, more efforts are increasingly needed to solve the elevated issues [21-26].

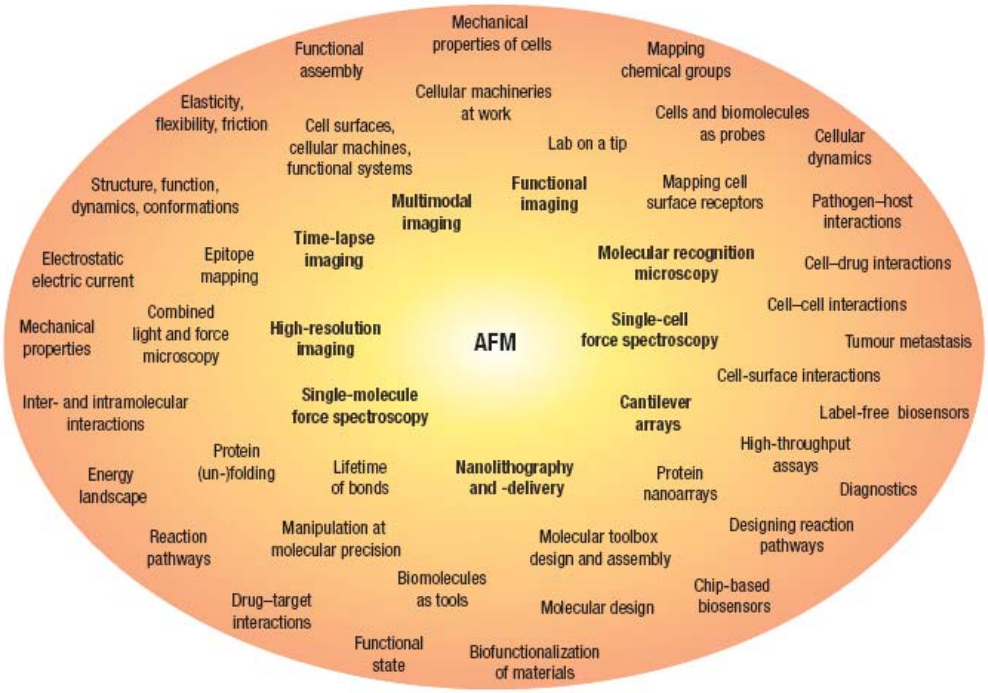

Figure 1.1 AFM has evolved into a multifunctional tool in nanotechnology. Figure copied from Ref. [15].

In principle, AFM is working by detecting the bending of the cantilever, which is regulated by the interacting force between the AFM tip and the sample. The interacting force is nonlinear in nature [27]. When the tip is away from the surface, the dominant forces include attractive Van der Waals and capillary forces, which depend on the materials properties of the sample. When the tip is in contact with the sample, repulsive forces due to elastic properties of the sample act on the tip. This thesis is focused to solve the practical problems in the process of measuring the interacting force to probe surface properties. The main studies include: a) optimization and calibration of detection

sensitivity of AFM operating in more complex environments and emerging imaging modes; b) bypassing the difficulties in calibration of lateral detection sensitivity and lateral spring constant for friction measurements at nanometer scale, along with its application as a chemical force microscopy; c) applying AFM techniques for characterization of our newly proposed material processing techniques. These studies help understanding of AFM systems, and benefit for more efficient operations and advanced applications, i.e. its capability in both of normal and lateral force measurements. The results from this thesis are general to realistic problems and can be applied for many related practices in the study of nanotechnology.

1.2 LITERATURE SURVEY: AFM NORMAL SENSITIVITY AND FORCE CURVE

A typical optic-level AFM system consists of three main components as shown in Figure 1.2, including piezoelectric scanner as an accurate actuator [28], a PI (Proportional-Integral) controller [29], and an optical – lever sensing system [30, 31]. The unique sensing system consists of a flexible cantilever beam with an ultra-sharp tip, a laser diode emitting a collimated laser beam as focused on the cantilever backside, and a quadrant photodetector to receive reflected laser beam from the cantilever backside. The differential voltage signal from the photodetector corresponds to the laser spot displacement across the photodetector plane. In general, the backside of the cantilever is coated with a thin gold or aluminium layer to enhance the reflectivity. Such an optical-lever sensing system can effectively detect the deflection of the cantilever under a very tiny force loaded on the tip.

In force measurement, the AFM cantilever bends in response to a force. Figure 1.3 is a cantilever with an external normal load F at its end. The Euler-Bernoulli equation to describe the elastic curve of the long, slender, one dimensional cantilever made of isotropic material is [32, 33]

$$EI\frac{d^4 z(x)}{dx^4} = F\Delta(L-x) \tag{1.1}$$

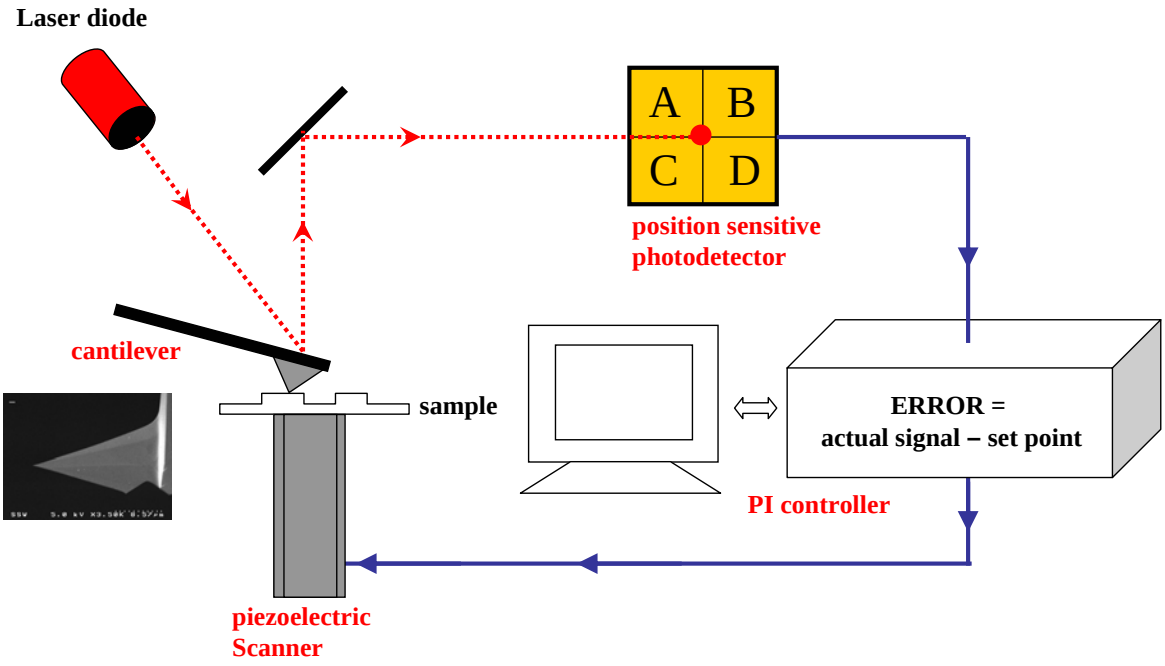

Figure 1.2 Main components of an atomic force microscopy system.

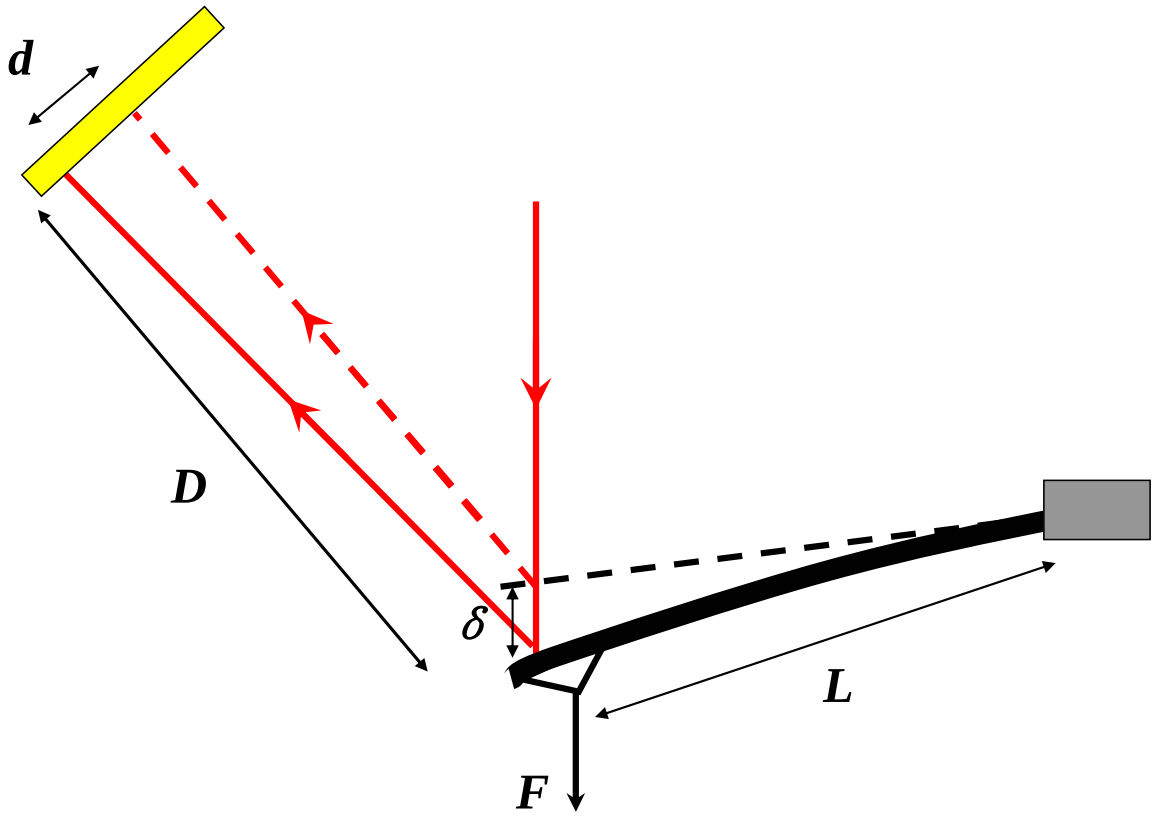

Figure 1.3 Principle schematics of the optical – lever sensing system.

where $z(x)$ describes the deflection normal to the surface of cantilever at the position x. E is the Young's modulus, L is the cantilever length and I is the inertial moment for cantilever. F is external point load and $\Delta(x-L)$ is equal to unit when $x=L$. The theory is valid if the slender ratio of the length of the cantilever to its thickness is relative large, about more than 10, and if the ratio of the deformation to the length of the beam is relatively small, about less than 0.1. In general, the length and the thickness of an off-shelf cantilever are about 100~300μm and 1~5μm, respectively. The deformation of the cantilever is about less than 100nm. Therefore, the deflection δ of the cantilever at $x = L$ can be solved by

$$\delta = z(x)\big|_{x=L} = \frac{F}{6EI}(3Lx^2 - x^3)\,|_{x=L} = \frac{FL^3}{3EI} \tag{1.2}$$

Then the spring constant of the cantilever the cantilever is given by[34]

$$k_c = \frac{3EI}{L^3} \tag{1.3}$$

Further, the bending angle of the cantilever is given by

$$\theta_{bend} = \frac{dz(x)}{dx}\Big|_{x=L} = \frac{FL^2}{2EI} = \frac{3F}{2Lk_c} \tag{1.4}$$

Under static load $F = k_c\delta$, for θ_{bend} we get

$$\theta_{bend} = \frac{3}{2}\frac{\delta}{L} \tag{1.6}$$

Corresponding to the bending of the cantilever, the displacement of the laser spot on the plane of the photodetector is *d*, as given by [32]

$$d = 2\theta_{bend} \times D = 2\frac{3D}{2L}\delta \tag{1.7}$$

where D is the spatial distance between the photodiode and the cantilever end. This displacement *d* gives rise to an imbalance in the power incident on the top – down phases of the quadrant photodetector, and the differential voltage ΔV can be linearly related with *d* by

$$\Delta V = \beta \times d \tag{1.8}$$

where β is a conversion coefficient dependent on the parameters of the photodetector. Combining Equations (1.7) and (1.8), we finally have

$$\Delta V = \beta \times 2\theta_{bend} \times D = 2\beta \frac{3D}{2L}\delta = \sigma \times \delta \tag{1.9}$$

σ is the optical – lever detection sensitivity of AFM with unit V/nm. From Equation (1.9) the voltage signal is directly related with the bending angle θ_{bend}. Therefore, the optical – lever technique is indeed working to detect the cantilever bending angle θ_{bend} rather and the cantilever deflection δ [35]. They are different by $3/2L$. The correlation between θ_{bend} and δ in Equation (1.6) is only valid for a constant load and static cantilever[35].

The calibration of σ in Equation (1.9) is generally finished by approaching the tip onto a hard solid substrate, such as Sapphire with Young's modulus ~ 435 GPa, and then lifting the tip back. In this process, we monitor both of ΔV and PZT tube displacement which is equivalent to the cantilever deflection δ. The slope of obtained approaching or retracting curves represents σ as shown in Figure 1.4(upper). Its unit is V/nm. Here, we give a definition of inverse optical lever sensitivity (*InvOLS*) [36] as

$$InvOLS = \frac{1}{\sigma} = \frac{\delta}{\Delta V} \tag{1.10}$$

If we have known the spring constant k_C of the cantilever, Equation (1.9) can be written as:

$$F = InvOS \times \Delta V \times k_C \tag{1.11}$$

Then the load force can be finally determined and the obtained curve is called as force – displacement curve or briefly **force curve** [37].

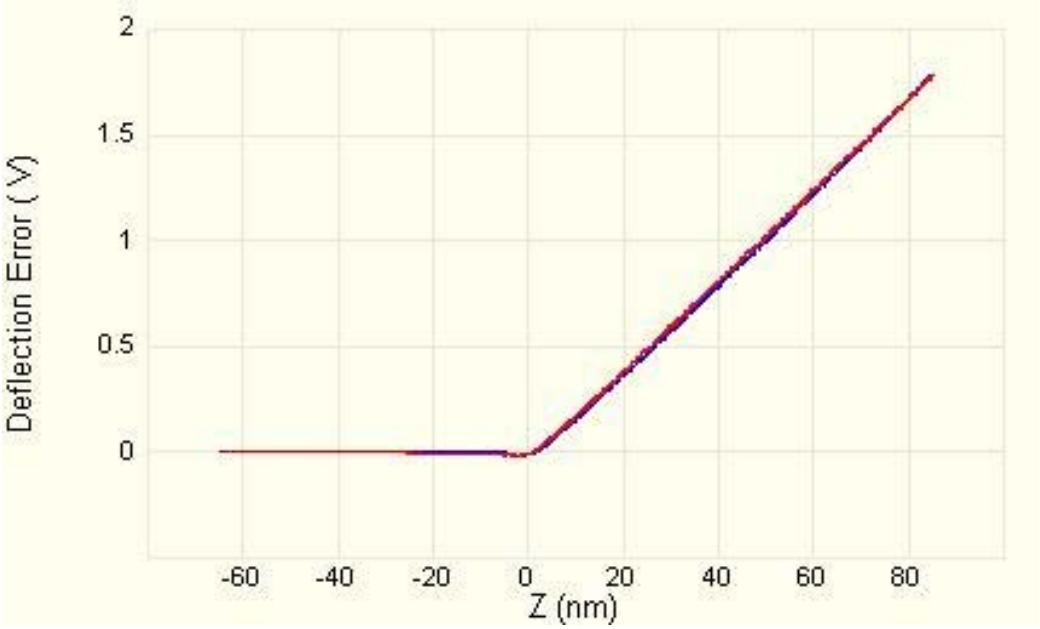

On hard substrate

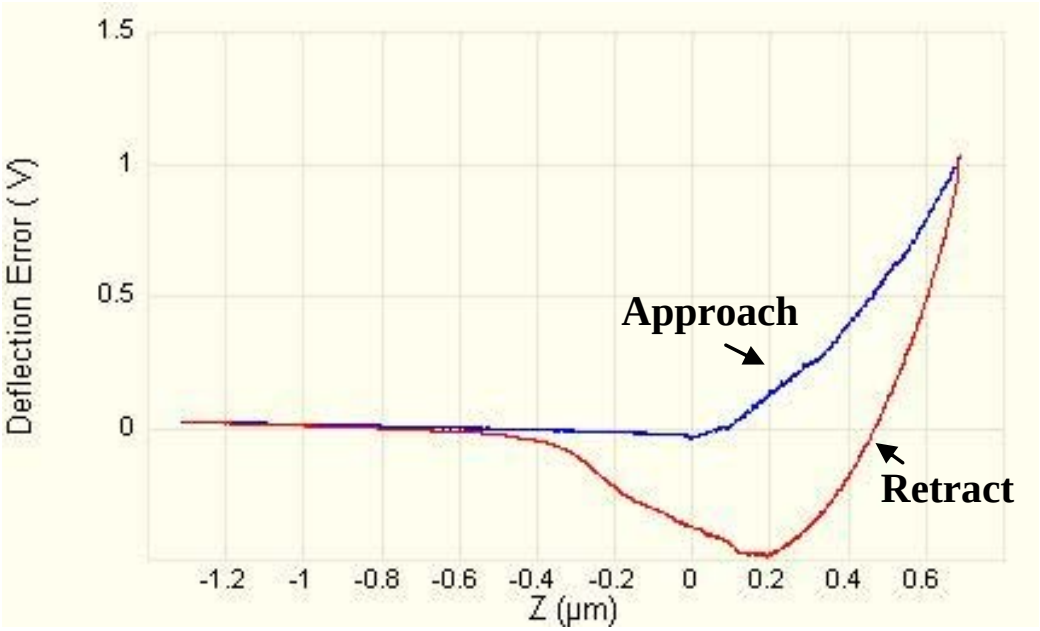

On soft substrate

Figure 1.4 Force curves obtained on hard substrate (up) and soft substrate (bottom), respectively.

The force curve has included important information on the surface properties of the samples on which the force is loaded [37]. The indentation depth of AFM tip into sample can be extracted from Z displacement and the cantilever deflection. Therefore, Young' modulus can be calculated based on the force curve. Both approach curve and retract curve can be applied for the calculation. When the tip approaching the sample with negligible "jump – in" force, the approach curve could be easily applied based on Hertz model; otherwise, Derjaguin – Muller – Toporov model should applied on the retract curve. Meanwhile, the adhesion between the AFM tip and the sample can be obtained from the lowest point of the retract curve. One of most important adhesion applications is single molecule force microscopy. Furthermore, the area closured between approach and retract curves corresponds to the dissipated energy during loading and unloading processes, which may come from adhesion hysteresis and viscosity [37]. Radmacher [38] proposed a force volume technique to collect an array of force curves over the entire sample area. Each force curve is measured at a unique X – Y position in the area, and force curves combined into a three-dimensional array of force data. Hence, these force curves can contain a volume of elasticity, adhesion and dissipation on the whole surface [39, 40]. Although informative, such force volume method is very time consuming not suitable for application which requires short scanning time esp. for biological application as well as it has lost its lateral resolution. A 64 by 64 pixels image required hours of operation time. Alternative means will be introduced later on.

1.3 LITERATURE SURVEY: CALIBRATION OF CANTILEVER

1.3.1. Normal Spring Constant Calibration

To determine the force between AFM tip and sample, the spring constant of the cantilever must be calibrated in advance. If the cantilever is an isotropic beam of a length L with a rectangular cross-section of width W and thickness T, its normal spring constant can be analytically given by [34]

$$k_c = \frac{EWT^3}{4L^3} \tag{1.12}$$

However, commercial AFM cantilevers are manufactured through MEMS batch process so that the geometries and shapes of the cantilevers are deviated from their design parameters. Furthermore, the backside of cantilevers is generally coated with a thin gold or aluminium layer to enhance the reflectivity. As a consequence, the spring constant obtained from Equation (1.12) is severely deviated from the true value. An amount of efforts have been reported in the literature to determine the spring constant of single AFM cantilever working in the experiment as following.

The added mass method [41, 42], also known as the Cleveland method, is based on the following formulate relating a cantilever's fundamental resonance frequency, spring constant, and mass:

$$f = \frac{1}{2\pi}\sqrt{\frac{k_C}{M + m^*}} \tag{1.13}$$

where m^* is the "effective mass" of the cantilever and M is the added mass to the tip end of the cantilever. This added mass can be small tungsten microspheres[41] or liquid droplets[42]. To avoid damage the tip, the added mass should be placed at a distance ΔL from the tip along the length L of the cantilever, as shown in Figure 1.5. Therefore, the M in Equation (1.12) should be corrected according to:

$$M = M_{meas}\left(\frac{L - \Delta L}{L}\right)^3 \tag{1.14}$$

where M_{meas} is the measured mass of microsphere before added. In this method, the imperfect measurement of the tiny mass could introduce error as well as there is some risk of damage to the cantilever when we add the mass.

Alternative one is reference spring lever calibration method as first proposed by Torri et al. [43] with manufacturing a 35mm long rectangular reference lever from mechanical cut copper foil. At present, micro-machined silicon reference rectangular beam cantilever array is commonly adopted and commercially provided by Veeco Inc.[44]. The reference spring constant of each cantilever has been accurately calibrated using laser Doppler

vibrometry [45] based on thermal method [46], which will be discussed in the next. The spring constant of the unknown cantilever is calibrated by pressing it against a reference spring lever with already calibrated spring constant k_{ref} , as shown in Figure 1.6, and then against a very stiff substrate to obtain two inverse optical – lever sensitivities $InvOLS_{ref}$ and $InvOLS_{sub}$, respectively[44]. Therefore, we have:

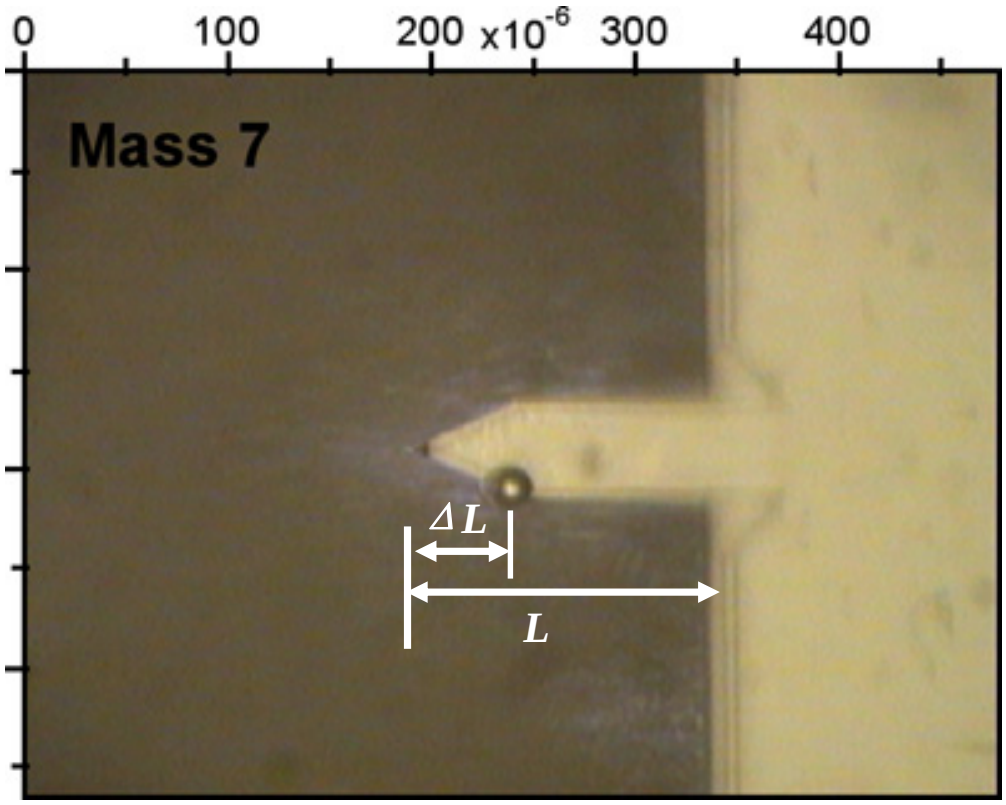

Figure 1.5 Added mass method or Cleveland method. Figure copied from Ref. [41].

$$k_C = k_{ref}\left(\frac{InvOLS_{ref}}{InvOLS_{sub}} - 1\right)\left(\frac{1}{1-\Delta L/L}\right)^3 \tag{1.15}$$

where L is the reference lever length and ΔL is the off-end loading distance from the actual point of contact on the reference lever to its free end[44]. The uncertainty in the calibration is dominated by the error in determining the detection sensitivity. The accuracy of the deflection sensitivity calibrations can be improved by operating our ramp mode with closed – loop Z as supported in our AFM systems. Typical calibration curves

are shown in Figure 1.4, where the slope of curve on rigid substrate is much sleeper than that on reference lever.

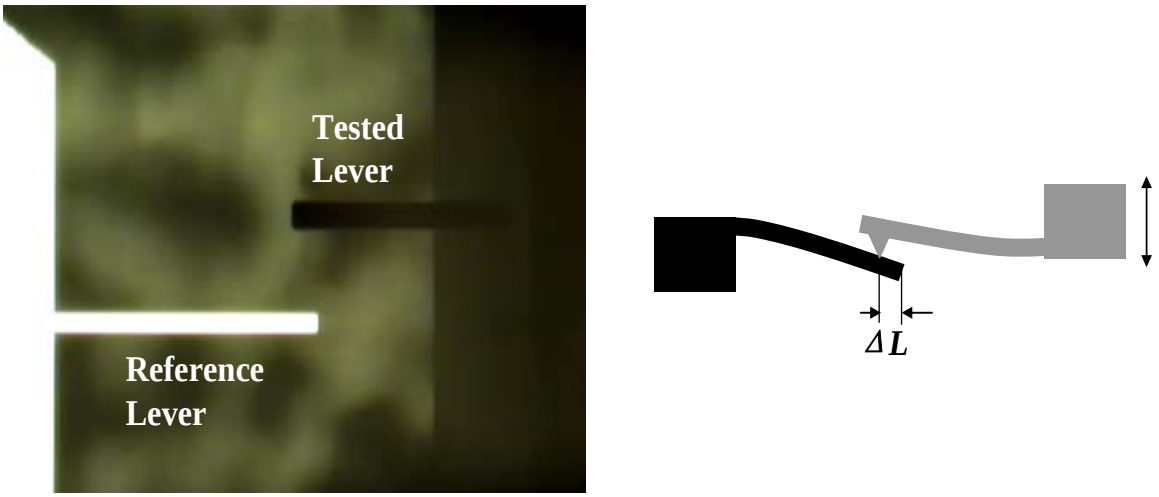

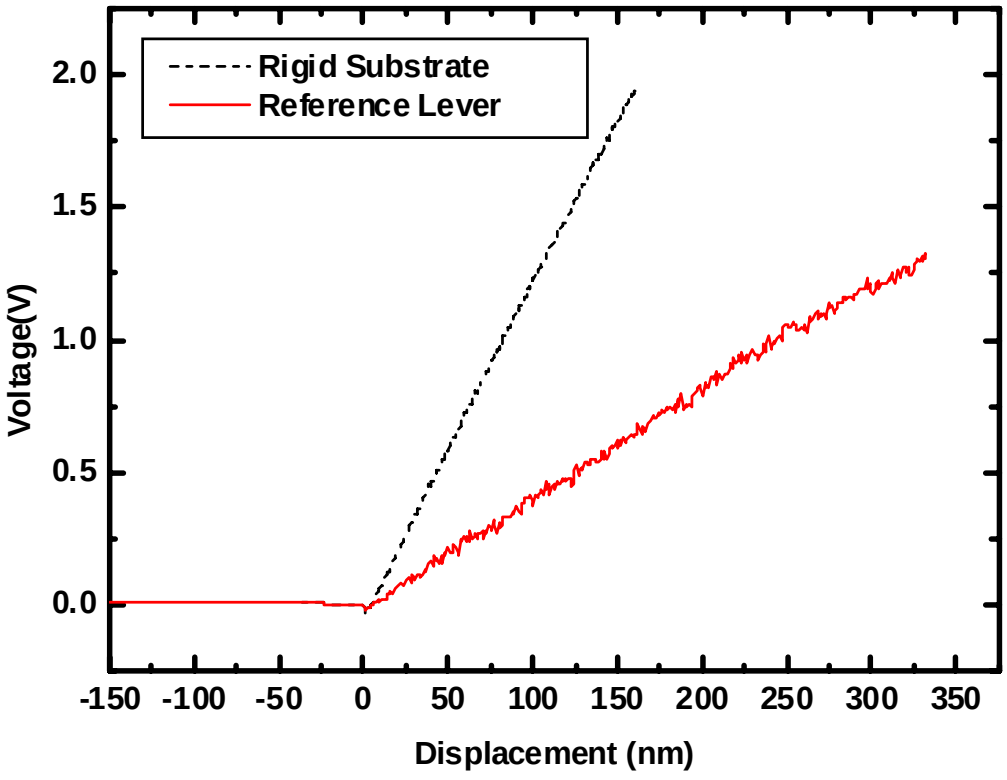

Figure 1.6 Demonstration of reference lever method for spring constant calibration.

The aforementioned two methods are based on special design of external accessories with their own high accuracies. The next “thermal method” is completely self-tuned with its nature in physics. The beam system can be accepted as a simple harmonic oscillator with ignoring the damping of air as shown in Figure 1.7. In equilibrium with its surroundings, the harmonic oscillator will fluctuate in response to thermal noise. The equipartition theorem points out that the temperature T of a system is related with its average energies and each degree of freedom has an average energy of $1/2k_BT$, where k_B is Boltzmann constant. Therefore, Hutter and Bechhoefer [47] obtained the most widely used formula in the calibration of cantilever spring constant:

$$k_C = \frac{k_B T}{\langle z^2 \rangle} \tag{1.16}$$

where $\langle z^2 \rangle$ is the mean square displacement of the cantilever. This quantify can be found by performing a power spectral density analysis of the cantilever oscillations under the peak of the fundamental mode [47], as shown in Figure 1.7.

Immediate corrections were developed to enhance the accuracy of this thermal method in the calibration of spring constant. Butt and Jaschke [35] pointed that the cantilever did not behave as an ideal harmonic oscillator but fluctuated with higher modes[48]. In thermal equilibrium each vibration mode of the beam has a mean thermal energy of $1/2k_BT$ for its potential energy. They derived a formula by using beam theory with considering the actual beading mode at its fundamental resonance:

$$k_C = 0.971\frac{k_B T}{\langle z^2 \rangle} \tag{1.17}$$

As we also mentioned earlier, the optical – lever technique is indeed working to detect the cantilever bending angle rather than the cantilever deflection. These bending angle changes depend on the bending mode the cantilever and the measured displacement $\langle z^* \rangle$ by the optical lever technique is different from the actual displacement $\langle z \rangle$ of the cantilever [35]. The corrected formula should be:

$$k_C = \frac{0.971 k_B T}{\chi^2 \left\langle z^{*2} \right\rangle} \tag{1.18}$$

where χ represents the correction factor in this thesis [36]. This factor is dependent on parameters of optical – lever system, including shape of the cantilever[49], laser spot size and location on the cantilever [36, 50], and tip – sample interaction stiffness [51, 52]. The Chapter 3 will give detailed discussion on this factor through our study.

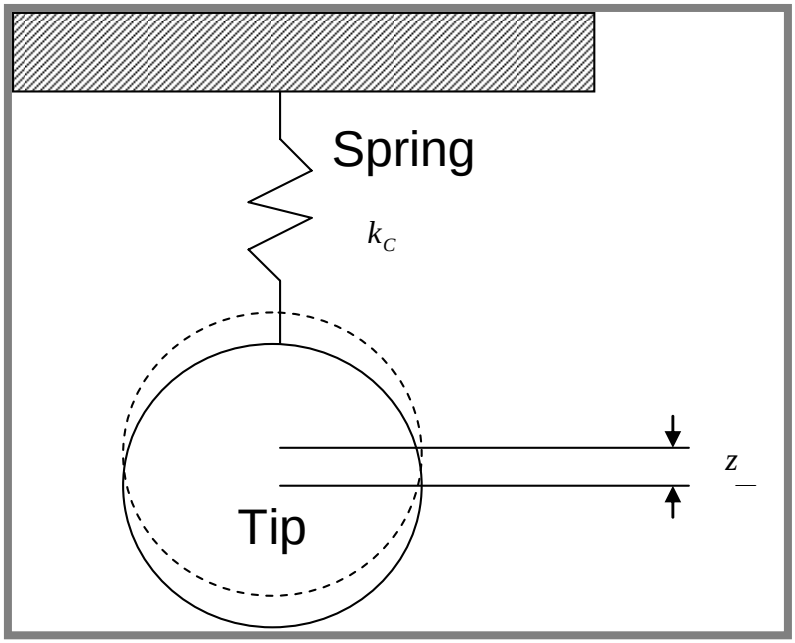

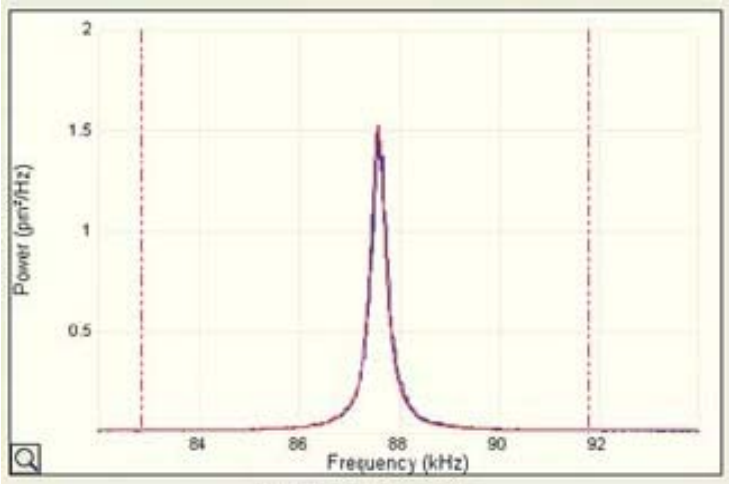

Figure 1.7 Simplified harmonic oscillator model for free-end cantilever beam in ambient (top) and its spectrum (bottom)

1.3.2 Calibration of Friction Force of AFM

In general, the calibration of friction force of AFM is much more complex. The earliest work was done by Mate et al. [53], and their tungsten wire tip had its own lateral spring constant. The lateral deflection is directly measured by an interferometer. On optical – lever AFM, two steps are needed including calibration of lateral detection sensitivity and calibration of lateral spring constant.

The lateral detection sensitivity, similar to normal detection sensitivity, maps the relationship between lateral voltage change of the quadrant photodetector and lateral deflection of the cantilever. Although some researcher have analyzed the sensitivity based on known optical path of AFM as shown in Figure 1.8 (a) [54, 55] , such information are not provided for most of users relying on commercial AFM systems. On another hand, to introduce a quantitative and known lateral displacement at the AFM tip is not an easy job. External and accurate accessories are necessary, such as vertical sliding wall [56], titled mirror with an calibrated angle [57], and mechanical lever [58].

To calibrate the lateral spring constant, an isotropic and rectangular cantilever can be analytically derived for its lateral spring constant by [57, 59]:

$$k_L = \frac{GWT^3}{3L} \tag{1.18}$$

where G is shear modulus. This equation is not accurate for any commercial cantilevers esp. with metal coating. A complex setup must be designed for this calibration in Figure 1.9, for example a glass fibre with known spring constant [60], MEMS based lateral electrical nanobalance [61], and magnetic field device with calibrated Lorenz force [62].

Since our ultimate goal is to calibrate the friction coefficient, which is a key parameter of surface properties, a wedge method has been developed by Ogletree et al. [63] to bypass the difficulty of calibration of lateral spring constant and lateral detection sensitivity for friction force and then for friction coefficient. In the method, a cantilever tip is scanned across a calibration sample with two well-defined slopes, and the friction signal is monitored as a function of applied load. The total force applied by the tip on the surface

can be divided into two components: a friction component parallel to the surface and another component normal to the surface. Under constant normal load, the lateral signal is shown in Figure 1.10, where the offset of the friction loop is not zero and depends on the normal load [63]. An analytical formula was derived as:

$$\mu + \frac{1}{\mu} = \frac{2\Delta}{W \sin 2\theta} \tag{1.19}$$

where Δ is the offset of the friction loop, W is the half width of the friction loop, and θ is the open angle of the wedge.

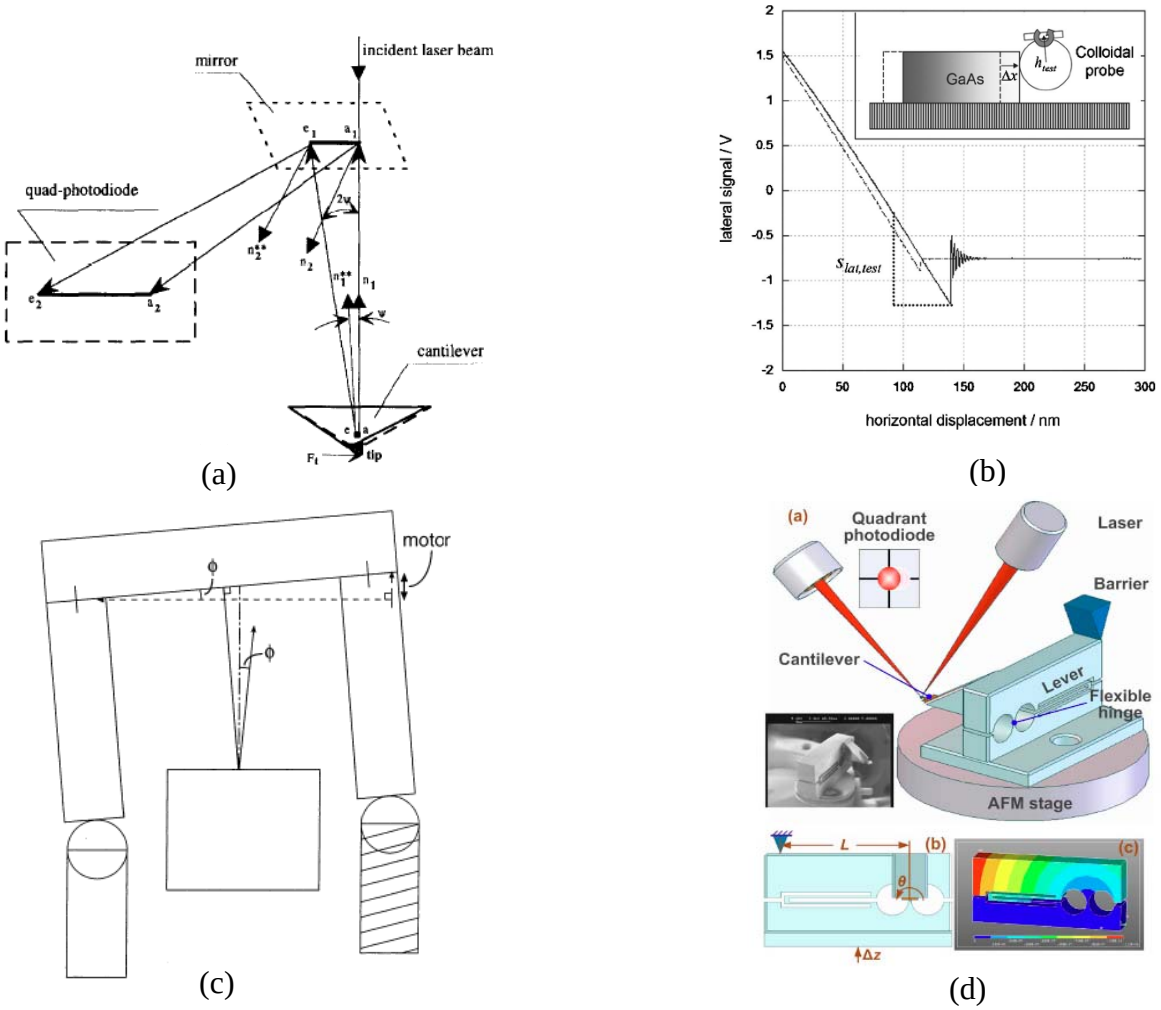

Figure 1.8 Calibration of lateral detection sensitivity of AFM: (a) optical path. Figure copied from Ref. [54]; (b) vertical sliding wall. Figure copied from Ref. [56]; (c) titled mirror beneath the head. Figure copied from Ref. [57]; (d) mechanical lever. Figure copied from Ref. [58].

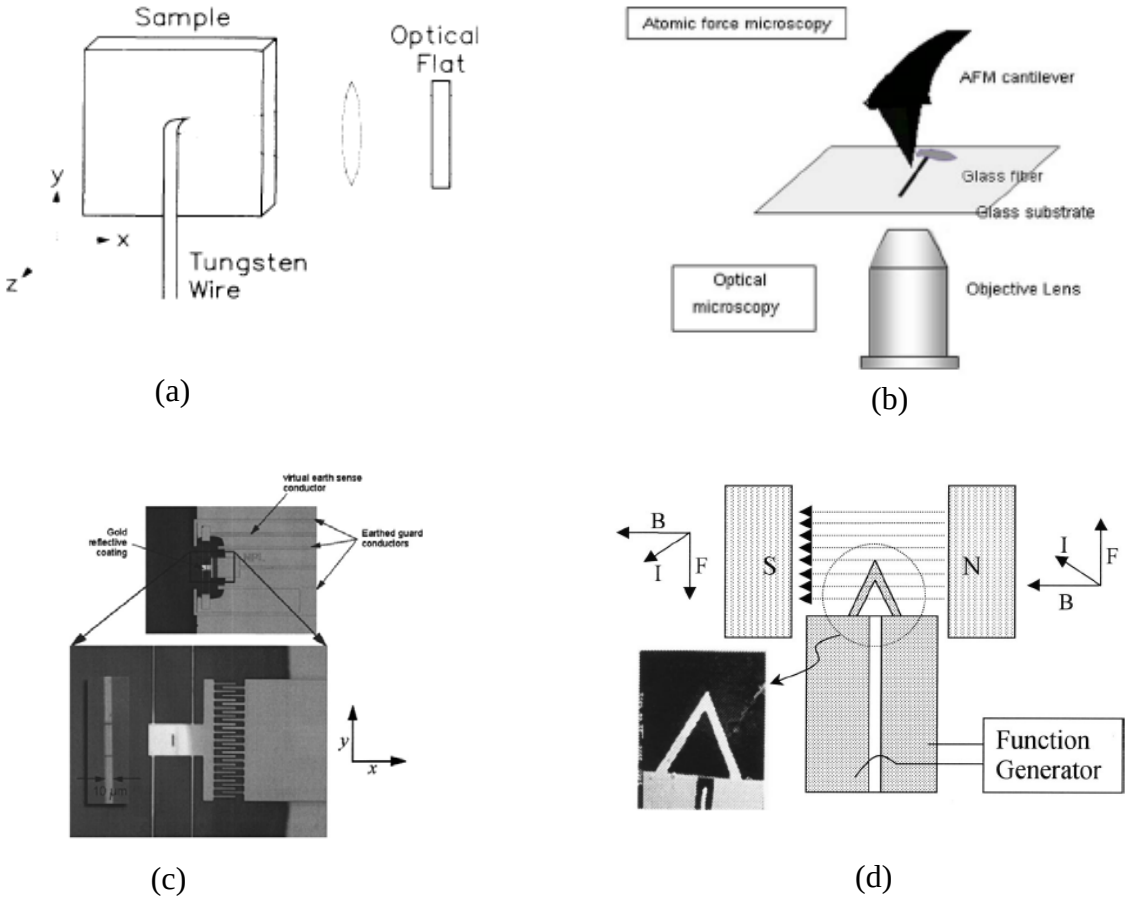

Figure 1.9 Calibration of lateral spring constant of cantilever: (a) tungsten wire with known spring constant. Figure copied from Ref. [53]; (b) glass fibre. Figure copied from Ref. [60]; (c) MEMS based lateral electrical nanobalance. Figure copied from Ref. [61]; (d) magnetic field with calculated Lorenz force. Figure copied from Ref. [62].

The major error source in this method is coming from measurement of θ and Ogletree et al. applied an annealed faceted $SrTiO_3$ surface with (101) and (103) planes as calibration sample. The tilted angles for the two planes are 14.0^o and -12.5^o, respectively. Recently, other calibration samples with known angles have also been developed and commercial one can be obtained from Mikromasch, Inc., such as TGF.

Until now, the wedge method has been esteemed as a gold methodology for friction coefficient calibration. Recently, we have developed a simpler method for calibrating

friction coefficient through applying a T – shape cantilever [22] and this method will be discussed in the Chapter 4.

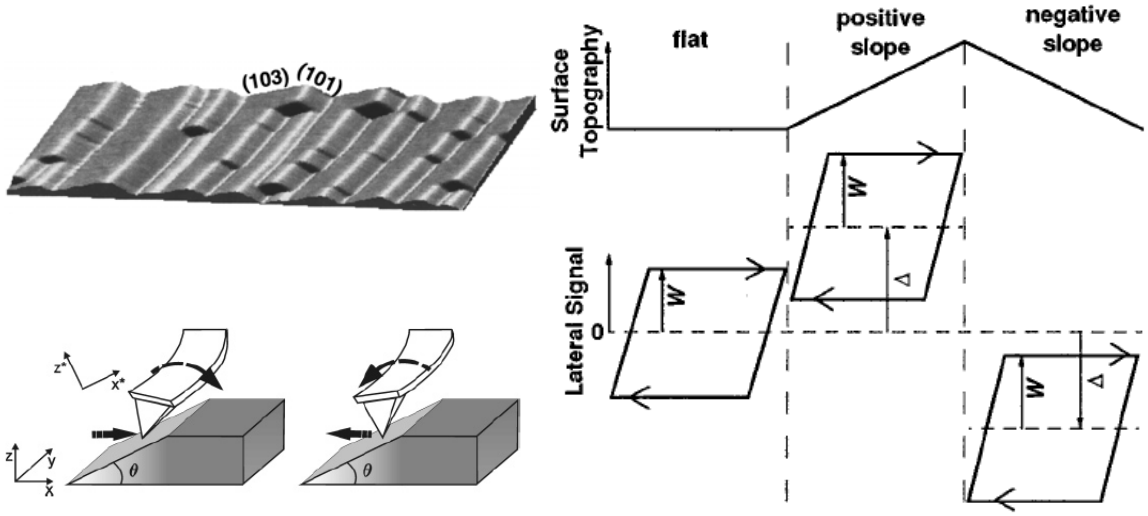

Figure 1.10 Wedge method for calibration of friction coefficient. Figure copied from Ref. [55, 63].

1.4 LITERATURE SURVEY: AFM MODES

The principal operating modes of AFM include contact mode, tapping (intermediate) mode, and non–contact mode[32]. They are distinguished according to different operating force ranges as shown in Figure 1.11. Contact mode and tapping mode are two most widely used AFM modes in ambient environment. Non – contact mode is typically applied in a vacuum. Herein, only contact mode and tapping mode are reviewed for their applications in this thesis.

1.4.1 Contact Mode

In contact mode, the AFM tip is in an immediate contact with sample surface under repulsive force. While scanning a topographic image of a sample, the height position of the translation stage, to control the up-down movement of the AFM tip, is controlled by a feedback loop, which maintains a constant force between tip and sample. With appropriate selection of softer AFM cantilevers, contact mode has been successfully applied to image morphology of soft samples, such as dried red blood cell and monolayers with stiffness around 100MPa finished in our work (Figure. 1.12). However,

for softer materials with Young's modulus at the order of KPa and even less[64], significant deformation and damage on samples often occur in contact mode during imaging in air because enough loading force must be applied due to contaminants and adsorbed moisture in air. Therefore, contact mode imaging may be performed in a liquid environment, which minimizes meniscus effects from moisture and contaminant so that much lower contact forces can be used. In addition, biological buffer are generally applied together with AFM to image as well as retain the nature of biological samples in vitro [65].

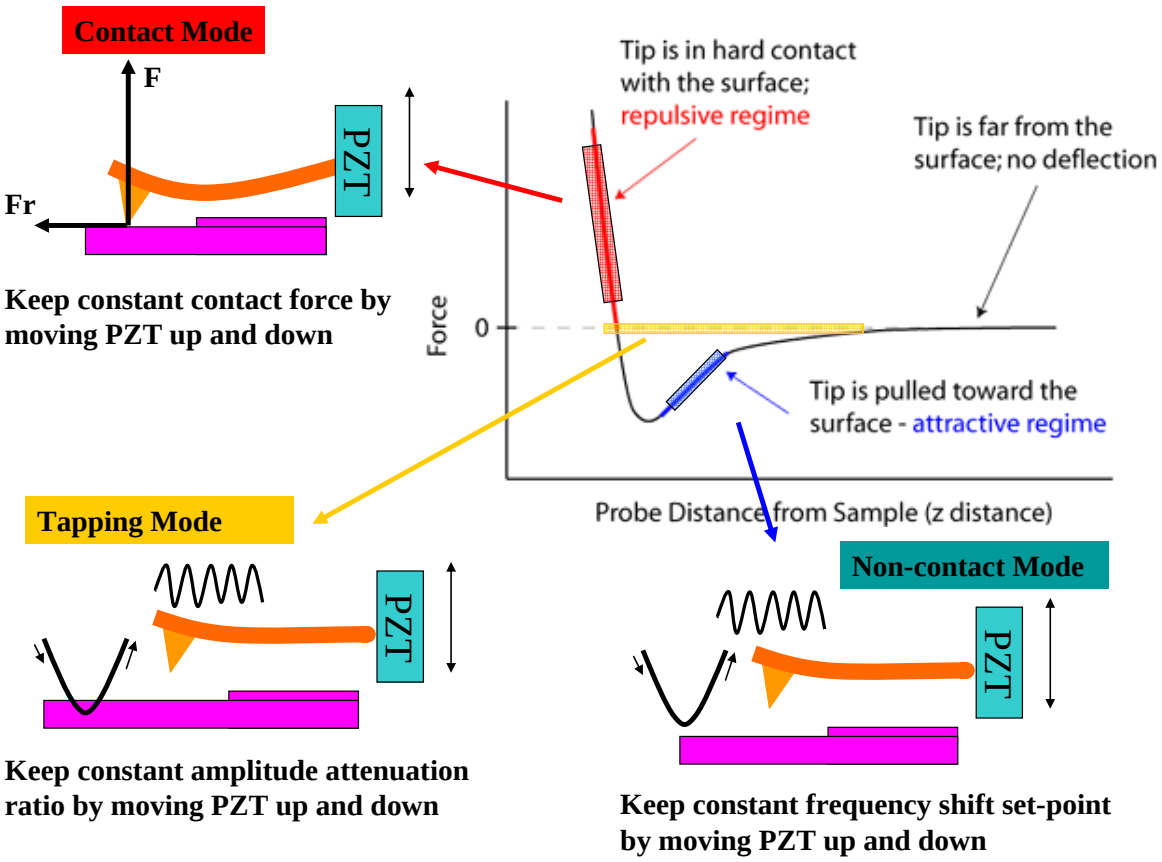

Figure 1.11 Operating modes of AFM at different force ranges.

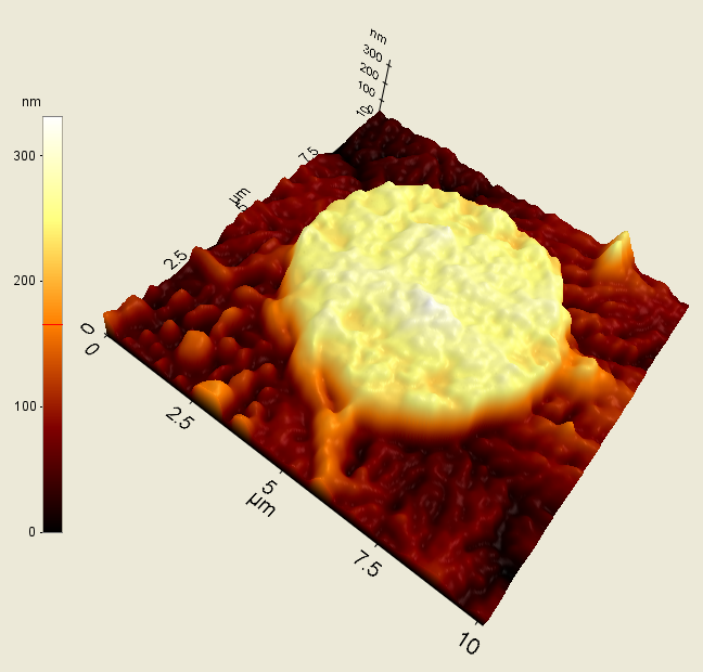

Dried Red Blood Cell

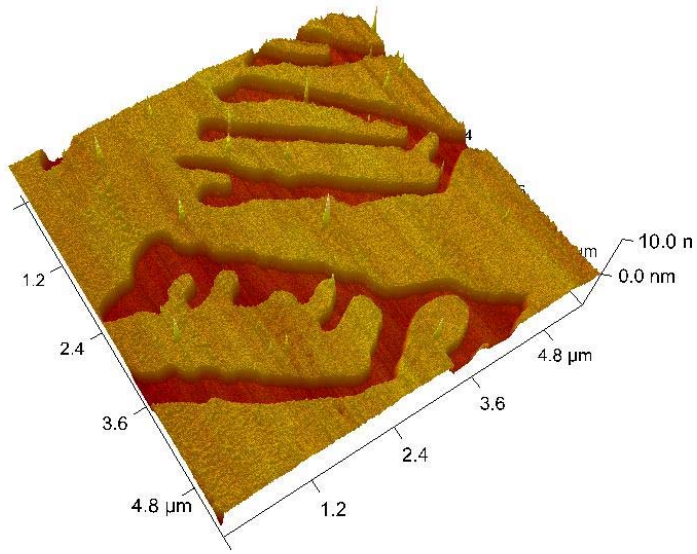

Dotriacontane $C_{32}H_{66}$ Thin Film

Figure 1.12 Contact imaging of soft materials in air: dried red blood cell and thin film

From the contact mode scanning, not only a useful topographical map of the surface is obtainable, but also lateral friction image is available through monitoring the lateral signal on the photodetector. The frictional image was earliest carried out by Mate et al. [53] to observe atomic-scale features on graphite surface, as reproduced in our work (Figure 1.13), which displays the honeycomb structures with periodicity $0.24 \pm 0.01 nm$. The atomic - scale frictional image has represented pioneering work of studying difference of tribology between micro/nano-scale contact and macro-scale contact, and leads eventually to the advances in atomic/molecular scale understanding of frictional phenomena [66, 67]. On the other hand, the lateral friction is dependent on heterogeneity of surface materials, such as chemical functionalities. Therefore, lateral friction AFM can be applied as a chemical force microscopy to provide nanoscale information about the chemical groups on a surface, which ultimately determines the friction, adhesion, and compliance of the surface at the molecular scale[68]. When an AFM tip is laterally scanning across a surface with different chemical groups such as – COOH and – CH_3, due to the hydrophilicity of silicon AFM tip less interaction from – CH_3 than from – COOH is distinguished from the lateral friction map, as shown in Figure 1.14.

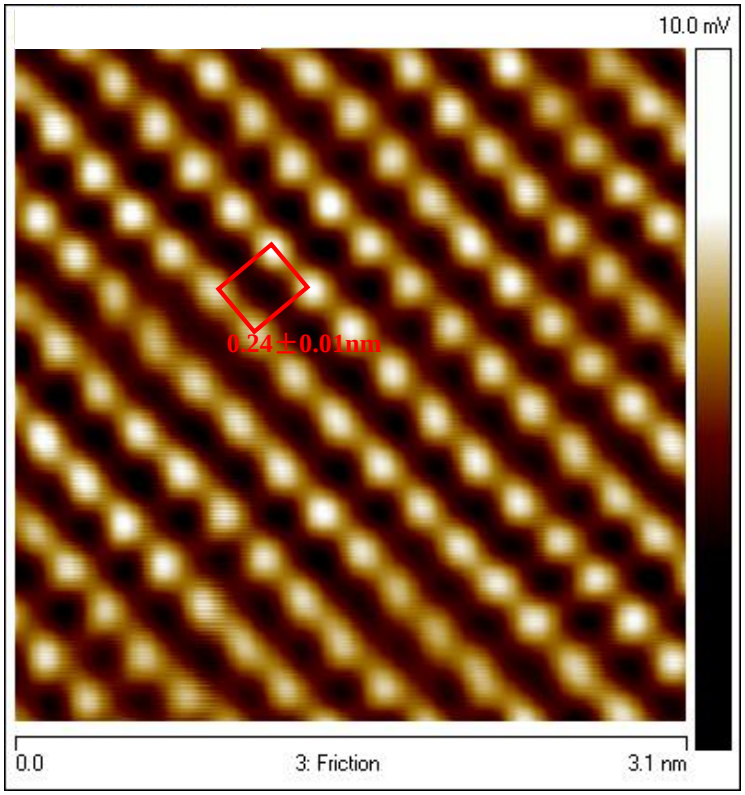

Figure 1.13 Atomic resolution friction of HOPG surface.

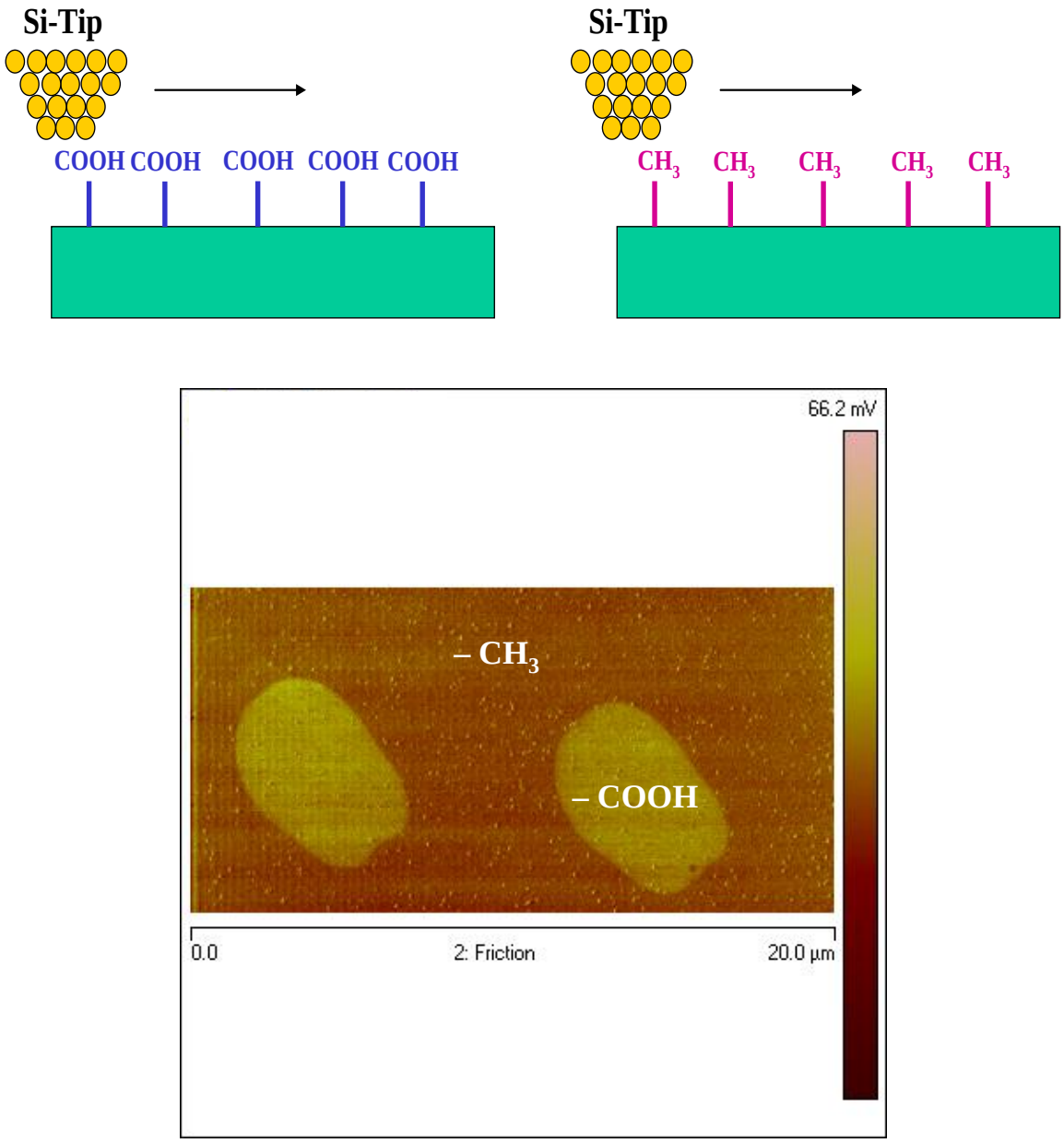

Figure 1.14 Chemical force microscopy distinguishes hydrophilic and hydrophobic groups on the surface.

1.4.2 Dynamic Mode: Tapping and Higher-order Harmonics

Tapping mode AFM was invented by Zhong et al. [69] to reduce tip – induced irreversible damage of contact mode on polymer with low modulus. During scanning, the tapping mode AFM oscillates its cantilever with amplitude of up to 100 nm and

frequency close to or at its fundamental resonance. The AFM tip is in an intermittent contact with the surface, about only 1% of each cycling time [70, 71]. In tapping mode, the feedback loop is to control the translational stage up-down and therefore maintain the damped oscillation amplitude of the cantilever at a constant set point. Beyond its topographic imaging technique on polymeric system, tapping mode has demonstrated the phase imaging capability to distinguish material heterogeneity in composition, adhesion, friction, viscoelasticity, and other properties, such including electric and magnetic. When the AFM cantilever is driven by a sinusoidal wave voltage at its fundamental resonance, the phase shift of the cantilever responsible oscillation is monitored.

Since its dependence on material property, phase image of tapping AFM has attracted increasing interests from the community. It was noticed that phase shift has certain relationship with mechanical property of the surface[72]. As shown in Figure 1.15, stiffer filler areas are brighter than softer rubber areas. It represents that less phase lag is with harder surface. However, the phase shift is, in deed, affected by complex combination of material stiffness with other existent dissipation mechanisms during the intermittent contact between tip and surface, such as adhesion and viscoelasticity. Tomayo and Garcia [73, 74] theoretically and experimentally demonstrated the phase shift in condition of adhesion hysteresis and/or viscoelastcity as involved as shown in Figure 1.16. However, such phase shift is not sensitive to stiffer materials with Young's modulus E > ~2GPa, approximately, when even with energy dissipation involved. Cleveland et al. [75] pointed that the tapping mode AFM phase image should be interpreted in terms of energy dissipation by:

$$E = \frac{1}{2}\frac{\pi k_C A^2}{Q}\left[\left(\frac{A_0}{A}\right)\sin\Delta\phi - 1\right] \tag{1.20}$$

where A is the driving amplitude, A_0 is the set-point amplitude, and Q is the quality factor. Furthermore, the interpretation of phase image is also dependent on the tapping condition [72]. In our study, tapping AFM is applied to image the sample mixed with low-density polyethylene (LDPE) and polystyrene (PS). As shown in Figure 1.17, the phase contrasts in light and hard tapping are completely reversible, and can not correctly tell the stiffness contrasts even for the Young's modulus less than 2 GPa. Although nanoindentation-based

force volume mode [38] and force modulation mode [76] have such quantitative capability, the force volume mode is too low in lateral resolution and imaging speed (taking hours to finish a only 64 by 64 pixels image) for practical application esp. biological imaging, and force modulation mode is still working in contact mode with selection on stiffness of materials. Therefore, there is a necessity to correctly determine the stiffness contrast through an effective way.

Due to the nonlinearity of tip – sample interaction, Hillenbrand et al. [24] noticed that during tapping the dynamic amplitudes of the cantilever were stimulated at its higher – harmonics (integer times of the fundamental resonance), which have certain relationship with the mechanical property of the surface. Stark et al. [27] concluded the twofold benefic in the acquisition of higher harmonic data, which is useful to optimize the imaging conditions in tapping mode and differentiate qualitatively between dissimilar materials that are hardly distinguished and interpreted by conventional tapping mode AFM, such as shown in Figure 1.17.

However, there are some major problems in applying higher-harmonics: first, the signal – to – noise ratios of the higher harmonic vibrations are not sufficient for practical measurement. In Figure 1.17, although we can use higher-harmonics to monitor the mechanical properties of composites, the amplitudes at the harmonics are quite low only about 4 ~ 5 mV. Secondly, although the amplitudes of such harmonics can be monitored, there is no quantitative relationship with Young’ modulus of surface. Furthermore, only certain harmonics embody the information on stiffness, and other harmonics may represent other surface properties [77, 78].

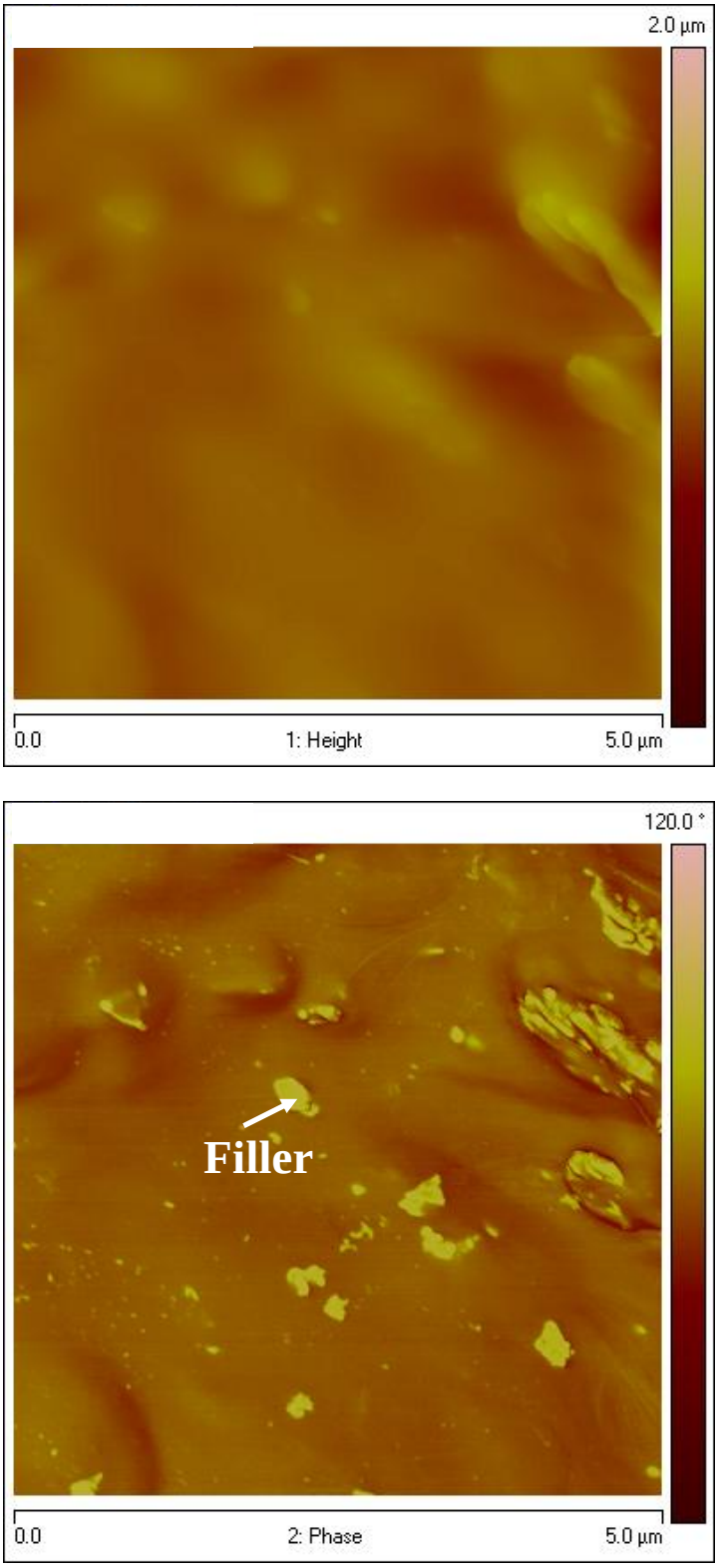

Figure 1.15 Tapping mode AFM image on filler – reinforced rubber: (up) morphology; (bottom) phase image.

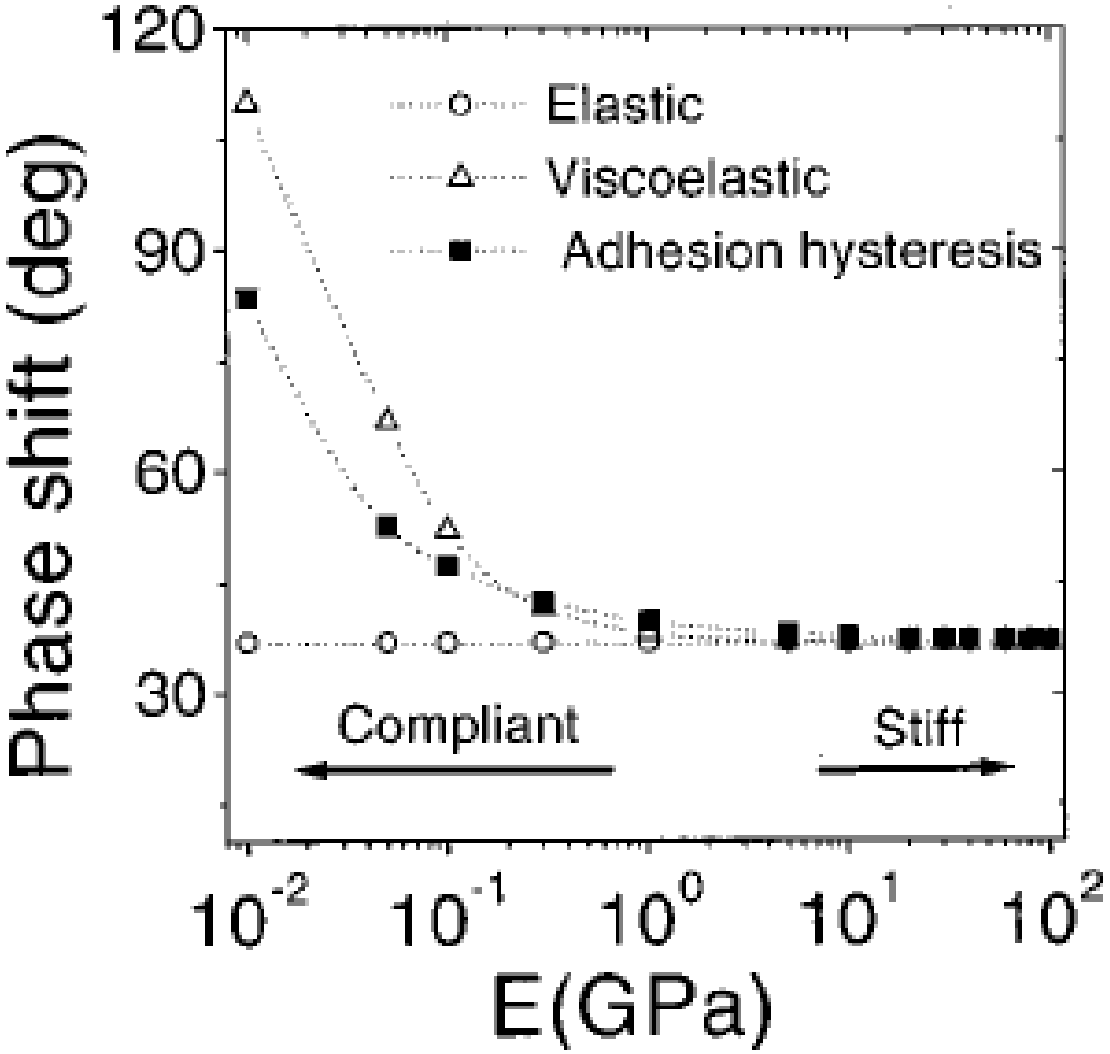

Figure 1.16 Theoretical phase shift dependence on elastic properties for different energy dissipation mechanisms in tip – sample interactions. Figure copied from Ref. [73].

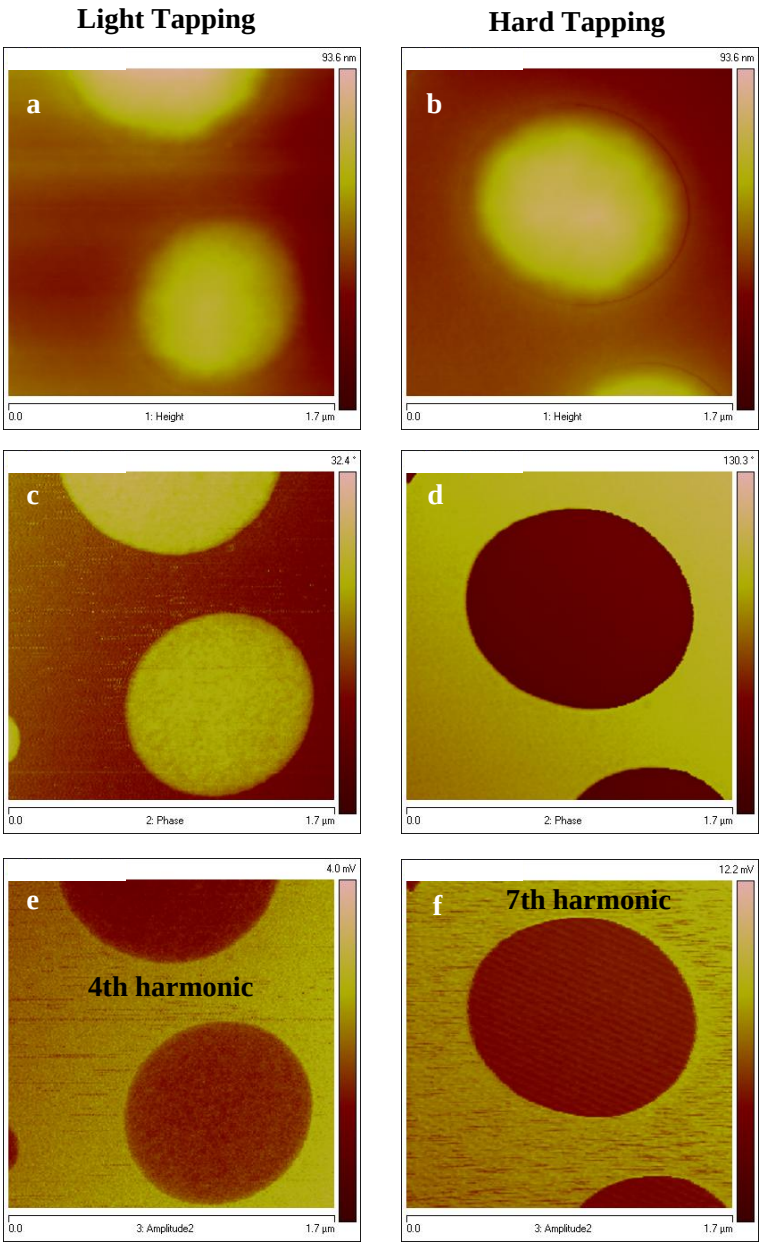

Figure 1.17 Light tapping (left) and hard tapping (right) are carried on the same LDPE – PS composite sample. (a) and (b) are showing morphology of LDPE and PS and can not tell us which is LDPE and which is PS. (c) is phase image at light tapping and shows dissipation contrast where LDPE (brighter) is more viscous and adhesive than PS (darker). (d) is phase image at hard tapping and shows elasticity contrast where LDPE (darker) is softer than PS (brighter). (e) is 4th harmonic amplitude at light tapping and (f) is 7th harmonic amplitude at hard tapping; and they both show LDPE (darker) is softer than PS(brighter).

Representative contributions to deal with these problems were presented by Sahin et al. [22, 23]. Their earlier work was to micromachine a harmonic cantilever with a notch, in which the position of the notch corresponds to a highly curved region of the third mode, but not to highly curved regions of the first two modes. They fabricated such cantilevers by reducing the stiffness of the third order flexural mode relative to the fundamental mode, and demonstrated that the harmonic cantilever has integer ratio between its third and fundamental resonance frequencies, such as 16th harmonic as shown in Figure 1.18. Recently, they redesigned their T – shape cantilever with its tip offset by a distance from its long axis as shown in Figure 1.19. During the normal tapping, the T – shape cantilever was also twisted by the interaction between the tip and sample. In their analysis, torsional response signal to noise was much significant than that with flexural response. When the tip hit the sample, the cantilever bends torsionally in proportion to the torque generated by the tip – sample forces. Furthermore, there was an existing transfer function to map the relationship between first torsional response and tip – sample interaction:

$$H_T(\omega) = c_{optical} \frac{\omega_T^2 / K_T}{\omega_T^2 - \omega^2 + i\omega\omega_T / Q_T} \tag{1.21}$$

where ω is the angular frequency, ω_T is the torsional resonance frequency, $c_{optical}$ is a scalar multiplier corresponding to the bending angle of the cantilever for a unit tip displacement in the torsional mode, Q_T is the quality factor of the torsional resonance, and K_T is the effective spring constant of the torsional resonance. Time resolved tapping force can be calculated based on this equation using the monitored torsional deflection signal. With approximately known vertical position of the tip, the force – displacement curve can be finally obtained and the Young's modulus can be calculated based on DMT model or Hertz model.

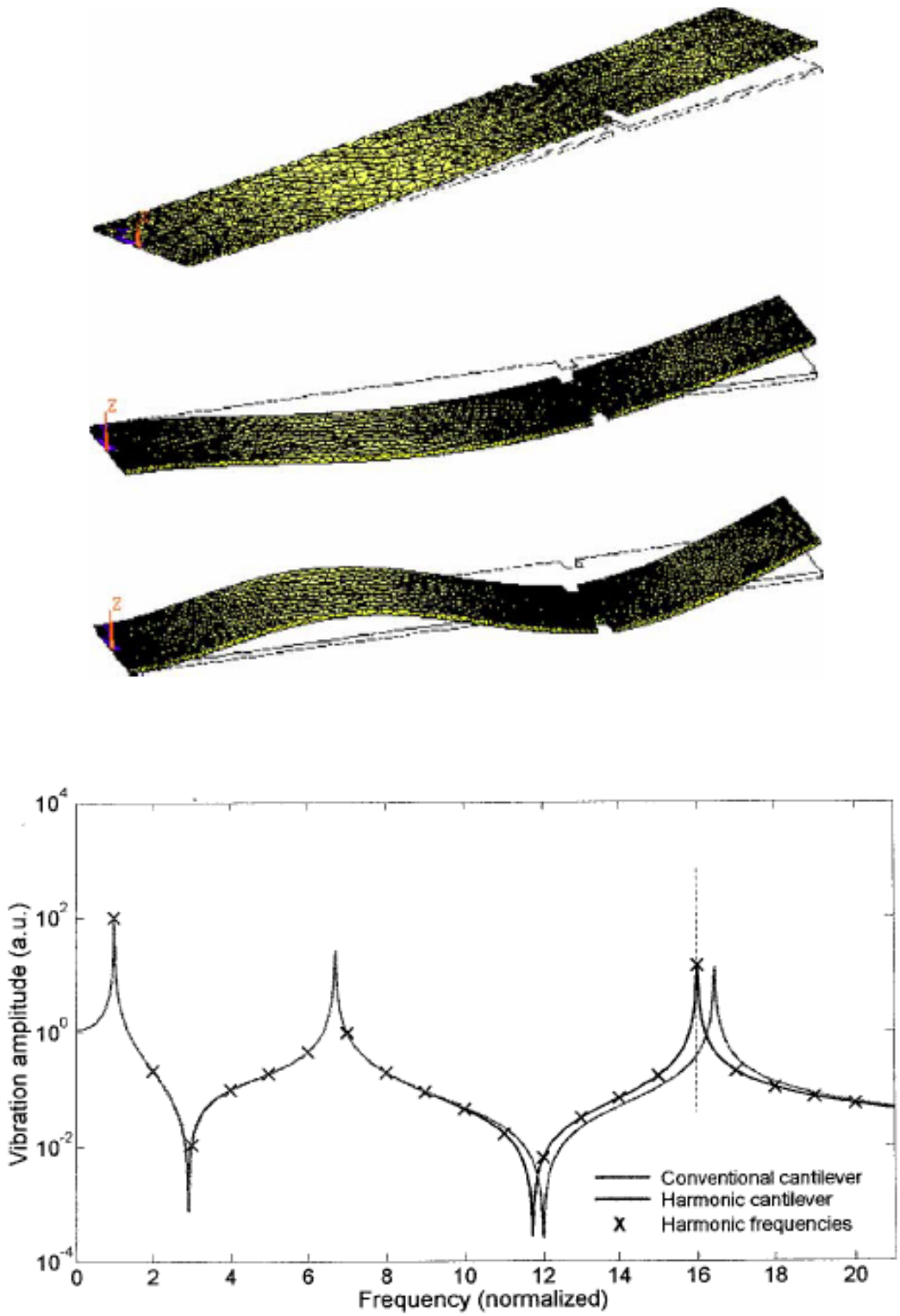

Figure 1.18 A specially designed harmonic cantilever with notch to have an integer ratio between the third and fundamental resonance frequencies. Figure copied from Ref. [23].

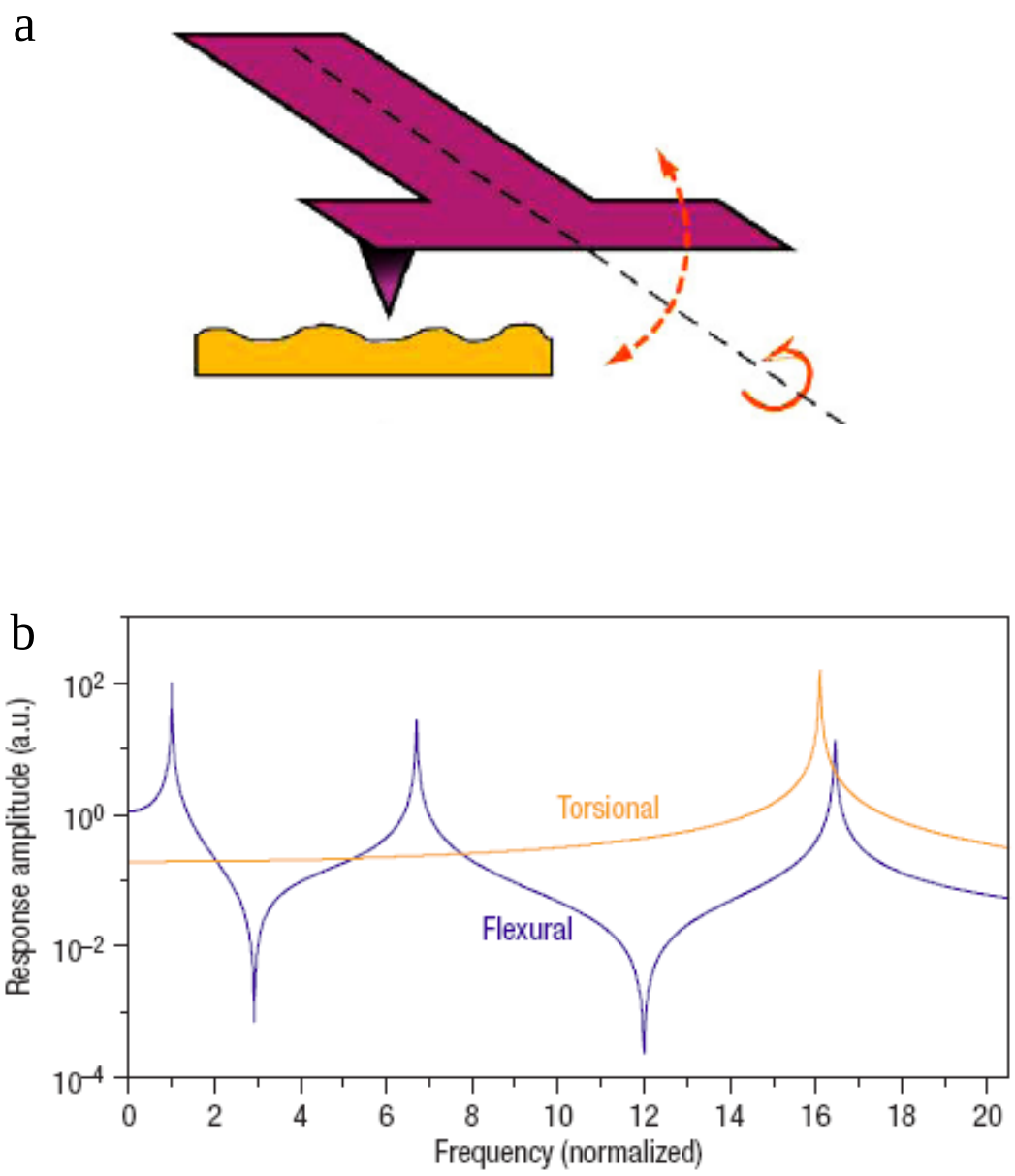

Figure 1.19 A specially designed harmonic cantilever with notch to have an integer ratio between the third and fundamental resonance frequencies: (a).Schematic diagram of T – shaped cantilever with an offset tip vibrating vertically at its resonance frequency. Tip – sample interactions twist the cantilever and generate torsional vibrations; (b). The frequency response of flexural and torsional modes of the T- shaped cantilever during tapping process. Figure copied from Ref. [22].

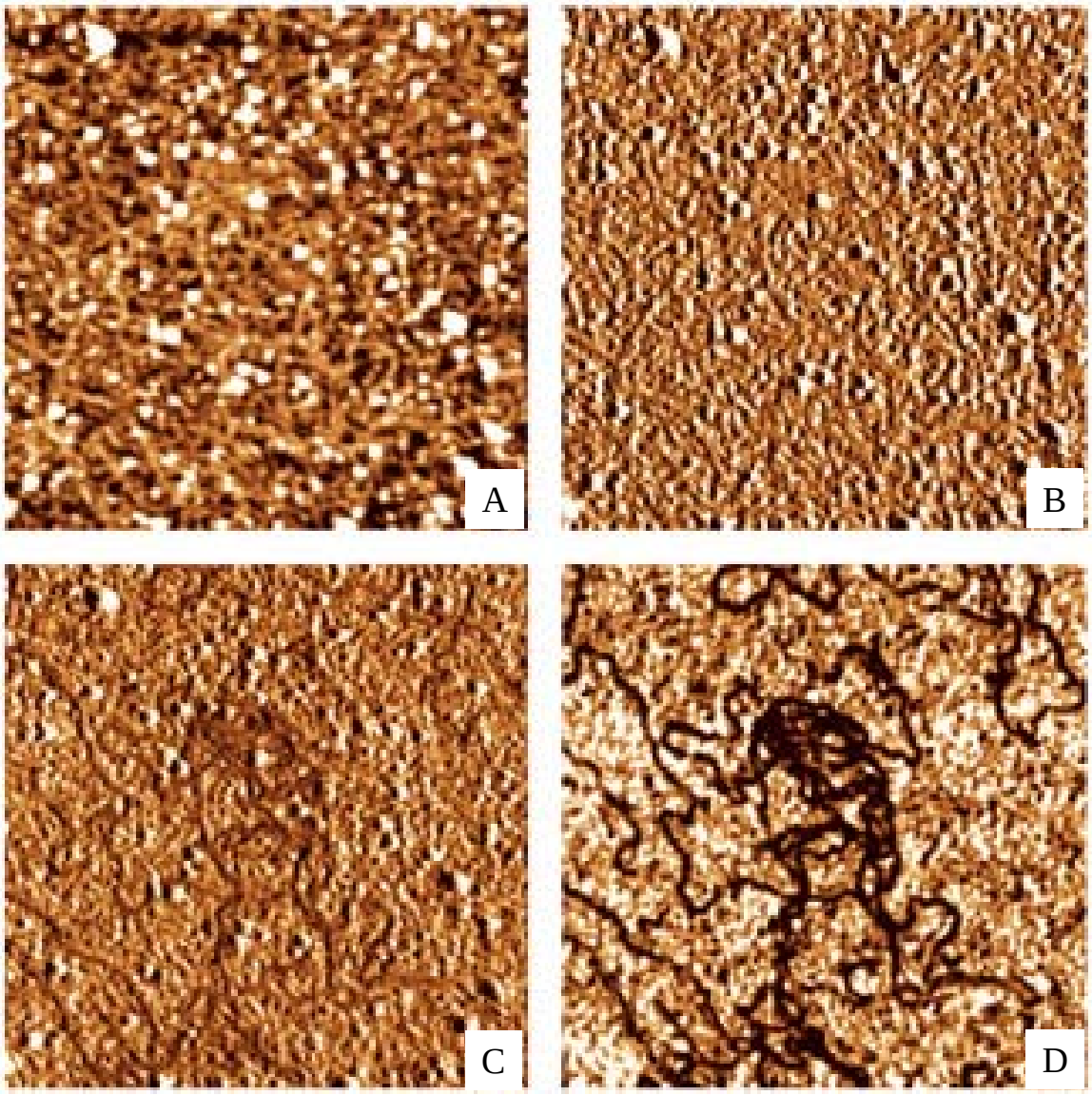

Figure 1.20 Multi-frequency AFM mode to image DNA in buffer: (a) the topography; (b) fundamental amplitude; (c) fundamental phase; (d) second mode amplitude. Figure copied from Ref. [79].

Higher – order flexural modes AFM has also been widely studied since very early work from[80] where the first resonance was for intermittent imaging and the second resonance was for sensing tip – sample force. Operating AFM mode at higher resonance not only improves the sensitivity to force gradients [24, 81] but also generates specific information about the surface properties [79, 82, 83]. Rodriguez and Garcia [84] first proposed the

multi-frequency mode whether the AFM cantilever was excited at the first two modes. In their simulation, they observed that the phase of second mode had a strong dependence on the chemical information about the surface. Proksch [79] experimentally implemented the multi-frequency AFM mode to study samples, such as imaging DNA in buffer: the fundamental resonance was driven and used as feedback for tip-sample positioning; and the second resonance was also driven and its amplitude was monitored for higher contrast of DNA image as shown in Figure 1.20(d). Xu et al. [85] demonstrated that, by driving cantilever at higher modes in liquid, its harmonics amplitudes had shown higher sensitivity to the mechanical property of the surface. In this thesis we will demonstrate our work on the sensitivity problem of AFM in higher – flexural mode and revisit and optimize the sensitivity enhancement.

1.5 SCOPE AND RESEARCH OBJECTIVES OF THESIS

The main purpose of our research is to improve, optimize and develop AFM to enhance its capabilities in the study of surface properties at nanometer scale. Three research objectives have to be accomplished with regarding contact mode, dynamic modes including tapping mode and higher – order mode, and lateral scanning mode, respectively. They cover most of AFM applications to probe physical and chemical properties of the surfaces along with their morphology imaging capabilities.

In Chapter 2, we study the static sensitivity of optic – lever AFM in a liquid environment. We are looking towards minimizing possible errors in the sensitivity calibration, especially when the buffer liquids are needed to be exchanged in real – time [86]. The modeling method starts from the idea on the variance of laser focus length due to inhomogeneous mediums, along the optical patch in liquid environment. A theoretical model has been established for determining the relationship between the sensitivities in ambient and in liquid. Through this study, the force curve based calibration of the detection sensitivity in ambient environment, which we are competent for, can also be utilized for determining the detection sensitivity in a liquid environment.

Although conventional force curve calibration method is generally used for calibrating AFM detection sensitivity, the optical – lever sensing technique of an AFM system is detecting the bending angle (inclination) rather than the deflection of a cantilever [35]. Therefore, in Chapter 3, we will first study such difference between sensitivities on contact mode and dynamic mode. A new method will be developed to accurately determine the dynamic sensitivity which correlates the amplitude of dynamic AFM modes with tip – sample interaction force. We will also revisit the calibration of spring constant of AFM cantilever [36, 46] based on thermal method, in which Lorentzian fit to the thermal spectrum of the cantilever at its fundamental resonance is generally applied.

The Chapter 4 is to develop an effective T – shape cantilever based lateral friction mode (in contact mode) to measure frictional property of the thin film or self-assembled monolayer, which is important for advanced applications in MEMS/NEMS tribology. Our method will overcome conventional difficulties to calibrate lateral spring constant and lateral sensitivity of AFM cantilever. It can also be developed as a chemical force microscopy to quantitatively distinguish the hydrophilic and hydrophobic groups on surface. We will further introduce an additional method through a lock-in monitoring on the buckling signal of the cantilever, which can be used to minimize the misalignment error of our method in measurement.

Chapter 5 presents an immediate application of AFM to study a hydrogen bombardment process. In this work, we chose n-$C_{32}H_{66}$ SAM as a model system because it can be easily prepared, with mixed domains of the stand-up and lie-down phases on a convenient substrate of native-SiO2/Si. With our modified atomic force microscopy (AFM), we characterized the heights and Young's modulus of these two domains. We then used the novel hyperthermal hydrogen induced crosslinking (HHIC) technique to form cross-linking C-C bonds and convert the SAM to a dense and cohesive network. AFM results confirm that the height of the stand-up phase was decreased drastically by HHIC but that lie-down phase changed little. The respective changes in Young's modulus are ~6.5 and ~1.0 GPa; the former is more than five times of the modulus of the virgin stand-up phase. Intriguingly, the surface roughness of the stand-up domains first increased with brief

HHIC treatments but became as smooth as the virgin domain after prolonged HHIC treatments.

In Chapter 6, we give a summary of the thesis, and highlight the contributions of our work in the development and application of AFM. Suggestions for future work are also outlined.

1.6 REFERENCES

1. Feynman, R.P., *There's Plenty of Room at the Bottom: An Invitation to Enter a New Field of Physics.* First Published in Engineering and Science maganzine, vol. XXIII, no. 5, 1960.
2. Cumings, J. and Zettl, A., *Low-friction nanoscale linear bearing realized from multiwall carbon nanotubes*. Science, 2000. **289**(5479): p. 602-604.
3. El-Sayed, M.A., *Some interesting properties of metals confined in time and nanometer space of different shapes*. Accounts of Chemical Research, 2001. **34**(4): p. 257-264.
4. Klinke, C., Hannon, J.B., Afzali, A., and Avouris, P., *Field-effect transistors assembled from functionalized carbon nanotubes*. Nano Letters, 2006. **6**(5): p. 906-910.
5. Link, S. and El-Sayed, M.A., *Spectral properties and relaxation dynamics of surface plasmon electronic oscillations in gold and silver nanodots and nanorods*. Journal of Physical Chemistry B, 1999. **103**(40): p. 8410-8426.
6. Lucas, M., Zhang, X.H., Palaci, I., Klinke, C., Tosatti, E., and Riedo, E., *Hindered rolling and friction anisotropy in supported carbon nanotubes*. Nature Materials, 2009. **8**(11): p. 876-881.
7. Wang, Z.L., Petroski, J.M., Green, T.C., and El-Sayed, M.A., *Shape transformation and surface melting of cubic and tetrahedral platinum nanocrystals*. Journal of Physical Chemistry B, 1998. **102**(32): p. 6145-6151.
8. Bao, Y.P., Wei, T.F., Lefebvre, P.A., An, H., He, L.X., Kunkel, G.T., and Muller, U.R., *Detection of protein analytes via nanoparticle-based bio bar code technology*. Analytical Chemistry, 2006. **78**(6): p. 2055-2059.
9. Alivisatos, P., *The use of nanocrystals in biological detection*. Nature Biotechnology, 2004. **22**(1): p. 47-52.
10. Qin, Y., Wang, X.D., and Wang, Z.L., *Microfibre-nanowire hybrid structure for energy scavenging*. Nature, 2008. **451**(7180): p. 809-U5.
11. Nam, K.T., Kim, D.W., Yoo, P.J., Chiang, C.Y., Meethong, N., Hammond, P.T., Chiang, Y.M., and Belcher, A.M., *Virus-enabled synthesis and assembly of nanowires for lithium ion battery electrodes*. Science, 2006. **312**(5775): p. 885-888.

12. Arico, A.S., Bruce, P., Scrosati, B., Tarascon, J.M., and Van Schalkwijk, W., *Nanostructured materials for advanced energy conversion and storage devices*. Nature Materials, 2005. **4**(5): p. 366-377.
13. Binnig, G., Quate, C.F., and Gerber, C., *Atomic Force Microscope*. Physical Review Letters, 1986. **56**(9): p. 930-933.
14. Binnig, G., Rohrer, H., Gerber, C., and Weibel, E., *Tunneling through a Controllable Vacuum Gap*. Applied Physics Letters, 1982. **40**(2): p. 178-180.
15. Muller, D.J. and Dufrene, Y.F., *Atomic force microscopy as a multifunctional molecular toolbox in nanobiotechnology*. Nature Nanotechnology, 2008. **3**(5): p. 261-269.
16. Binnig, G., Despont, M., Drechsler, U., Haberle, W., Lutwyche, M., Vettiger, P., Mamin, H.J., Chui, B.W., and Kenny, T.W., *Ultrahigh-density atomic force microscopy data storage with erase capability*. Applied Physics Letters, 1999. **74**(9): p. 1329-1331.
17. Raab, A., Han, W.H., Badt, D., Smith-Gill, S.J., Lindsay, S.M., Schindler, H., and Hinterdorfer, P., *Antibody recognition imaging by force microscopy*. Nature Biotechnology, 1999. **17**(9): p. 902-905.
18. Chasiotis, I. and Knauss, W.G., *Microtensile tests with the aid of probe microscopy for the study of MEMS materials*. Materials and Device Characterization in Micromachining Iii, 2000. **4175**: p. 96-103
19. Spinney, P.S., Collins, S.D., and Smith, R.L., *Solid-phase direct write (SPDW) of carbon via scanning force microscopy*. Nano Letters, 2007. **7**(6): p. 1512-1515.
20. Yang, F., Wornyo, E., Gall, K., and King, W.P., *Nanoscale indent formation in shape memory polymers using a heated probe tip*. Nanotechnology, 2007. **18**(28): p. 285302.
21. Sahin, O. and Erina, N., *High-resolution and large dynamic range nanomechanical mapping in tapping-mode atomic force microscopy*. Nanotechnology, 2008. **19**(44): p. 445717.
22. Sahin, O., Magonov, S., Su, C., Quate, C.F., and Solgaard, O., *An atomic force microscope tip designed to measure time-varying nanomechanical forces*. Nature Nanotechnology, 2007. **2**(8): p. 507-514.
23. Sahin, O., Yaralioglu, G., Grow, R., Zappe, S.F., Atalar, A., Quate, C., and Solgaard, O., *High-resolution imaging of elastic properties using harmonic cantilevers*. Sensors and Actuators a-Physical, 2004. **114**(2-3): p. 183-190.
24. Stark, R.W., Drobek, T., and Heckl, W.M., *Tapping-mode atomic force microscopy and phase-imaging in higher eigenmodes*. Applied Physics Letters, 1999. **74**(22): p. 3296-3298.
25. Hillenbrand, R., Stark, M., and Guckenberger, R., *Higher-harmonics generation in tapping-mode atomic-force microscopy: Insights into the tip-sample interaction*. Applied Physics Letters, 2000. **76**(23): p. 3478-3480.
26. Krotil, H.U., Stifter, T., Waschipky, H., Weishaupt, K., Hild, S., and Marti, O., *Pulsed force mode: a new method for the investigation of surface properties*. Surface and Interface Analysis, 1999. **27**(5-6): p. 336-340.
27. Stark, R.W. and Heckl, W.M., *Higher harmonics imaging in tapping-mode atomic-force microscopy*. Review of Scientific Instruments, 2003. **74**(12): p. 5111-5114.

28. Devasia, S., Eleftheriou, E., and Moheimani, S.O.R., *A survey of control issues in nanopositioning*. Ieee Transactions on Control Systems Technology, 2007. **15**(5): p. 802-823.
29. Su, C.M., *Industrial Perspectives of Afm Control*. Asian Journal of Control, 2009. **11**(2): p. 104-109.
30. Alexander, S., Hellemans, L., Marti, O., Schneir, J., Elings, V., Hansma, P.K., Longmire, M., and Gurley, J., *An Atomic-Resolution Atomic-Force Microscope Implemented Using an Optical-Lever*. Journal of Applied Physics, 1989. **65**(1): p. 164-167.
31. Meyer, G. and Amer, N.M., *Novel Optical Approach to Atomic Force Microscopy*. Applied Physics Letters, 1988. **53**(12): p. 1045-1047.
32. Sarid, D., *Scanning Force Microscopy with Applicaitons to Electric, Magnetic and Atomic Forces* 1994: Oxford: Oxford University Press.
33. Timoshenko, S., *Vibration Problems in Engineering, 4th Ed.* 1974: Wiley, New York.
34. Sader, J.E., Larson, I., Mulvaney, P., and White, L.R., *Method for the Calibration of Atomic-Force Microscope Cantilevers*. Review of Scientific Instruments, 1995. **66**(7): p. 3789-3798.
35. Butt, H.J. and Jaschke, M., *Calculation of Thermal Noise in Atomic-Force Microscopy*. Nanotechnology, 1995. **6**(1): p. 1-7.
36. Proksch, R., Schaffer, T.E., Cleveland, J.P., Callahan, R.C., and Viani, M.B., *Finite optical spot size and position corrections in thermal spring constant calibration*. Nanotechnology, 2004. **15**(9): p. 1344-1350.
37. Butt, H.J., Cappella, B., and Kappl, M., *Force measurements with the atomic force microscope: Technique, interpretation and applications*. Surface Science Reports, 2005. **59**(1-6): p. 1-152.
38. Radmacher, M., Fritz, M., Cleveland, J.P., Walters, D.A., and Hansma, P.K., *Imaging Adhesion Forces and Elasticity of Lysozyme Adsorbed on Mica with the Atomic-Force Microscope*. Langmuir, 1994. **10**(10): p. 3809-3814.
39. Rotsch, C. and Radmacher, M., *Mapping local electrostatic forces with the atomic force microscope*. Langmuir, 1997. **13**(10): p. 2825-2832.
40. AHassan, E., Heinz, W.F., Antonik, M.D., DCosta, N.P., Nagaswaran, S., Schoenenberger, C.A., and Hoh, J.H., *Relative micromechanical mapping of living cells by atomic force microscopy*. Molecular Biology of the Cell, 1997. **8**: p. 351-351.
41. Cleveland, J.P., Manne, S., Bocek, D., and Hansma, P.K., *A Nondestructive Method for Determining the Spring Constant of Cantilevers for Scanning Force Microscopy*. Review of Scientific Instruments, 1993. **64**(2): p. 403-405.
42. Golovko, D.S., Haschke, T., Wiechert, W., and Bonaccurso, E., *Nondestructive and noncontact method for determining the spring constant of rectangular cantilevers*. Review of Scientific Instruments, 2007. **78**(4): p. -.
43. Torii, A., Sasaki, M., Hane, K., and Okuma, S., *A method for determining the spring constant of cantilevers for atomic force microscopy*. Measurement Science & Technology, 1996. **7**(2): p. 179-184.

44. Gates, R.S. and Reitsma, M.G., *Precise atomic force microscope cantilever spring constant calibration using a reference cantilever array*. Review of Scientific Instruments, 2007. **78**(8): p. 086101.
45. Ohler, B., *Cantilever spring constant calibration using laser Doppler vibrometry*. Review of Scientific Instruments, 2007. **78**(6): p. 063701.
46. Hutter, J.L. and Bechhoefer, J., *Calibration of Atomic-Force Microscope Tips (Vol 64, Pg 1868, 1993)*. Review of Scientific Instruments, 1993. **64**(11): p. 3342-3342.
47. Hutter, J.L. and Bechhoefer, J., *Calibration of Atomic-Force Microscope Tips*. Review of Scientific Instruments, 1993. **64**(7): p. 1868-1873.
48. Levy, R. and Maaloum, M., *Measuring the spring constant of atomic force microscope cantilevers: thermal fluctuations and other methods*. Nanotechnology, 2002. **13**(1): p. 33-37.
49. Stark, R.W., Drobek, T., and Heckl, W.M., *Thermomechanical noise of a free v-shaped cantilever for atomic-force microscopy*. Ultramicroscopy, 2001. **86**(1-2): p. 207-215.
50. Schaffer, T.E., *Calculation of thermal noise in an atomic force microscope with a finite optical spot size*. Nanotechnology, 2005. **16**(6): p. 664-670.
51. Naeem, S., Liu, Y., Nie, H.Y., Lau, W.M., and Yang, J., *Revisiting atomic force microscopy force spectroscopy sensitivity for single molecule studies*. Journal of Applied Physics, 2008. **104**(11): p. 114504.
52. Liu, Y., Guo, Q.Q., Nie, H.Y., Lau, W.M., and Yang, J., *Optimization and calibration of atomic force microscopy sensitivity in terms of tip-sample interactions in high-order dynamic atomic force microscopy*. Journal of Applied Physics, 2009. **106**(12): p. 124507.
53. Mate, C.M., Mcclelland, G.M., Erlandsson, R., and Chiang, S., *Atomic-Scale Friction of a Tungsten Tip on a Graphite Surface*. Physical Review Letters, 1987. **59**(17): p. 1942-1945.
54. Liu, E., Blanpain, B., and Celis, J.P., *Calibration procedures for frictional measurements with a lateral force microscope*. Wear, 1996. **192**(1-2): p. 141-150.
55. Tocha, E., Song, J., Schonherr, H., and Vancso, G.J., *Calibration of friction force signals in atomic force microscopy in liquid media*. Langmuir, 2007. **23**(13): p. 7078-7082.
56. Cannara, R.J., Eglin, M., and Carpick, R.W., *Lateral force calibration in atomic force microscopy: A new lateral force calibration method and general guidelines for optimization*. Review of Scientific Instruments, 2006. **77**(5): p. 053701.
57. Bogdanovic, G., Meurk, A., and Rutland, M.W., *Tip friction - torsional spring constant determination*. Colloids and Surfaces B-Biointerfaces, 2000. **19**(4): p. 397-405.
58. Xie, H., Vitard, J., Haliyo, S., and Regnier, S., *Optical lever calibration in atomic force microscope with a mechanical lever*. Review of Scientific Instruments, 2008. **79**(9): p. 096101.
59. Schwarz, U.D., Koster, P., and Wiesendanger, R., *Quantitative analysis of lateral force microscopy experiments*. Review of Scientific Instruments, 1996. **67**(7): p. 2560-2567.

60. Liu, W.H., Bonin, K., and Guthold, M., *Easy and direct method for calibrating atomic force microscopy lateral force measurements*. Review of Scientific Instruments, 2007. **78**(6): p. 063707.
61. Cumpson, P.J., Hedley, J., and Clifford, C.A., *Microelectromechanical device for lateral force calibration in the atomic force microscope: Lateral electrical nanobalance*. Journal of Vacuum Science & Technology B, 2005. **23**(5): p. 1992-1997.
62. Jeon, S., Braiman, Y., and Thundat, T., *Torsional spring constant obtained for an atomic force microscope cantilever*. Applied Physics Letters, 2004. **84**(10): p. 1795-1797.
63. Ogletree, D.F., Carpick, R.W., and Salmeron, M., *Calibration of frictional forces in atomic force microscopy*. Review of Scientific Instruments, 1996. **67**(9): p. 3298-3306.
64. Oncins, G., Vericat, C., and Sanz, F., *Mechanical properties of alkanethiol monolayers studied by force spectroscopy*. Journal of Chemical Physics, 2008. **128**(4): p. 044701.
65. Muller, D.J., *AFM: a nanotool in membrane biology*. Biochemistry, 2008. **47**(31): p. 7986-7998.
66. Szlufarska, I., Chandross, M., and Carpick, R.W., *Recent advances in single-asperity nanotribology*. Journal of Physics D-Applied Physics, 2008. **41**(12): p. -.
67. Mo, Y.F., Turner, K.T., and Szlufarska, I., *Friction laws at the nanoscale*. Nature, 2009. **457**(7233): p. 1116-1119.
68. Noy, A., Vezenov, D.V., and Lieber, C.M., *Chemical force microscopy*. Annual Review of Materials Science, 1997. **27**: p. 381-421.
69. Zhong, Q., Inniss, D., Kjoller, K., and Elings, V.B., *Fractured Polymer Silica Fiber Surface Studied by Tapping Mode Atomic-Force Microscopy*. Surface Science, 1993. **290**(1-2): p. L688-L692.
70. Huang, L. and Su, C.M., *A torsional resonance mode AFM for in-plane tip surface interactions*. Ultramicroscopy, 2004. **100**(3-4): p. 277-285.
71. Burnham, N.A., Behrend, O.P., Oulevey, F., Gremaud, G., Gallo, P.J., Gourdon, D., Dupas, E., Kulik, A.J., Pollock, H.M., and Briggs, G.A.D., *How does a tip tap?* Nanotechnology, 1997. **8**(2): p. 67-75.
72. Magonov, S.N., Elings, V., and Whangbo, M.H., *Phase imaging and stiffness in tapping-mode atomic force microscopy*. Surface Science, 1997. **375**(2-3): p. L385-L391.
73. Tamayo, J. and Garcia, R., *Deformation, contact time, and phase contrast in tapping mode scanning force microscopy*. Langmuir, 1996. **12**(18): p. 4430-4435.
74. Tamayo, J. and Garcia, R., *Effects of elastic and inelastic interactions on phase contrast images in tapping-mode scanning force microscopy*. Applied Physics Letters, 1997. **71**(16): p. 2394-2396.
75. Cleveland, J.P., Anczykowski, B., Schmid, A.E., and Elings, V.B., *Energy dissipation in tapping-mode atomic force microscopy*. Applied Physics Letters, 1998. **72**(20): p. 2613-2615.
76. Radmacher, M., Tillmann, R.W., Fritz, M., and Gaub, H.E., *From Molecules to Cells - Imaging Soft Samples with the Atomic Force Microscope*. Science, 1992. **257**(5078): p. 1900-1905.

77. van Noort, S.J.T., Willemsen, O.H., van der Werf, K.O., de Grooth, B.G., and Greve, J., *Mapping electrostatic forces using higher harmonics tapping mode atomic force microscopy in liquid*. Langmuir, 1999. **15**(21): p. 7101-7107.
78. Giessibil, F.J., *Higher-harmonic atomic force microscopy*. Surface and Interface Analysis, 2006. **38**(12-13): p. 1696-1701.
79. Proksch, R., *Multifrequency, repulsive-mode amplitude-modulated atomic force microscopy*. Applied Physics Letters, 2006. **89**(11): p. 113121.
80. Minne, S.C., Manalis, S.R., Atalar, A., and Quate, C.F., *Contact imaging in the atomic force microscope using a higher order flexural mode combined with a new sensor*. Applied Physics Letters, 1996. **68**(10): p. 1427-1429.
81. Hoummady, M. and Farnault, E., *Enhanced sensitivity to force gradients by using higher flexural modes of the atomic force microscope cantilever*. Applied Physics a-Materials Science & Processing, 1998. **66**: p. S361-S364.
82. Zhang, J.B., Xi, N., Li, G.Y., and Su, C.M., *Atomic Force Microscopy sensing using multiple modes*. 2006 IEEE/RSJ International Conference on Intelligent Robots and Systems, Vols 1-12, 2006: p. 3928-3933
83. Bostanci, U., Abak, M.K., Aktas, O., and Dana, A., *Nanoscale charging hysteresis measurement by multifrequency electrostatic force spectroscopy*. Applied Physics Letters, 2008. **92**(9): p. 093108.
84. Rodriguez, T.R. and Garcia, R., *Compositional mapping of surfaces in atomic force microscopy by excitation of the second normal mode of the microcantilever*. Applied Physics Letters, 2004. **84**(3): p. 449-451.
85. Xu, X., Melcher, J., Basak, S., Reifenberger, R., and Raman, A., *Compositional Contrast of Biological Materials in Liquids Using the Momentary Excitation of Higher Eigenmodes in Dynamic Atomic Force Microscopy*. Physical Review Letters, 2009. **102**(6): p. 060801.
86. Kasas, S., Alonso, L., Jacquet, P., Adamcik, J., Haeberli, C., and Dietler, G., *Microcontroller-driven fluid-injection system for atomic force microscopy*. Review of Scientific Instruments, 2010. **81**(1): p. 013704.

CHAPTER 2
DETECTION SENSITIVITY OF AFM IN LIQUID*

Most AFM experiments require the accurate calibration of the optical lever sensitivity in order to obtain quantitative data. As we mentioned in Chapter 1, in ambient the calibration of AFM detection sensitivity can be done through fitting the slope of force curve, which is obtained by pressing the cantilever against a hard substrate. In liquid, although same method can be used, such as on a glass cover-slip, to introduce a hard substrate is not always the case to support samples and there are other biocompatible coatings with less stiffness. In addition, the use of an extra hard substrate can easily introduce contamination into the liquid environment, esp. for the biological application. Such problem is becoming significant for the applications with exchanging mediums during imaging or force mapping [1, 2]. Therefore, this chapter will discuss the calibration of AFM detection sensitivity in liquid environment and look forwards to providing theoretical and experimental demonstrations to establish the connection between detection sensitivities in air and in liquid.

2.1 INTRODUCTION

Since its invention in 1986 [3], atomic force microscopy (AFM) has been applied to imaging [4, 5], force measurement [6, 7], nanoindentation [8], hard-disk data storage [9] and nanolithography [10]. Recently, AFM has been extensively used in life science due to its high resolution in force measurement at the order of a picoNewton (pN) [11-15]. One of the most significant AFM applications is to probe protein – protein recognition by detecting their non-covalent intermolecular forces ranging from tens to several hundred pN, which is elusive for conventional force measurement artifices. In an optical-lever based AFM system[16, 17], the measurement resolution for height or force is linearly determined by its deflection sensitivity, which establishes a quantitative relationship between the displacement output d of the position sensitive detector (PSD) and the

* A modified version of this part has been published as: Liu, Y. and Yang, J., "Coupling Effects of Refractive Index Discontinuity, Spot Size and Spot Location on the Deflection Sensitivity of Optical-Lever Based Atomic Force Microscopy", Nanotechnology, 19, 2008, 235501.

cantilever deflection z. With the deflection amplified in geometric optics[18], AFM can effectively reflect a minute deflection of tip at the order of 0.1 nm even 0.01 nm [18, 19]. The deflection sensitivity is the key factor in the force measurement and the AFM spring constant calibration as well [20-22], which directly mediates reproducibility, repeatability and accuracy of protein–protein interaction assays. Therefore, a solid understanding of the deflection sensitivity would help the experimentalists to achieve AFM's best performance and improve the existing microscope design.

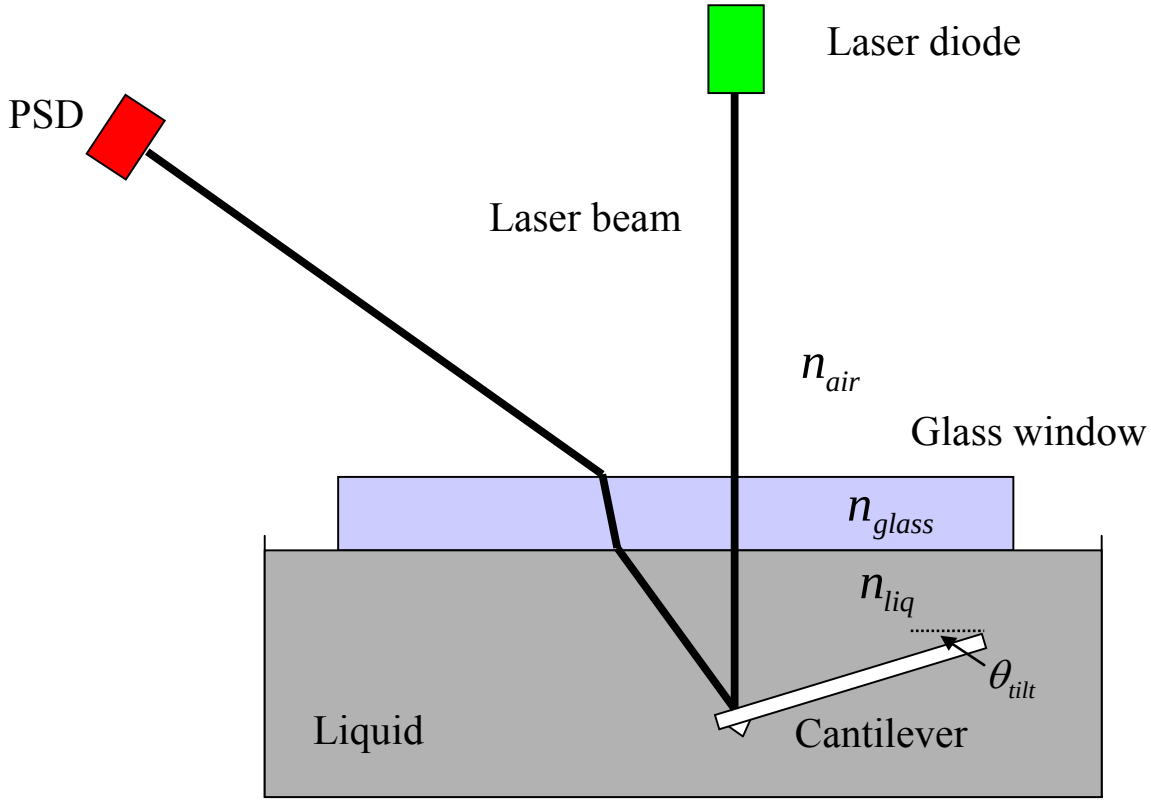

Figure 2.1 Schematic illustration of the AFM system in a liquid environment

Previous studies of AFM deflection sensitivity are mainly focused on hydrodynamic drag[23], thermal noise [24, 25] and electrostatic interaction[26]. Some researchers have recognized an enhancement of the deflection sensitivity from air to liquid in their experiments [27] and system design [28]. A general conclusion in their works is that in liquid environment the deflection angle of the cantilever is primarily determined and

virtually amplified by the index discontinuity at the liquid–air interface. Based on geometric optics, Tocha et al. [29] obtained analytically the quantitative relationship between the deflection sensitivity variance in normal and/or lateral force measurement and the ratio of refractive indices of liquid to air. In a typical liquid AFM system, along the laser light transmission path at least three different media are involved: air, liquid and glass window (sometime made of Teflon) with very high transparent quality, as shown in Figure 2.1. Advantages of the use of the glass window herein are: to reduce the effect of water fluctuation on light transmission; and to avoid the impact of surface tension which will bend the air–liquid interface, and consequently deviates the light reflected from cantilever. However, the use of the glass window also results in an additional refractive index discontinuity at the air–glass and glass–liquid interfaces. As a result, the discontinuity induces variations of laser spot size and spot location on the cantilever, both of which are directly related to the deflection sensitivity [30-32]. In this paper, we will conduct a systematical study of the coupling effects of the refractive index discontinuity between the three media, the laser spot size and the spot location on the deflection sensitivity of AFM.

2.2 THEORY

2.2.1. Extended Focal Length

In this study, the irradiation distributions of the laser spot on both the cantilever and PSD are assumed to be of Gaussian shape [18, 24]. In air, the laser beam, passing through a focus lens, is focused at the 'cantilever plane', as specified in Figure 2.2[18]. The corresponding focused spot size on the cantilever plane is w_0 (measured between the $1/e^2$ irradiance points) as shown in Figure 2.3. However, in a liquid environment the focus of lens has been shifted from the 'cantilever plane' to 'plane 1' because of the discontinuity of refractive indices at the air–glass interface and the glass–liquid interface, as shown in Figure 2.2. To calculate the shift displacement ΔL_1, we first assume the refractive index of liquid to be equal to that of glass and then consider the divergence angle η_1 of the laser beam in air before the laser passes through the air–glass interface at a distance ($h_1 + h_2$) from the cantilever plane: h_1 is the layer thickness of the cover glass

and h_2 is the layer thickness of the liquid[33]:

$$\tan\eta_1 = \frac{\lambda f}{\pi w_0^2 n_{air}} \tag{2.1}$$

where h_2 is the laser wavelength in air; f is the focal length of the focus lens which is commonly installed in a commercial AFM system suitable for the use of small cantilevers. Based on the ray matrix [33] at the air–glass interface, the divergence angle η_2 after the laser has passed the air–glass interface becomes

$$\tan\eta_2 = \tan\eta_1 \frac{n_{air}}{n_{glass}} \tag{2.2}$$

where n_{air} and n_{glass} are the refractive indices for air and glass, respectively.

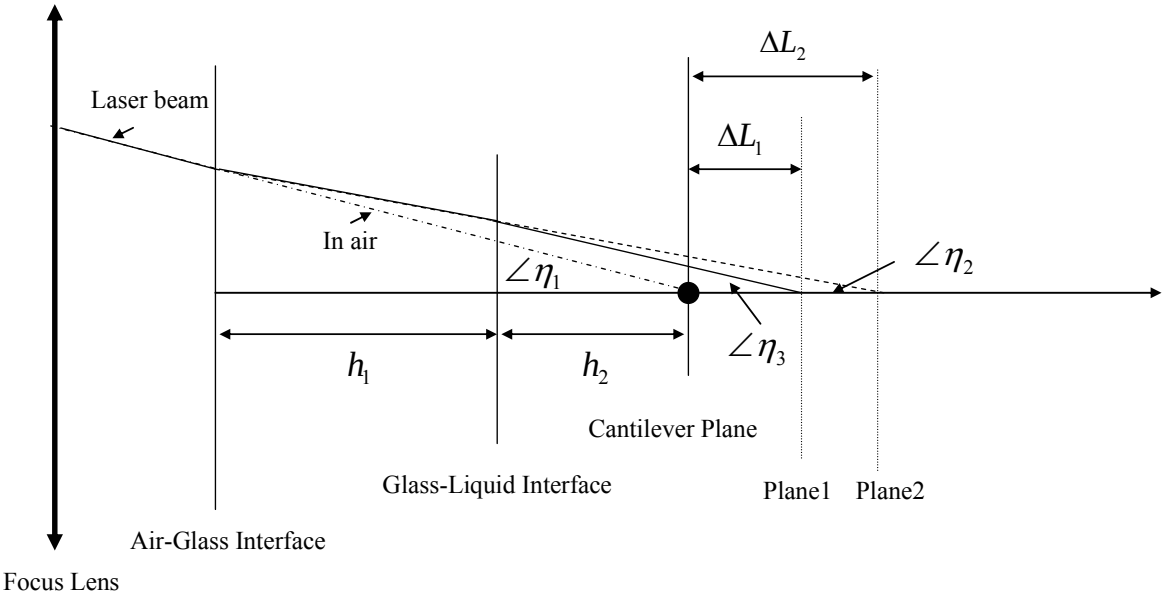

Figure 2.2 Schematic illustration of the focal length being extended by the refractive index discontinuity

The extended focal length ΔL_2 is defined as

$$\Delta L_2 = \frac{(h_1 + h_2)\tan\eta_1}{\tan\eta_2} - (h_1 + h_2) = (h_1 + h_2)\frac{n_{glass} - n_{air}}{n_{air}} \tag{2.3}$$

The laser is shifted and focused on ‘plane 2’ not on the ‘cantilever plane’. However, n_{liq}

is indeed different from n_{glass}, so the laser should be finally focused on 'plane 1' and the correspondingly increased focal length ΔL_1 is given by

$$\Delta L_1 = h_2 \frac{n_{liq} - n_{glass}}{n_{glass}} + \Delta L_2 \frac{n_{liq}}{n_{glass}} \tag{2.4}$$

where n_{liq} is the refractive index of the liquid. Therefore, in liquid environment, the focal length of the lens is extended by ΔL_1, depending on the discontinuity of the refractive indices, coupled with the layer thickness h_1 and h_2. Directly, the extended focal length alters the spot size on the back face of the cantilever, to be discussed next.

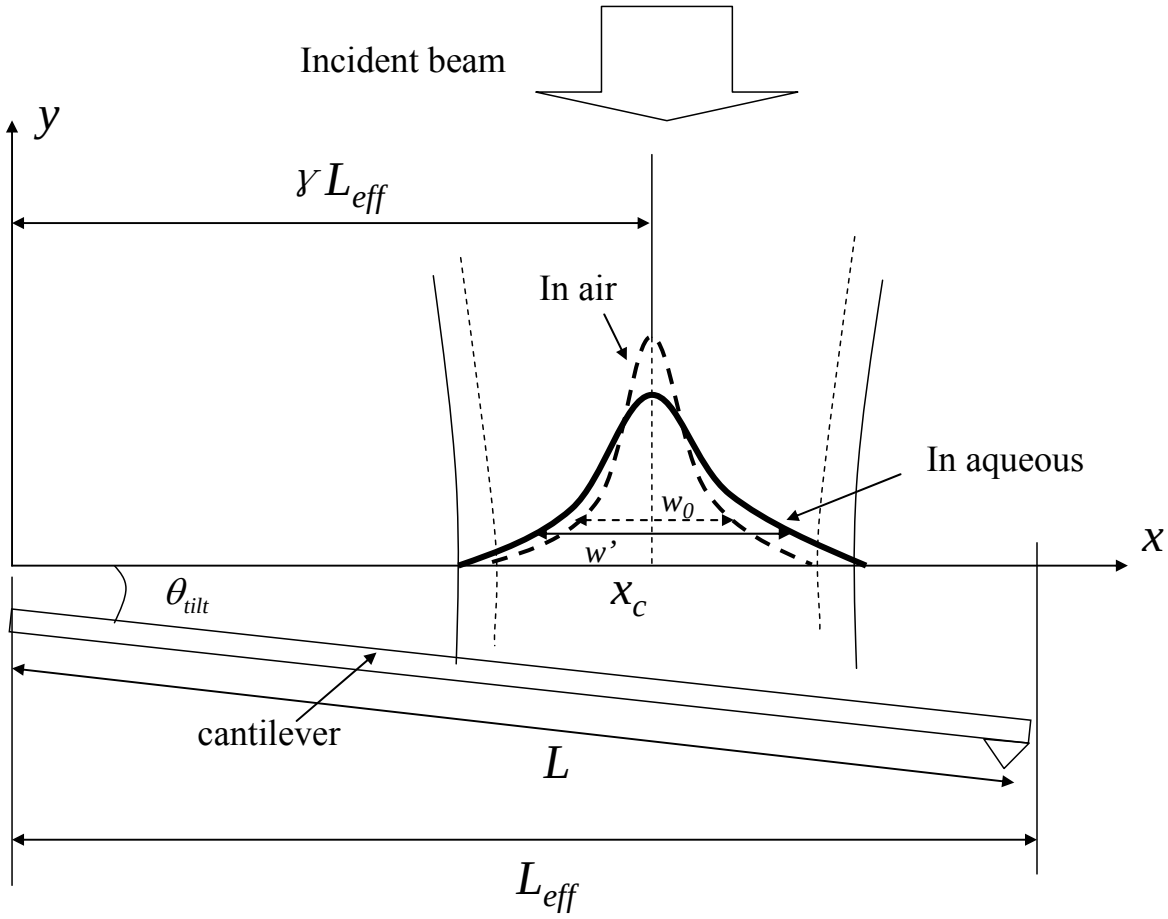

Figure 2.3 Schematic of irradiation distribution of Gaussian beam spot on the tilted cantilever: the dashed curve represents the beam profile in air with spot size w_o at the x – axis and the solid curve represents the beam profile in liquid environment with spot size w' at the x – axis.

2.2.2 Spot Size and Deflection Sensitivity

Regardless of being in air or in a liquid environment, the numerical aperture (NA) of the focus lens does not change, according to Snell's law:

$$\mathrm{NA} = n\sin\phi = D/2f \tag{2.5}$$

where ϕ is the converging angle and D is the effective diameter of the focus lens, which is also the collimated laser beam diameter before focusing. The diameter w_0 of the focused Gaussian beam at its focus is defined as [34]

$$w_0 = \frac{4}{\pi}\frac{f\lambda}{D} = \frac{4}{\pi}\frac{\lambda}{2\mathrm{NA}} \tag{2.6}$$

Therefore, the focal spot size is independent of the refractive index of the medium through which the laser beam is transmitted. In the light of concerns of the spot size on the cantilever plane, in liquid the spot diameter w' becomes [33, 35]

$$w' = w_0\left\{1+\left(\frac{4\lambda}{\pi}\frac{\Delta L_1}{(w_0)^2 n_{liq}}\right)^2\right\}^{1/2} \tag{2.7}$$

where w_0 and w' are the spot sizes along x-axis at $1/e^2$ irradiance points in air and in liquid environments, respectively. It is noticed that when the liquid phase and the glass windows are involved the spot size on the 'cantilever plane' is increased, as shown in Figure 2.4. This is still valid when the cantilever tilts at an angle in the range 7° ~ 20° [36] As shown in Figure 2.3 the one-dimension irradiance distribution of a Gaussian beam (generally assumed) along x is [30-32]

$$I(x) = \sqrt{\frac{8}{\pi}}\frac{P_0}{w'}\exp\left(\frac{-8(x-x_c)^2}{w'^2}\right) \tag{2.8}$$

where P_0 is the total power from the laser diode and $x_c = \gamma L_{eff}$ is the center location of the Gaussian spot along x-axis, with γ standing for the relative location on the cantilever ($0 < \gamma < 1.0$) and L_{eff} being the effective cantilever length, equal to $L\cos\theta_{tilt}$ [30].

Correspondingly, the scalar wave function is [31]

$$E(x)=\sqrt{\sqrt{\frac{8}{\pi}}\frac{P_0}{w'}}\exp\left(\frac{-4(x-x_c)^2}{w'^2}\right) \tag{2.9}$$

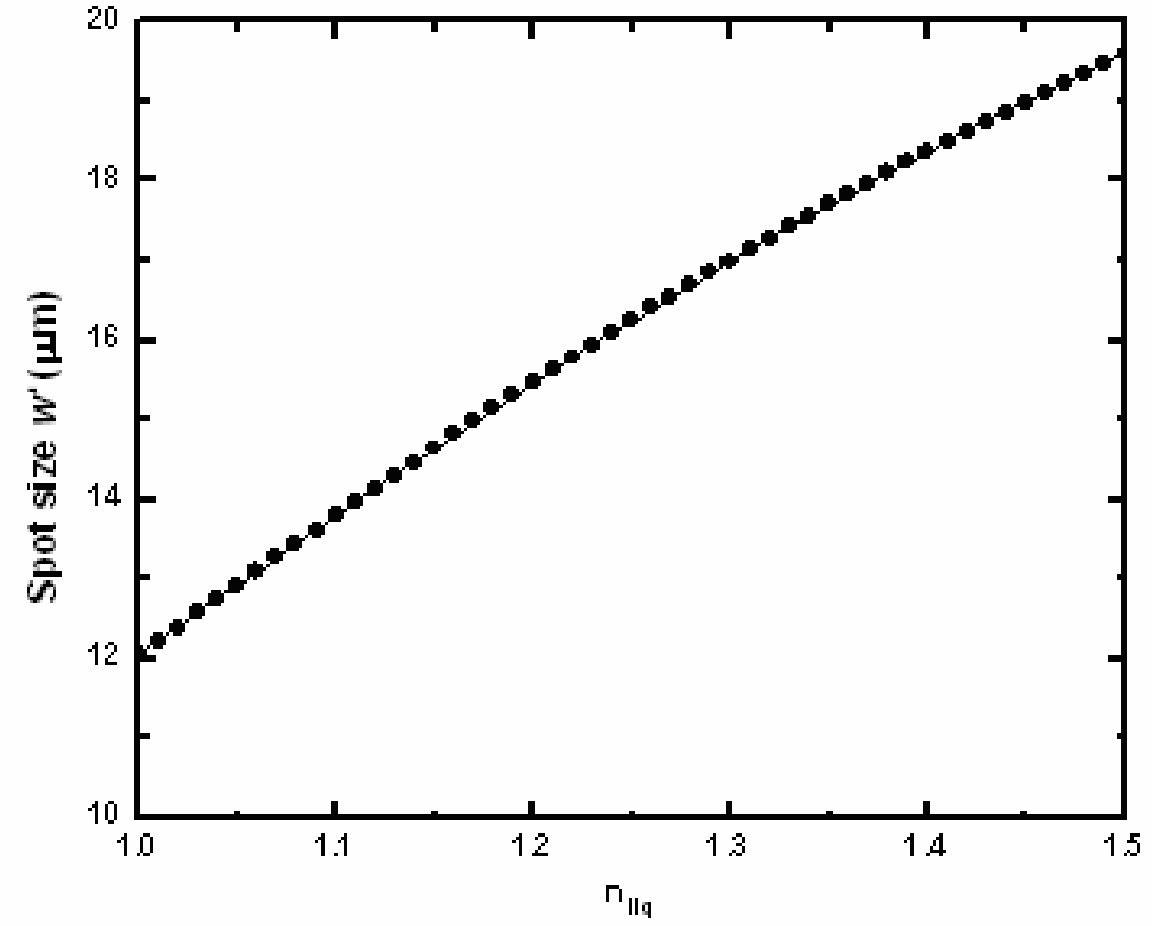

Figure 2.4 Effects of the liquid refractive index on spot size w' with $w_0 = 10\mu m$ and other parameters $h_1 = 1.0mm$, $h_2 = 1.5mm$, $n_{liq} = 1.3$, $n_{glass} = 1.55$ and $\lambda = 635nm$.

The difference signal of the optic lever deflection AFM system is given by Equation (10) of [30]

$$S = z_{eff}\frac{4\alpha}{\lambda}\int_0^{L_{eff}} dx\int_0^{L_{eff}} dx'E(x)E(x')\frac{h(x)-h(x')}{x-x'} \tag{2.10}$$

where α is the loss factor for power transmission (set as 0.9), and $h(u)$ is the normalized shape function for a deflected beam under static end-loading as defined by [30]

$$h(u) = \frac{3u^2 L_{eff} - u^3}{2L_{eff}^3} \tag{2.11}$$

Then the deflection sensitivity is defined as

$$\sigma = \frac{S}{z} \tag{2.12}$$

In a liquid environment, the discontinuity of refractive indices at the glass-liquid interface and the air-glass interface distorts the transmitting path of the laser beam as shown in Figure 2.1. There is a relationship between z, which is the deflection in air detected by the PSD, and z_{eff}, which is the effective deflection detected by the PSD due to the refraction in the liquid environment:

$$z_{eff} = \frac{\cos 2\theta_{tilt}}{\sqrt{\left(\frac{n_{air}}{n_{liq}}\right)^2 - \sin^2 2\theta_{tilt}}} z \tag{2.13}$$

As a result, Equation (12) defining the deflection sensitivity in liquid should be written as

$$\sigma = \frac{S}{z} = \frac{\cos 2\theta_{tilt}}{\sqrt{\left(\frac{n_{air}}{n_{liq}}\right)^2 - \sin^2 2\theta_{tilt}}} \frac{4\alpha}{\lambda} \int_0^{L_{eff}} dx \int_0^{L_{eff}} dx' E(x) E(x') \frac{h(x) - h(x')}{x - x'} \tag{2.14}$$

To investigate the variation of the deflection sensitivity in liquid environment relative to that in air, we further define the ratio

$$R = \frac{\sigma_{liq}}{\sigma_{air}} \tag{2.15}$$

2.3 RESULTS AND DISCUSSIONS

2.3.1 Coupled Effects

We set the cantilever length L = 200 μm, cantilever titled angle $\theta_{tilt} = 10°$ [36], the focused spot size as $w_0 = 10$ μm and $\gamma = 0.9$. From Figure 2.5, the deflection sensitivity is nearly linearly increased with the increase of n_{liq} and h_2, as well as the increase of n_{glass} and h_1. Moreover, the dependence of the linear trend on n_{liq} is stronger than that on

n_{glass} from the view of the slopes of curves. However it is not practical to enhance the detection sensitivity by solely increasing these parameters (n_{liq}, h_2, n_{glass} and h_1) because we also need to consider the enlarged spot size w' on the cantilever due to refraction. Based on Equation (7), to some extent the spot size w' is larger than the cantilever width, especially when small cantilevers used. Thus part of the laser spot is located out of the cantilever and the power received by PSD is less, and consequently the sensitivity is degraded.

In practice, there is some laser power loss for several reasons, including the partly reflected laser wave at the interface, diffraction along the transmission path and imperfect reflection from the back face of the cantilever. In the present study the power loss factor α is set as 0.9 for all cases. From Figure 2.5, it is noticed that if the refractive index n_{liq} for the liquid is fixed, increasing n_{glass} could enhance the deflection sensitivity. However, if α is assumed as 0.8, when n_{glass} = 1.5 and n_{liq} = 1.3, R is 1.66, less than 1.88 for n_{glass} = 1.3. As a result, the deflection sensitivity is degraded. To minimize the power loss, the experiment should be implemented by blocking possible contamination in the liquid medium, keeping the surfaces of the glass window and the cantilever clean, and using smaller h_1 and h_2 to reduce the dominant effect of diffraction, although they may enhance the deflection sensitivity (see Figure 2.5).

The influence of spot size w_0 on the deflection sensitivity with different combinations of refractive indices for glass and liquid is shown in Figure 2.6. When w_0 is smaller than the critical value w_c (~ 25 μm), R increases with the decrease of w_0. When w_0 is larger than a critical value w_c, R is independent on the spot size. The reason is that the variation of Gaussian spot size due to refraction is negligible compared to its original size $w_0 (> w_c)$, so that the major influence on the deflection sensitivity comes from the power loss α. If n_{liq} is fixed (e.g. $n_{liq} = 1.3$ in Figure 2.6) and the spot size is bigger than the critical value, R becomes independent of n_{glass}. Intriguingly, R could become smaller than

1.0. In other words, the deflection sensitivity may be degraded for the cases of $n_{liq} \to n_{air}$ (e.g. in Figure 2.6).

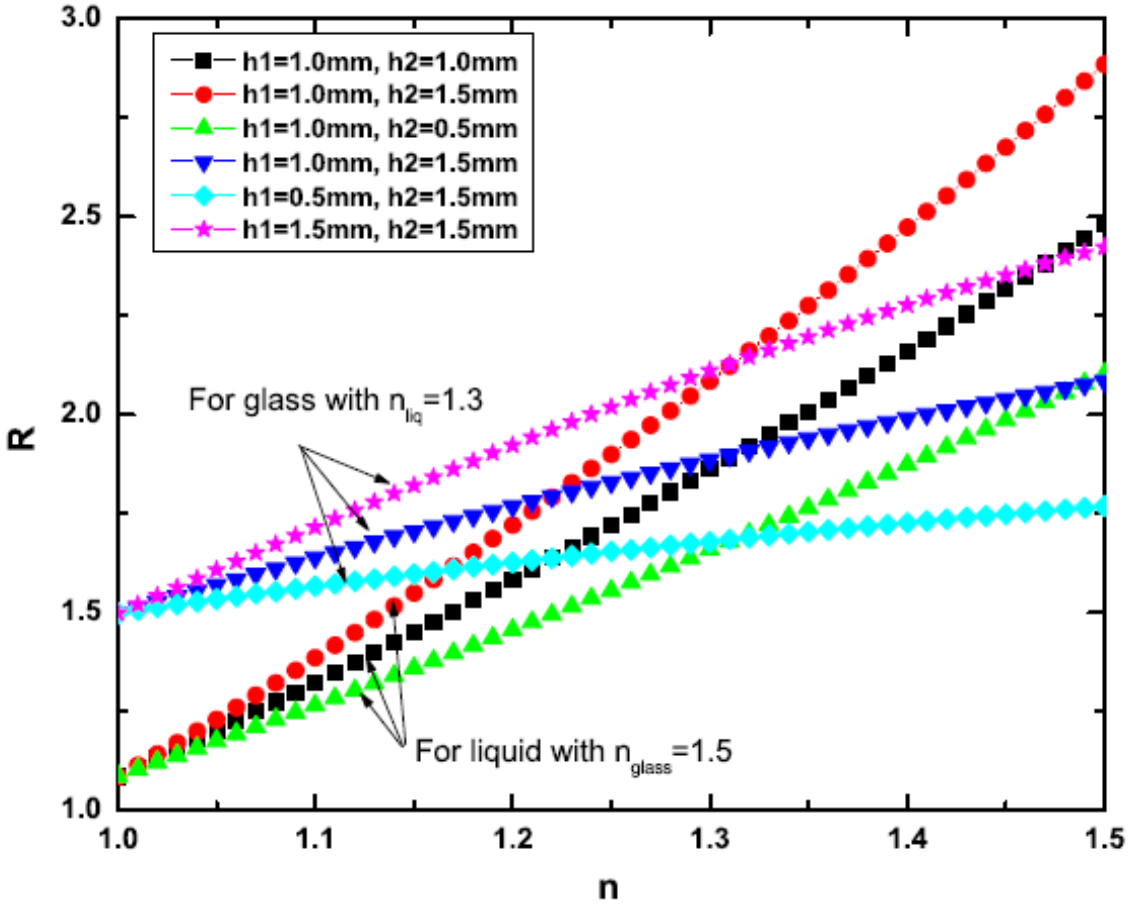

Figure 2.5 Effects of the glass and liquid refractive indices on R with different combination of the glass layer thickness h_1 and the liquid layer thickness h_2.

Although the liquid's refractive index n_{liq} is rarely smaller than 1.1, it is of general interest to study the coupling effect by covering a wide range of liquid refractive index. On the other hand, some AFM experiments may be conducted in a specific gas/vapour environment. For instance, samples are placed in a glass enclosure which is full of a specific gas/vapour. The index of the specific gas/vapour is likely to be in the range from 1.0 to 1.1. Our analysis of index discontinuity will be applicable for this case. As shown in Figure 2.6, when $1.0 < n_{glass} < 1.1$, there is a transition of the deflection sensitivity

from enhancement ($R > 1.0$) to degradation ($R < 1.0$), which also depends on the spot size w_0. Therefore, whether the deflection sensitivity is enhanced or decreased (R is larger or smaller than 1.0) is determined by the coupled effect of the refractive indices of the air–glass–liquid system, spot size w_0 and power loss factor α.

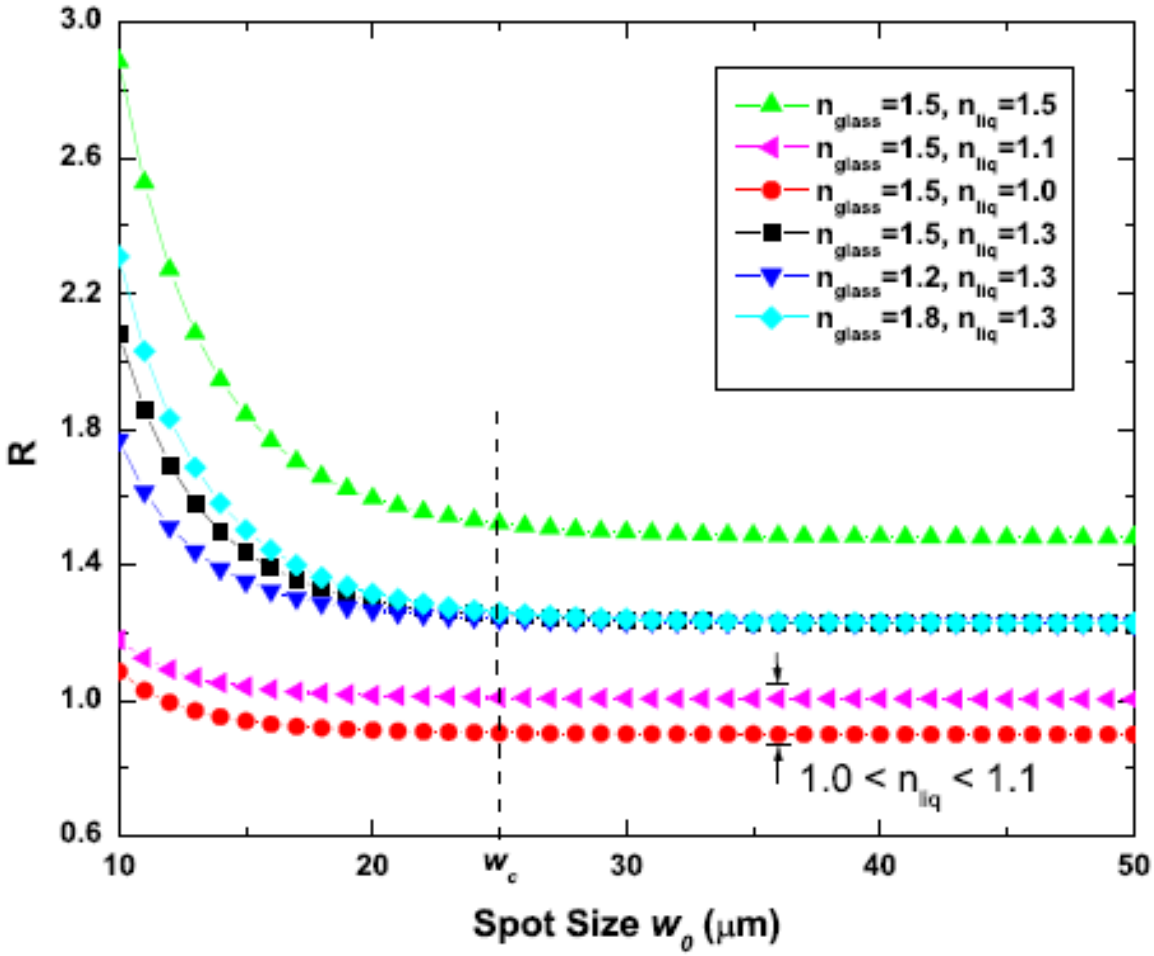

Figure 2.6 Effects of the spot size w_0 on R with different combination of refractive indices for glass and liquid for $h_1 = 1.0\,mm$ and $h_2 = 1.5\,mm$. When the spot size is bigger than a critical value w_c (~25 μm), R is independent of the spot size and the refractive index of the glass, but mainly determined by the refractive index of the liquid.

If both n_{liq} and n_{glass} are fixed, for example 1.3 and 1.5, respectively, a higher deflection sensitivity can be reached from a smaller spot size. The smaller focused laser spot on the

cantilever can be obtained through using a lens with a higher numeric aperture (NA) (see Equation (6)). Another method, introduced by Schäffer and Hansma[30], is to use an adjustable aperture to increase the effective diameter *D* (Equation (6)) of the focus lens and thus reduce the spot size for a fixed focal length *f*. In practice, there is another issue regarding the shot noise of the PSD [18, 35]. As a result, the signal–to–noise ratio (SNR) [35]should be considered. Using a smaller focused spot size is not always a preferable choice, since the SNR is highest when the focused spot size is matched to the cantilever size[30, 35]. In other words, a smaller cantilever with a smaller focused spot size should be employed for a higher SNR, and therefore higher deflection sensitivity is achieved.

In addition, as shown in Figures 2.7(a) and (b), the location γ of the laser spot on the back face of the cantilever also plays a role in influencing the deflection sensitivity. Here γ is in the range [0.1, 0.9] with the spot size w_0 set as 10 μm. When the refractive indices for both the glass and the liquid remain constant, *R* decreases and finally approaches a constant value when the spot location moves from the cantilever base to its end, as shown in Figure 2.7(b). Nevertheless, we also notice that the influence of spot location on the deflection sensitivity is much less significant than that of the spot size by comparing Figure 2.6 with Figure 2.7(a).

2.3.2 Experiments

The measurement of the deflection sensitivity was carried out on an atomic force microscope (XE-100, PSIA Inc., USA) in air (n_{air} = 1.0) and in deionized water (n_{liq} = 1.33) with a glass window (n_{glass} = 1.55) installed on a probe holder, which holds rectangular cantilever (ContAl, BudgetSensors, Inc.). A group of force–displacement curves was acquired for air and liquid at different spot locations on the cantilever. The spot location on the cantilever can be adjusted by a micrometer screw gauge with readings. Power loss factor α is the ratio of the total electric voltage output of the PSD in liquid to that in air. Finally, sensitivities were determined by the linear slopes of the force–displacement curves at the different locations of the laser spot. For each location, the experimental results for *R* are displayed in Figure 2.8. From this figure, it is noticed

that the experimental results for R are generally smaller than the predicated value (= 1.41) in [29] for the case of water but close to the predicated value based on our calculation (equations (14) and (15)), regarding the coupling effects from the refractive discontinuity, spot size and spot location.

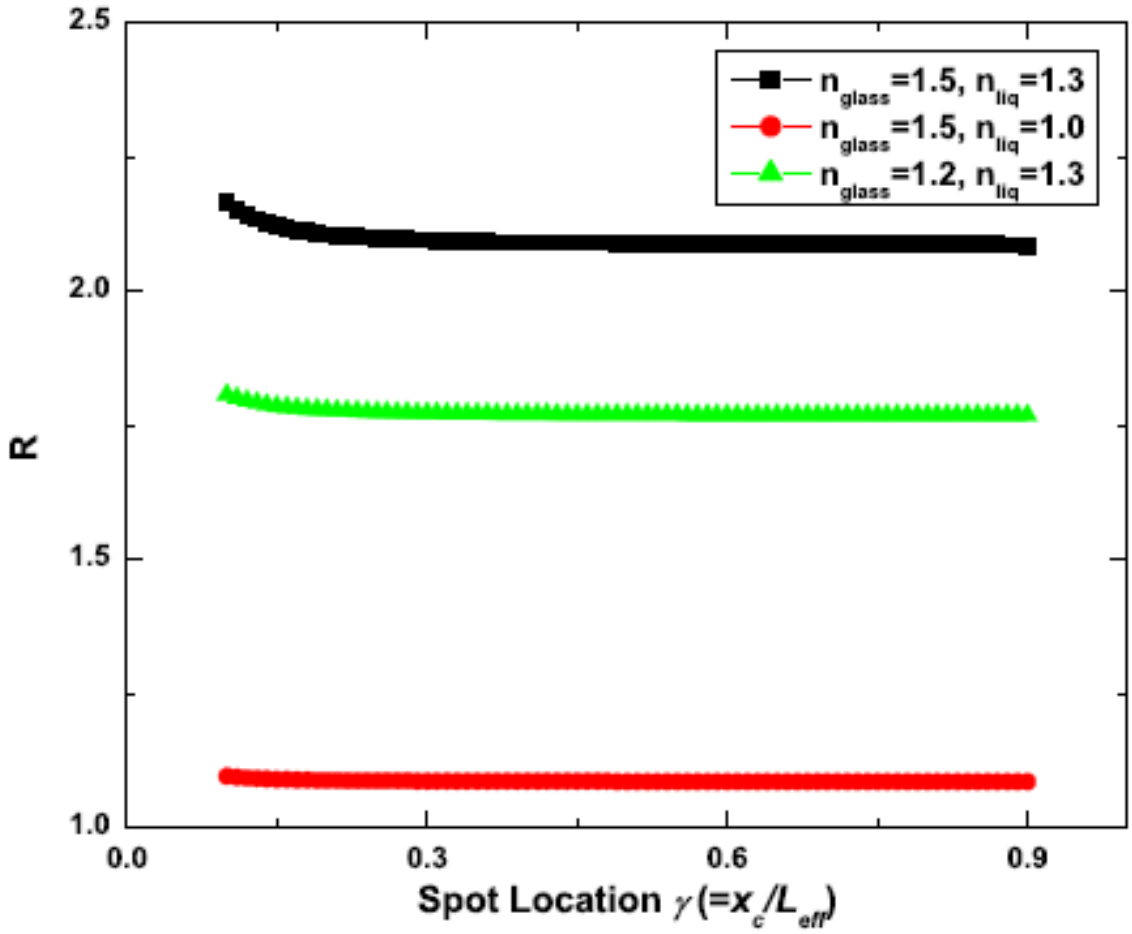

(a)

Figure 2.7 (Continued)

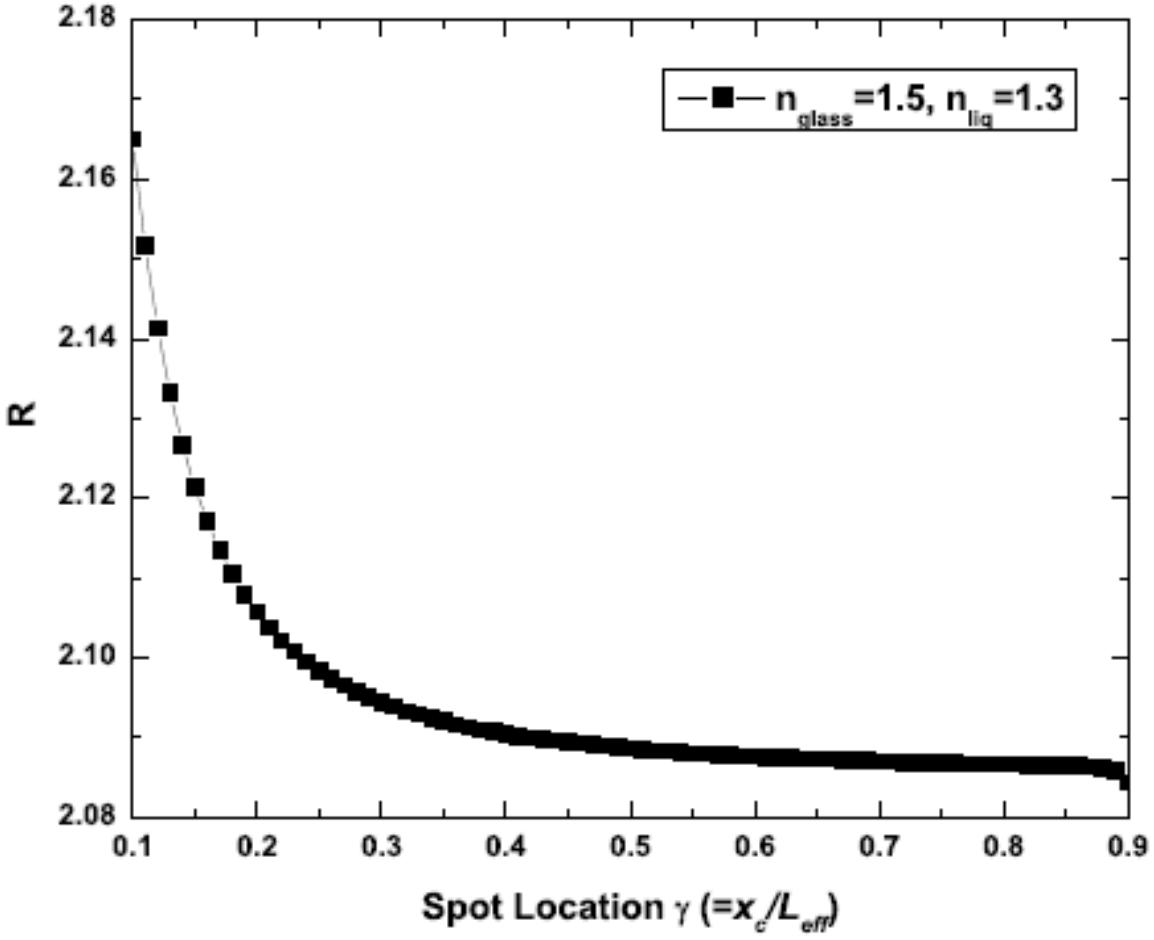

(b)

Figure 2.7 The influence of spot relative location $\gamma = x_c / L_{eff}$ on R for $w_0 = 10\mu m$, $h_1 = 1.0mm$, and $h_2 = 1.5mm$; (a) with different combination of refractive indices of glass and liquid; (b) enlarged view for the case of $n_{glass} = 1.5$, and $n_{liq} = 1.3$.

2.3.3 Further Discussion

As discussed in previous sections, this study is potentially beneficial to optimizing AFM design with better accuracy in both force measurement and imaging. On the other hand, this work is also useful in optimizing experimental procedures. For some AFM biological applications (e.g. an AFM cantilever array [37, 38] being used for screening biomolecular recognition or protein–drug interactions above numbers of microwells of a microarray), one may inject or perfuse different biological buffers during the experiment [1, 39, 40]. These biological buffers likely have different refractive indices. In this case, this study

can predict the variation of the deflection sensitivity due to the change of medium, and therefore remove the necessity of time-consuming re-alignment of the laser spot on the cantilever and re-calibration of the deflection sensitivity for different liquids. In addition, instead of performing such calibration at the beginning of an AFM experiment in liquid, one may calibrate the deflection sensitivity in air before or after the AFM experiment, since some biological experiments may be sensitive to operating time.

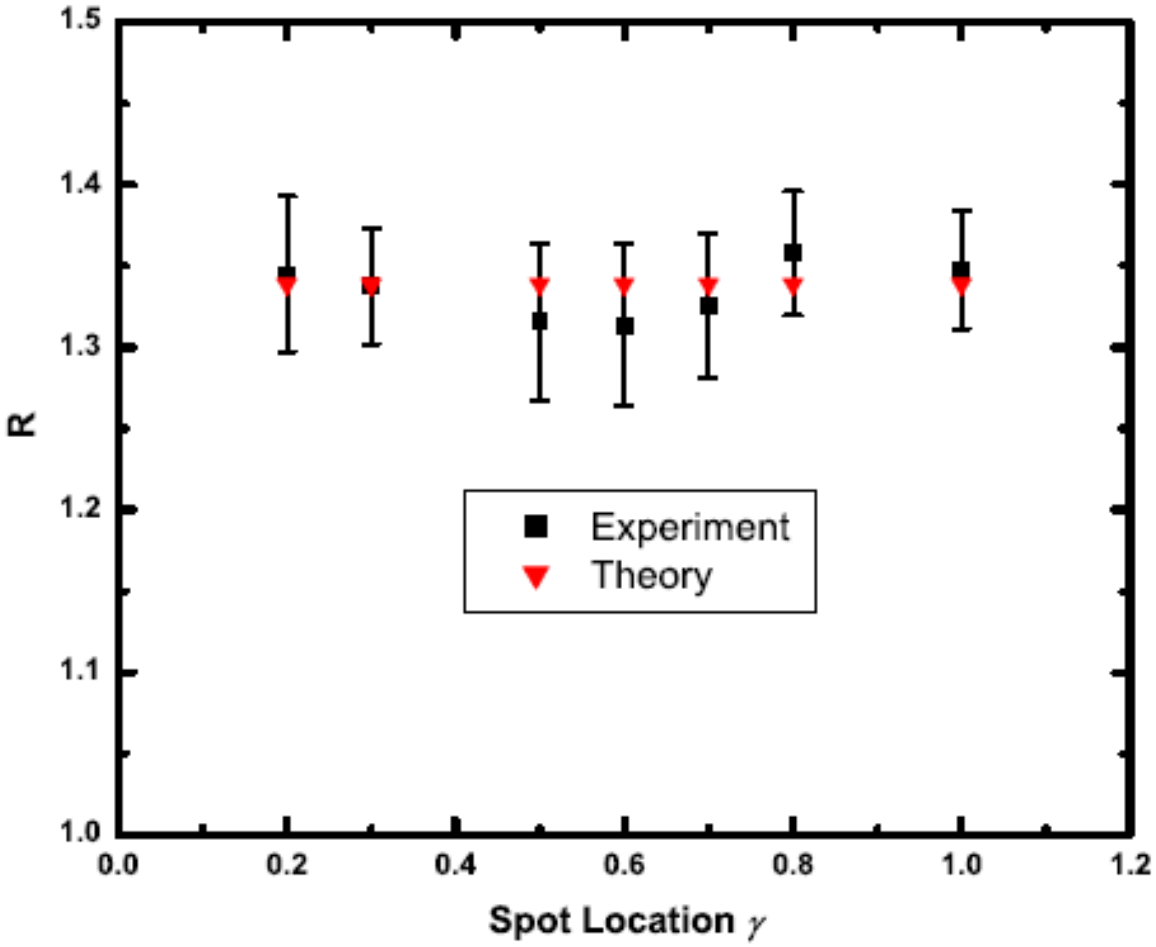

Figure 2.8 Comparison between experimental and theoretical results for *R* at different spot locations γ.

2.4 SUMMARY

In summary, the deflection sensitivity is a critical parameter for both imaging and force measurement in liquid environments by optical-lever based AFMs. The deflection

sensitivity can be enhanced or degraded depending on the coupling effects of the refractive index discontinuity, laser spot size and spot location. This study could potentially help us design high accuracy AFM systems and improve the resolution of force measurement in biological liquid environments. In addition, imaging resolution in liquid environments may also be further improved by maximizing the deflection sensitivity through an optimal design of the air–glass–liquid system.

2.5 REFERENCES

1. Kasas, S., Alonso, L., Jacquet, P., Adamcik, J., Haeberli, C., and Dietler, G., *Microcontroller-driven fluid-injection system for atomic force microscopy*. Review of Scientific Instruments, 2010. **81**(1): p. 013704.
2. Kiracofe, D. and Raman, A., *On eigenmodes, stiffness, and sensitivity of atomic force microscope cantilevers in air versus liquids*. Journal of Applied Physics, 2010. **107**(3): p. 033506.
3. Binnig, G., Quate, C.F., and Gerber, C., *Atomic Force Microscope*. Physical Review Letters, 1986. **56**(9): p. 930-933.
4. Weisenhorn, A.L., Egger, M., Ohnesorge, F., Gould, S.A.C., Heyn, S.P., Hansma, H.G., Sinsheimer, R.L., Gaub, H.E., and Hansma, P.K., *Molecular-Resolution Images of Langmuir-Blodgett-Films and DNA by Atomic Force Microscopy*. Langmuir, 1991. **7**(1): p. 8-12.
5. Zhu, J., Brink, M., and McEuen, P.L., *Frequency shift imaging of quantum dots with single-electron resolution*. Applied Physics Letters, 2005. **87**(24): p. 242102.
6. Bippes, C.A., Janovjak, H., Kedrov, A., and Muller, D.J., *Digital force-feedback for protein unfolding experiments using atomic force microscopy*. Nanotechnology, 2007. **18**(4): p. 044022.
7. Oberhauser, A.F., Marszalek, P.E., Carrion-Vazquez, M., and Fernandez, J.M., *Single protein misfolding events captured by atomic force microscopy*. Nature Structural Biology, 1999. **6**(11): p. 1025-1028.
8. Yang, F., Wornyo, E., Gall, K., and King, W.P., *Nanoscale indent formation in shape memory polymers using a heated probe tip*. Nanotechnology, 2007. **18**(28): p. 285302.
9. Binnig, G., Despont, M., Drechsler, U., Haberle, W., Lutwyche, M., Vettiger, P., Mamin, H.J., Chui, B.W., and Kenny, T.W., *Ultrahigh-density atomic force microscopy data storage with erase capability*. Applied Physics Letters, 1999. **74**(9): p. 1329-1331.
10. Spinney, P.S., Collins, S.D., and Smith, R.L., *Solid-phase direct write (SPDW) of carbon via scanning force microscopy*. Nano Letters, 2007. **7**(6): p. 1512-1515.
11. Forman, J.R. and Clarke, J., *Mechanical unfolding of proteins: insights into biology, structure and folding*. Current Opinion in Structural Biology, 2007. **17**(1): p. 58-66.

12. Albrecht, C.H., Clausen-Schaumann, H., and Gaub, H.E., *Differential analysis of biomolecular rupture forces*. Journal of Physics-Condensed Matter, 2006. **18**(18): p. S581-S599.
13. Moy, V.T., Florin, E.L., and Gaub, H.E., *Adhesive Forces between Ligand and Receptor Measured by Afm*. Colloids and Surfaces a-Physicochemical and Engineering Aspects, 1994. **93**: p. 343-348.
14. Stark, R.W., Drobek, T., and Heckl, W.M., *Tapping-mode atomic force microscopy and phase-imaging in higher eigenmodes*. Applied Physics Letters, 1999. **74**(22): p. 3296-3298.
15. Best, R.B. and Clarke, J., *What can atomic force microscopy tell us about protein folding?* Chemical Communications, 2002(3): p. 183-192.
16. Alexander, S., Hellemans, L., Marti, O., Schneir, J., Elings, V., Hansma, P.K., Longmire, M., and Gurley, J., *An Atomic-Resolution Atomic-Force Microscope Implemented Using an Optical-Lever*. Journal of Applied Physics, 1989. **65**(1): p. 164-167.
17. Meyer, G. and Amer, N.M., *Novel Optical Approach to Atomic Force Microscopy*. Applied Physics Letters, 1988. **53**(12): p. 1045-1047.
18. Sarid, D., *Scanning Force Microscopy with Applicaitons to Electric, Magnetic and Atomic Forces* 1994: Oxford: Oxford University Press.
19. Hu, Z.Y., Seeley, T., Kossek, S., and Thundat, T., *Calibration of optical cantilever deflection readers*. Review of Scientific Instruments, 2004. **75**(2): p. 400-404.
20. Lievonen, J., Ranttila, K., and Ahlskog, M., *Environmental chamber for an atomic force microscope*. Review of Scientific Instruments, 2007. **78**(4): p. 043703.
21. Rabe, U., Hirsekorn, S., Reinstadtler, M., Sulzbach, T., Lehrer, C., and Arnold, W., *Influence of the cantilever holder on the vibrations of AFM cantilevers*. Nanotechnology, 2007. **18**(4): p. 044008.
22. Lapshin, R.V., *Automatic drift elimination in probe microscope images based on techniques of counter-scanning and topography feature recognition*. Measurement Science & Technology, 2007. **18**(3): p. 907-927.
23. Janovjak, H., Struckmeier, J., and Muller, D.J., *Hydrodynamic effects in fast AFM single-molecule force measurements*. European Biophysics Journal with Biophysics Letters, 2005. **34**(1): p. 91-96.
24. Schaffer, T.E., *Calculation of thermal noise in an atomic force microscope with a finite optical spot size*. Nanotechnology, 2005. **16**(6): p. 664-670.
25. Gittes, F. and Schmidt, C.F., *Thermal noise limitations on micromechanical experiments*. European Biophysics Journal with Biophysics Letters, 1998. **27**(1): p. 75-81.
26. Johnson, A.S., Nehl, C.L., Mason, M.G., and Hafner, J.H., *Fluid electric force microscopy for charge density mapping in biological systems*. Langmuir, 2003. **19**(24): p. 10007-10010.
27. Haugstad, G. and Gladfelter, W.L., *Force-Displacement Measurements in a Beam-Reflection Scanning Force Microscope - Calibration Issues*. Ultramicroscopy, 1994. **54**(1): p. 31-40.

28. Fukuma, T. and Jarvis, S.P., *Development of liquid-environment frequency modulation atomic force microscope with low noise deflection sensor for cantilevers of various dimensions*. Review of Scientific Instruments, 2006. **77**(4): p. 043701.
29. Tocha, E., Song, J., Schonherr, H., and Vancso, G.J., *Calibration of friction force signals in atomic force microscopy in liquid media*. Langmuir, 2007. **23**(13): p. 7078-7082.
30. Schaffer, T.E. and Hansma, P.K., *Characterization and optimization of the detection sensitivity of an atomic force microscope for small cantilevers*. Journal of Applied Physics, 1998. **84**(9): p. 4661-4666.
31. Proksch, R., Schaffer, T.E., Cleveland, J.P., Callahan, R.C., and Viani, M.B., *Finite optical spot size and position corrections in thermal spring constant calibration*. Nanotechnology, 2004. **15**(9): p. 1344-1350.
32. Stark, R.W., *Optical lever detection in higher eigenmode dynamic atomic force microscopy*. Review of Scientific Instruments, 2004. **75**(11): p. 5053-5055.
33. Yariv, A., *Quantum Electronics 3rd edn*. 1989: New York: Wiley.
34. Hecht, E., *Optics 4th edn*. 2002: Reading, MA: Addison Wesley Longman.
35. Putman, C.A.J., Degrooth, B.G., Vanhulst, N.F., and Greve, J., *A Detailed Analysis of the Optical Beam Deflection Technique for Use in Atomic Force Microscopy*. Journal of Applied Physics, 1992. **72**(1): p. 6-12.
36. Heim, L.O., Kappl, M., and Butt, H.J., *Tilt of atomic force microscope cantilevers: Effect on spring constant and adhesion measurements*. Langmuir, 2004. **20**(7): p. 2760-2764.
37. McKendry, R., Zhang, J.Y., Arntz, Y., Strunz, T., Hegner, M., Lang, H.P., Baller, M.K., Certa, U., Meyer, E., Guntherodt, H.J., and Gerber, C., *Multiple label-free biodetection and quantitative DNA-binding assays on a nanomechanical cantilever array*. Proceedings of the National Academy of Sciences of the United States of America, 2002. **99**(15): p. 9783-9788.
38. Zhang, R., Best, A., Berger, R., Cherian, S., Lorenzoni, S., Macis, E., Raiteri, R., and Cain, R., *Multiwell micromechanical cantilever array reader for biotechnology*. Review of Scientific Instruments, 2007. **78**(8): p. 084103.
39. Kasas, S., Wang, X., Hirling, H., Catsicas, S., Haeberli, C., Dietler, G., and Thomson, N., *Setup for observing living cells using a commercial atomic force microscope*. Review of Scientific Instruments, 2000. **71**(11): p. 4338-4340.
40. Kim, Y., Kang, S.K., Choi, I., Lee, J., and Yi, J., *Dependence of image distortion in a liquid-cell atomic force microscope on fluidic properties*. Applied Physics Letters, 2006. **88**(17): p. 173121.

CHAPTER 3
DETECTION SENSITIVITY OF DYNAMIC FLEXURAL AFM MODE*

The mechanism of dynamic force modes has been successfully applied to many atomic force microscopy (AFM) applications such as tapping mode. The higher-order flexural vibration modes are recent advance of AFM dynamic force modes. Furthermore, the calibration of the AFM cantilever spring constant can be implemented by Lorentzian fitting the peak of the thermal spectrum of the dynamic cantilever beam at its fundamental resonance (tapping resonance). Therefore, AFM optical lever detection sensitivity plays a major role in dynamic modes because it determines the accuracy in mapping surface morphology, distinguishing various tip-surface interactions, measuring the strength of the tip-surface interactions, and calibrating spring constant. In this chapter, we will analyze optimization and calibration of the optical lever detection sensitivity for an AFM cantilever-tip ensemble vibrating in flexural modes and/or simultaneously experiencing a wide range and variety of tip-sample interactions.

3.1 INTRODUCTION

The amplitude-modulated dynamic force modes in the operation of atomic force microscopy (AFM) commonly include the tapping mode, its secondary imaging mode, and the phase imaging mode. These modes of AFM have been widely applied to materials science and biological science, due to their ability to probe not only the surface morphology but also the mechanical and chemical properties of materials with high spatial resolution [1, 2]. In tapping mode, the cantilever/tip ensemble is excited at or close to its fundamental resonance frequency and the tip intermittently taps the sample surface with minimized destructive lateral forces[3]. While the oscillating tip approaches to or retracts from the sample surface under tapping amplitude modulation, it experiences

* Modified versions of this part have been published as: Liu, Y., Guo, Q.Q., Nie, H.Y., Lau, W.M., and Yang, J. Journal of Applied Physics. 106, 2009, 124507; Naeem, S., Liu, Y., Nie, H.Y., Lau, W.M., and Yang, J., Journal of Applied Physics, 104, 2008, 114504.

a complex and time-varying force field which contains a wealth of information about the materials composition [4], electrical [5] and mechanical properties[6], as well as dissipative response of the sample [7, 8]. As a result, such tip-sample interactions generate a disturbance to the vibration of the cantilever while it is tapping at the resonance frequency. Thus the motion of cantilever becomes anharmonic. In addition, the effect of the tip-sample interactions often excites higher-order flexural oscillation modes of the AFM cantilever [9, 10]. Studies of these higher-order oscillations are scientifically interesting and technologically important.

Higher-order dynamic flexural modes are recent advance of AFM dynamic force microscopy, which further enhance AFM functionality in analyzing tip-sample interactions, surface composition and material properties, as shown in Figure 1.20. Recently, researchers have investigated the possibility of using higher-order flexural modes to explain the origins of the anharmonic spectra, and therefore extract the information of the tip-sample interactions. Such information can not be obtained by the traditional dynamic analysis of tapping mode that is based on the fundamental resonance. Several recent studies of higher-order dynamic force modes are highlighted as follows. Minne et al. [11] studied the second flexural mode to monitor the change of ZnO film admittance, which is not possible to probe while the AFM is operated at the fundamental resonance. Hoummady and Farnault [12] applied the second-order flexural mode to distinguish hydrodynamic damping and attractive interaction. They found that the AFM optical lever detection sensitivity was enhanced in the second-order flexural mode. Stark et al. [9, 13-15] studied the origins of the increased anharmonic responses in higher-order flexural modes due to nonlinear tip-sample interactions. They also resolved the force constants of the tip-sample interactions by analyzing a wide spectrum of flexural motions of the cantilever using Fourier transformation. By simulating the AFM cantilever using finite element method, Song and Bhushan [10] studied the dynamic responses of the cantilever under both of attractive and repulsive force regimes, and concluded that the nonlinear force field excited higher-order modes of the vertical bending. García's group [16-18] developed an approach to probe materials' properties by simultaneously exciting the first two flexural modes. The second-order flexural mode, generally a nonharmonic

eigenmode of the cantilever [19], is less coupled with the first-order mode according to the amplitude of vibration [16]. In their work, sample topography and composition contrast were obtained simultaneously through locking-in signals of the first two flexural modes respectively. As a result, the sensitivity detected in the second-order flexural mode for compositional mapping was promoted by a factor of 10 because of a higher Q-factor. However, higher flexural mode vibration requires much higher driving force and the effective signal-to-noise ratio becomes lower. Worse case is that higher flexural vibration may cause fatigue problem of the cantilever. Therefore, further attempts have been made by Sahin et al. [20] to enable a specially-designed (notched) cantilever to reach the high-order harmonics of its higher-order flexural modes. This consequently enables sensing the non-linear mechanical interactions due to higher signal-to-noise ratio [21].

In the study of the dynamics of AFM, the optical lever detection sensitivity, which is defined as the converting relationship between the measured AFM photodetector voltage and the cantilever deflection, plays a crucial role in determining the detectable minimum change of the vibrating amplitude. Since the minimum detectable force constant is proportional to the minimum detectable amplitude change [22], higher detection sensitivity is related to a better ability to detect a small force constant applied to the cantilever. In the literature, studying and optimizing the optical lever detection sensitivity is an important issue not only for the design [23] but also for operation of AFM systems such as for more accurate detection of tip-sample interactions [24, 25]. Traditionally, the calibration of the detection sensitivity, σ_{end} , of an optical lever AFM is done by measuring force curves on a hard substrate in the contact mode [26]. The resultant detection sensitivity establishes a proportional relationship between the photodetector voltage output and the PZT displacement which is considered equal to the cantilever displacement deflection. However, researchers generally do not directly measure the displacement deflection of the cantilever [23, 25, 26]. Butt and Jaschke [27] recognized that the cantilever deflection as measured by the scheme of optical lever detection was indeed the angular deflection of the cantilever, which is different from the actual displacement deflection of the cantilever as measured by an interferometer [26, 28]. The angular change is dependent on the flexural modes of the cantilever. As a result, the F-D

curve method in the contact mode, based on the condition of static end-loading, is not the best way to calibrate the detection sensitivity on a vibrating cantilever beam [27, 29]. In fact, Walters et al. [30] pointed out that the optical lever detection sensitivity in the first-order flexural mode should appear as a correction of σ_{FD} by a factor of 1.09 for a rectangular cantilever beam.

Furthermore, an infinitely small laser spot located at the tip end of the cantilever was assumed in previous studies [25]. Recently, researchers [24, 25, 29, 31] and the Chapter 2 have studied the effect of the size and the location of the laser spot that is focused on the cantilever backside, on the optical lever detection sensitivity in various cases. Our objective in this work is to discuss the theoretical optimum of the optical lever detection sensitivity in both of tapping and higher-order flexural vibration modes in common experimental conditions where a wide range of the force constant of tip-sample interactions may occur and therefore constrain the optimal operating condition of AFM systems. A useful calibration method will be demonstrated to correlate the sensitivity of tapping or a high-order flexural vibration mode with the traditional σ_{FD} when appropriate corrections apply. At the end, we will discuss the amplitude sensitivity, which is obtained through monitoring the tapping amplitude attenuation relative to the tip–sample distance. The amplitude sensitivity represents another option to more accurately calibrate the detection sensitivity in dynamic modes. It has been demonstrated in our new calibration of spring constant of the cantilever based on thermal tune method [32].

3.2 THEORY

3.2.1 Flexural Modes of a Cantilever Beam Experiencing a Force Constant

A rectangular AFM cantilever beam can be modeled as a one-dimensional straight flexible beam made of homogeneous material and with a uniform cross-section. With one end clamped at its base, the flexural dynamics of a rectangular cantilever beam is given by [26, 33, 34]

$$EI\frac{\partial^4 z(x,t)}{\partial x^4}+\rho A\frac{\partial^2 z(x,t)}{\partial t^2}=0 \tag{3.1}$$

with the normalized coordinate $x\in[0,1]$ and time *t*. In Equation (3.1), *E* is the Young's modulus, ρ is the mass density, *A* is the cross section area, *I* is the area moment of inertia of the cantilever, and $z(x,t)$ is the deflection of the cantilever as a function of position and time. For a freely vibrating cantilever, in its steady–state solution, the deflection and the slope have to vanish at the clamped end $x=0$, and no moment and shear force can be present at the free end $x=1$. The corresponding boundary conditions are:

$$z(x)=0,\ \frac{\partial z(x)}{\partial x}=0 \quad \text{for} \quad x=0 \tag{3.2}$$

and

$$\frac{\partial^2 z(x)}{\partial x^2}=0,\ \frac{\partial^3 z(x)}{\partial x^3}=0 \quad \text{for} \quad x=1 \tag{3.3}$$

The normalized shape function $h_n(x)$ of free, undamped, transverse vibrations of a rectangular cantilever can be obtained as [35]:

$$h_n(x)=\frac{(-1)^n}{2}\left[(\cos\kappa_n x-\cosh\kappa_n x)-\frac{(\cos\kappa_n+\cosh\kappa_n)}{(\sin\kappa_n+\sinh\kappa_n)}(\sin\kappa_n x-\sinh\kappa_n x)\right] \tag{3.4}$$

where *n* denotes the order of the flexural mode and κ_n is the dimensionless wave numbers which are determined by the characteristic equation:

$$\cos\kappa_n\cosh\kappa_n+1=0 \tag{3.5}$$

If a static force acts on the tip (pinned end), the Equation (1.1) should be applied for a statically curved cantilever. The normalized shape function $h_{end}(x)$ is given by

$$h_{end}(x)=\frac{3x^2-x^3}{2} \tag{3.6}$$

This is generally applicable for force curve or contact mode operation for calibration of σ_{FD} when assuming the end-displacement of the cantilever as detected by photodetector.

In the tapping mode, when the cantilever is engaged close to the sample surface by a

separation distance *d*, it experiences nonlinear tip-sample interactions. However, if the cantilever vibrates with a very small amplitude around its equilibrium position d_0, the tip-sample force could be linearized as a spring with a force constant $k_{eff} = -\left.\frac{\partial F}{\partial d}\right|_{d=d_0}$ [36, 37]. In this study, k_{eff} is the derivative of all tip-sample interaction forces, *F*, with respect to the separation distance *d*. Consequently, a force $k_{eff} z$ due to the deflection z should be added to the shear force [36]:

$$EI\frac{\partial^3 z}{\partial x^3} - k_{eff} z = 0 \tag{3.7}$$

with the following boundary conditions:

$$h_n(x) = 0 \quad \text{and} \quad \frac{\partial h_n(x)}{\partial x} = 0 \qquad \text{at} \quad x = 0 \tag{3.8}$$

$$\frac{\partial^2 h_n(x)}{\partial x^2} = 0 \quad \text{and} \quad \frac{\partial^3 h_n(x)}{\partial x^3} = \frac{k_{eff}}{EI} h_n(x) = \frac{3k_{eff}}{k_C} h_n(x) \qquad \text{at} \quad x = 1 \tag{3.9}$$

where k_C denotes the cantilever spring constant. To solve the characteristic equation for this system, the same procedure described in our previous study is used to obtain,

$$\sinh\kappa_n \cos\kappa_n - \sin\kappa_n \cosh\kappa_n = \frac{(\kappa_n)^3 k_c}{3k_{eff}}\left(1 + \cos\kappa_n \cosh\kappa_n\right) \tag{3.10}$$

If $k_{eff} = 0$, Equation (3.10) reduces to Equation (3.5), which describes a freely vibrating cantilever. In the other extreme case when $k_{eff} = \infty$, the cantilever is pinned at both ends: base and tip. The dimensionless wave number κ_n is affected by the value of k_{eff} relative to the cantilever spring constant k_C. In this study, we only show the results for *n* up to 4 because we have found that the maximum detection sensitivity is nearly independent on the force constant if $n \geq 4$.

3.2.2 Optical Lever Detection Sensitivity

Previous studies have provided the expression of the optical lever detection sensitivity based on the classical diffraction theory [25, 33, 38, 39]. In this work, one-dimensional irradiation distribution of a Gaussian optical beam is assumed to perpendicularly impinge

and be focused on the backside of the cantilever [25, 39]. In addition, the effects of the torsion of the cantilever [10, 36] and the interference from the sample are ignored in this work. Therefore, we have

$$I(x) = \sqrt{\frac{8}{\pi}} \frac{P_0}{w_0} \exp\left(\frac{-8(x-\gamma)^2}{\left(w_0 / L \right)^2} \right) \tag{3.11}$$

where P_0 is the total power of the laser beam, w_0 is the diameter of the Gaussian laser focused along the *x*-axis (longitudinal axis of the cantilever), *L* is the cantilever length, and γ is the relative location of the laser beam centered on the cantilever which is defined to be 0 at the base and 1 at the tip end [33]. As a result, the scalar wave function is

$$E(x) = \sqrt{\sqrt{\frac{8}{\pi}} \frac{P_0}{w_0}} \exp\left(\frac{-4(x-\gamma)^2}{\left(w_0 / L \right)^2} \right) \tag{3.12}$$

The optical lever detection sensitivity at the *n*-th order flexural mode is given as [25, 37]

$$\sigma_n\left(\frac{w_0}{L}, \gamma \right) = \frac{4\alpha}{\lambda} \int_0^1 dx \int_0^1 dx' \, E(x) E(x') \frac{h_n(x) - h_n(x')}{x - x'} \tag{3.13}$$

where α denotes the loss factor when laser transmits from the laser source to the photo detector, λ is the laser wavelength. In the present work, we also assume no power loss ($\alpha = 1$) [33]. For static end – loading, $h_{end}(x)$ should be used in Equation (3.13) and the corresponding detection sensitivity is $\sigma_{end}\left(\frac{w_0}{L}, \gamma \right)$.

An "effective slope" of the section of the cantilever shined by the focused laser spot is given by:

$$c_n(\tau, \gamma) = \frac{4}{\pi \tau^2} \int_0^1 dx \int_0^1 dx' \, E(x) E(x') \frac{h_n(x) - h_n(x')}{x - x'} \exp\left[\frac{-4(x-\gamma)^2 - 4(x'-\gamma)^2}{\tau^2} \right] \tag{3.14}$$

where $\tau = \frac{w_0}{L}$ is the normalized spot size relative to the cantilever length. In optical

lever deflection AFM, $c_n(\tau,\gamma)$ is detected by the photodetector.

3.3 RESULTS AND DISCUSSIONS

The absolute value of the optical lever detection sensitivity is proportional to the "effective slope" $|c_n|$ by a constant. Thus we term $|c_n|$ as the equivalent detection sensitivity in our discussion [24]. It is a function of both the normalized spot size τ and the normalized location γ. The values of $|c_n|$ for different ratios of k_{eff}/k_C are displayed as contour plots in Figure 3.1, and Figures 3.2 – 3.4 for the flexural modes at *n* = 1, 2, 3 and 4, respectively. The maximum on the contour plot is defined to be the "globally optimized detection sensitivity" $|c_{global}|$ of the optical lever AFM. When there are several local maxima on the contour plots, among them the local maximum closest to the cantilever tip end is defined to be the "tip optimized detection sensitivity" $|c_{tip}|$ [24].

3.3.1 Effect of Tip – Sample Interaction on Tapping Sensitivity

From Table 3.1, for the first flexural mode (*n* = 1) or tapping mode, the globally optimized detection sensitivity $|c_{global}|$ coincides with the tip optimized detection sensitivity $|c_{tip}|$ at $\tau \cong 0.95$ and $\gamma \cong 0.57$ when $k_{eff}/k_C < 1$ as shown in Figure 3.1(a). When the laser spot diameter is about 95% of the cantilever length and the spot center is located at about 57% away from the cantilever base, the optimum detection sensitivity for the first flexural mode of the optical lever AFM system can be attained [24]. According to our study here, this conclusion should be constrained with another condition that k_{eff}/k_C may not significantly exceed 1. However, as shown in previous theoretical and experimental studies, a much higher k_{eff}/k_C is realistic and can go up to 200 or more [36, 40, 41]. Then the question remains: what if $k_{eff}/k_C >> 1$. We find, when k_{eff}/k_C significantly exceeds 1, the conditions for the globally optimized detection sensitivity may change. For example, when $k_{eff}/k_C = 10$ in Table 3.1, the normalized spot size decreases to $\tau \cong 0.88$ and the normalized spot location shifts to $\gamma \cong 0.43$. This

can be explained from Figure 3.1(c) which describes the normalized spot locations where the absolute values of $h'(\gamma)$, the derivative of the shape function, are "global maximum" (black solid line) and "tip maximum" (black dash line) for different values of k_{eff}/k_C . As mentioned before, the optical lever AFM systems detect the slope of the cantilever rather than its displacement deflection. From Figure 3.1(c), the normalized spot location γ of the global maximum $|h'(\gamma)|$ ($Max|h'(\gamma)|$) is shifted from the tip end to the cantilever base when k_{eff}/k_C is small or intermediate. As a result, the location of $|c_{global}|$ is shifted.

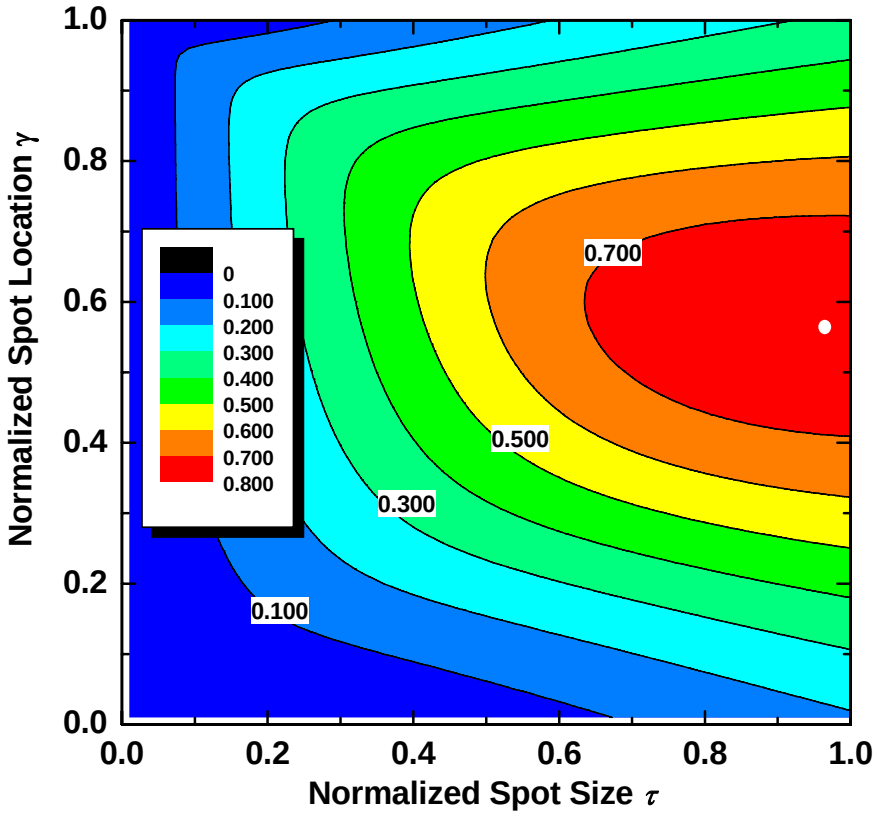

(a)

Figure 3.1 (continued)

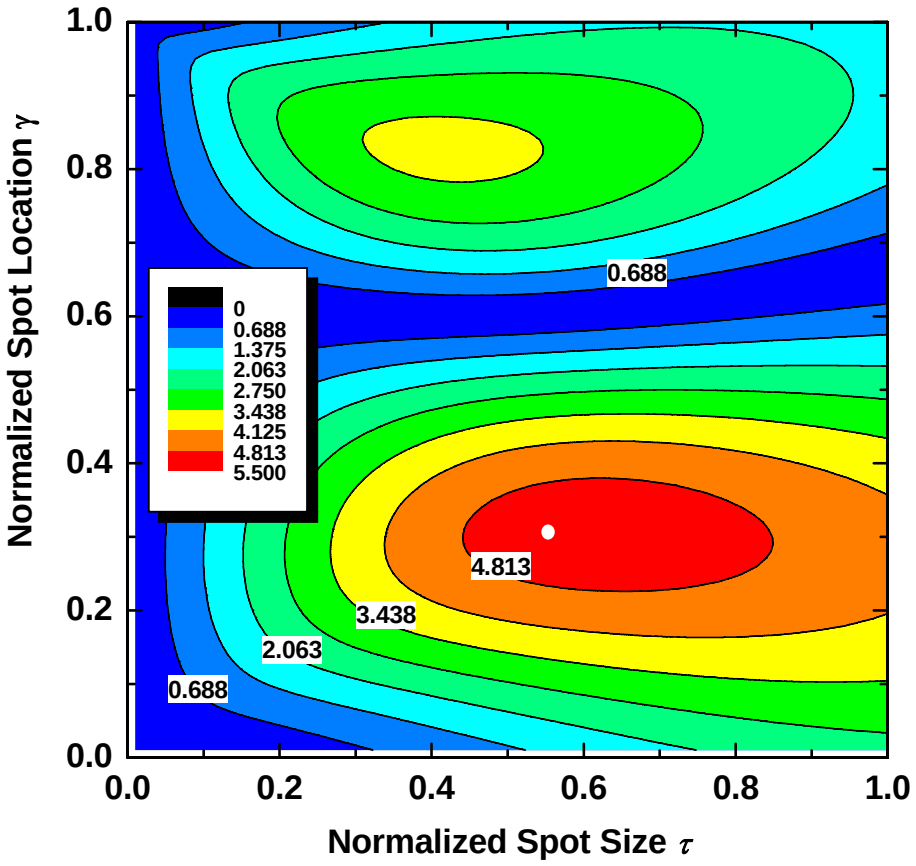

(b)

Figure 3.1 (continued)

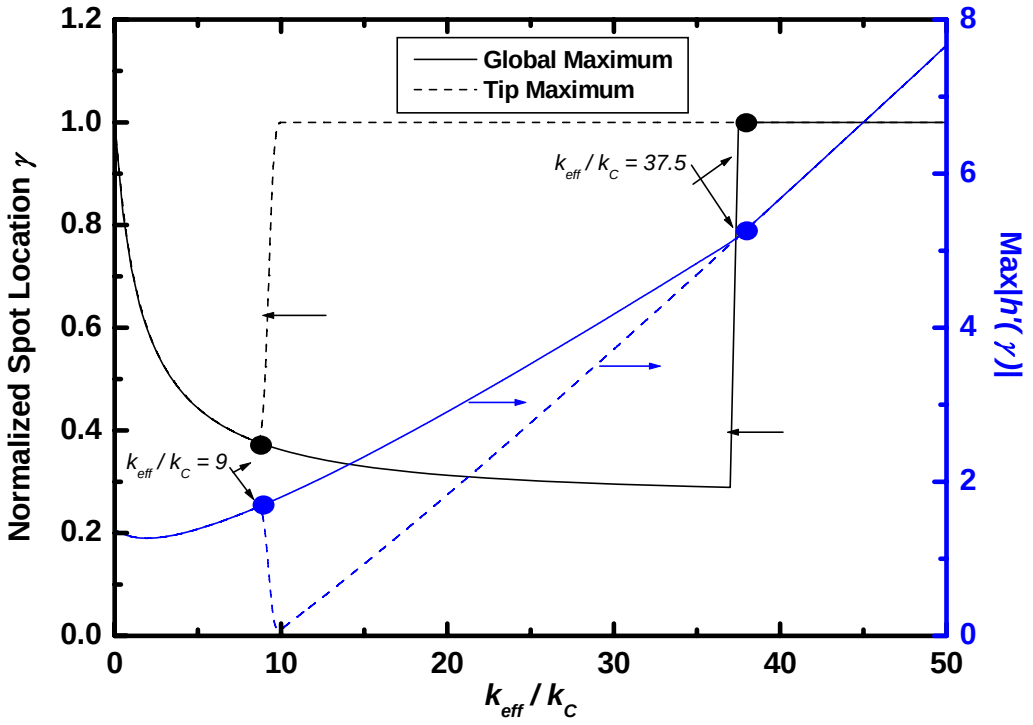

(c)

Figure 3.1 Contours of optical lever detection sensitivities in 1st-order flexural mode plotted as function of normalized spot size τ and normalized spot location γ for different ratios of the force constant to the spring constant of the cantilever: (a) $k_{eff}/k_C = 0.01$; (b) $k_{eff}/k_C = 100$. The locations of the globally optimized detection sensitivity are shown as white dots "o" on the contours. (c) the normalized spot location γ and the cantilever slope $\left|h'(\gamma)\right|$ for different k_{eff}/k_C.

If $k_{eff}/k_C >> 1$, the globally optimized detection sensitivity and the tip optimized detection sensitivity tend to separate from each other. For example, when $k_{eff}/k_C = 100$ as shown in Figure 3.1(b), for the globally optimized detection sensitivity, $\tau_{global} \cong 0.55$ and $\gamma_{global} \cong 0.31$; but for the tip optimized detection sensitivity, $\tau_{tip} \cong 0.40$ and $\gamma_{tip} \cong 0.85$. This difference can also be partially explained in light of $Max\left|h'(\gamma)\right|$ which

is directly related to the cantilever shape. When k_{eff}/k_C is relative small, the "tip maximum" and the "global maximum" for $|h'(\gamma)|$ are identical to each other at the same spot location; but when k_{eff}/k_C becomes bigger, they become different. As a result, the globally and tip optimized detection sensitivities become different as well. Figure 3.1(c) shows, according to Equation (3.4), the separation point for the global maximum $|h'(\gamma)|$ and the tip maximum $|h'(\gamma)|$ is at $k_{eff}/k_C = 9$, where it is assumed that the laser spot is zero-size point. In reality, the separation point for $|c_{global}|$ and $|c_{tip}|$ occurs at somewhere $k_{eff}/k_C > 9$, since the size of the focused laser spot is not zero. Also as shown in Figure 3.1(c), the global maximum $|h'(\gamma)|$ and the tip maximum $|h'(\gamma)|$ become identical to each other again after $k_{eff}/k_C > 37.5$. But such a crossover-point for $|c_{global}|$ and $|c_{tip}|$ has not been obtained even when we increase k_{eff}/k_C up to a reasonably big value. This aberrance between $Max|h'(\gamma)|$ and $|c_{global}|$ is because the laser spot projecting on the cantilever backside is assumed as a point laser in the calculation of $Max|h'(\gamma)|$. Thus, using $Max|h'(\gamma)|$ to predict the trend of optimized sensitivity is only valid for a certain range of the force constant k_{eff}. For higher k_{eff}/k_C, the finite size of the laser spot plays an important role in determining the optical detection sensitivity of the tapping mode AFM.

The globally optimized detection sensitivity $|c_{global}|$ for tapping mode AFM at its resonance frequency is increased with the increase of k_{eff}/k_C. When $k_{eff}/k_C = 0$, $|c_{global}| \cong 0.78$; when $k_{eff}/k_C = 100$, $|c_{global}| \cong 5.22$. The globally optimized detection sensitivity generally corresponds to the maximum value of $|h'(\gamma)|$. As shown in Figure 3.1(c), $Max|h'(\gamma)|$ (the blue solid line) monotonously increases as the increase of k_{eff}/k_C. Therefore, for a specific force constant $k_{eff} = \dfrac{\partial F}{\partial d}$ such as a single molecule

spring, using a softer cantilever with a smaller spring constant relative to the $k_{eff} = \frac{\partial F}{\partial d}$ can enhance the detection sensitivity in order to obtain more accurate force measurement, and better contrast in phase imaging as well [42]. However, with a soft cantilever, hysteresis/bistability phenomena can be easily amplified [43, 44]. In addition, the range of the "snap-to-contact" instability [45] encountered in the optical lever deflection AFM is enlarged, and the whole cantilever easily suffers from "jumping" or "snapping" [46, 47]. Therefore, there is a necessity to make a tradeoff between k_C and k_{eff} to obtain the better result in a practical application.

3.3.2 Effect of Tip – Sample Interaction on the Optical Lever Detection Sensitivity in High-order Flexural Modes

High-order flexural dynamic modes of the AFM have attracted increasing interests from AFM community [10-19, 21]. For the second-order flexural mode as shown in Figure 3.2 and Table 3.1, there are two local maxima for the cases of smaller k_{eff}/k_C and three local maxima for the case of $k_{eff}/k_C = 1000$. As k_{eff}/k_C increases, the location of the globally optimized detection sensitivity for the second-order flexural mode gradually shifts from the tip end to the base end of the cantilever, which is similar to what we have observed for the first flexural mode (tapping mode). For example, when $k_{eff}/k_C = 10$, $\gamma \cong 0.75$; and when $k_{eff}/k_C = 100$, $\gamma \cong 0.63$. For the second-order flexural mode, when $k_{eff}/k_C = 1000$, another local maximum appears close to the tip end of the cantilever, which is the tip optimized detection sensitivity. The reason is similar to what has been discussed for the case of the first-order flexural mode (tapping mode) in the previous section.

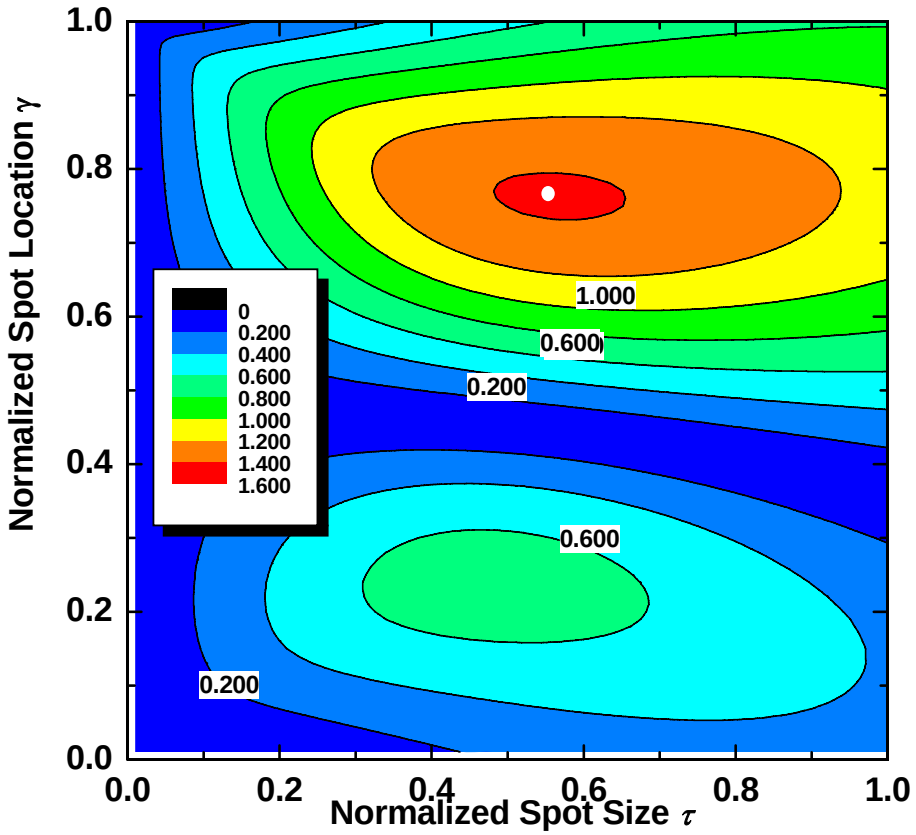

(a)

Figure 3.2 (continued)

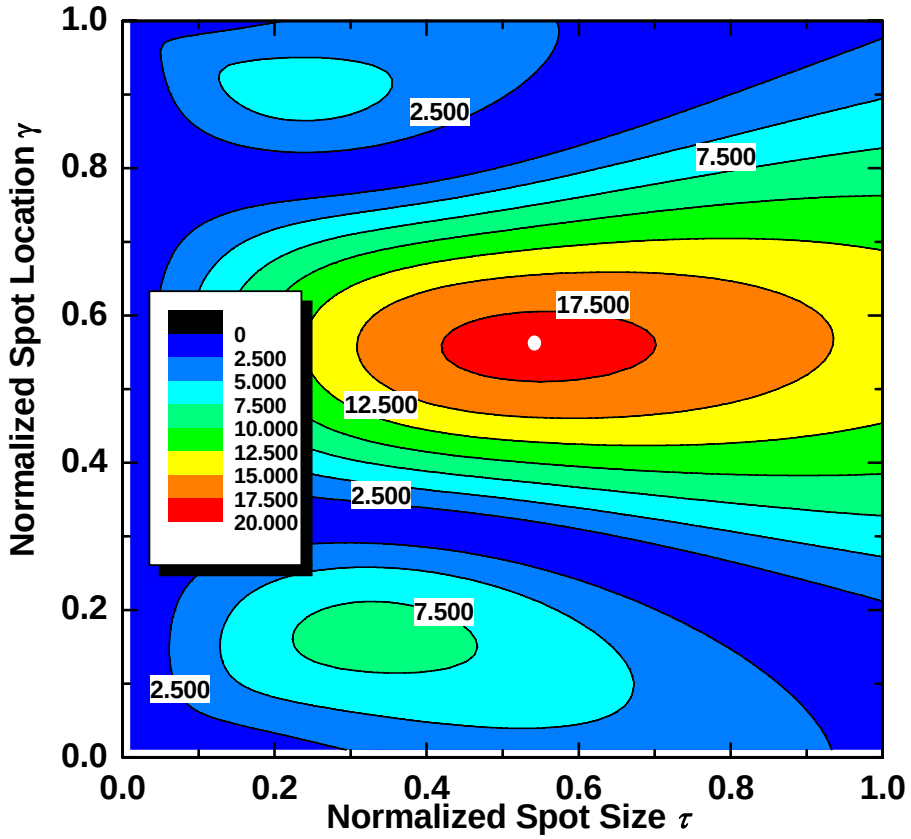

(b)

Figure 3.2 (continued)

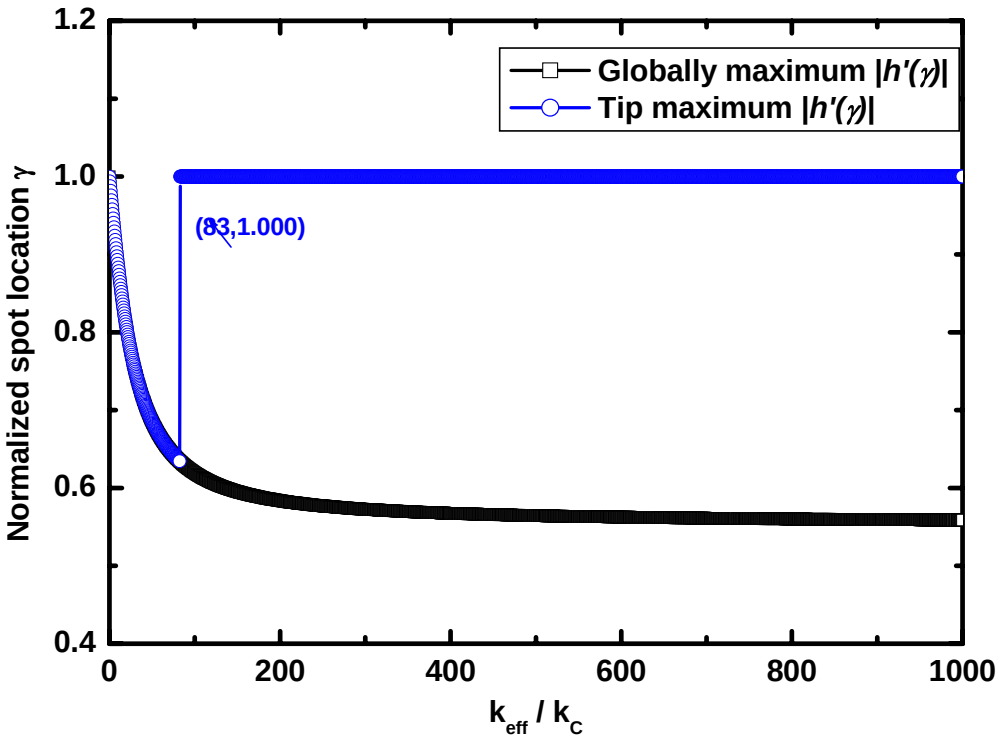

Figure 3.2(c) (continued)

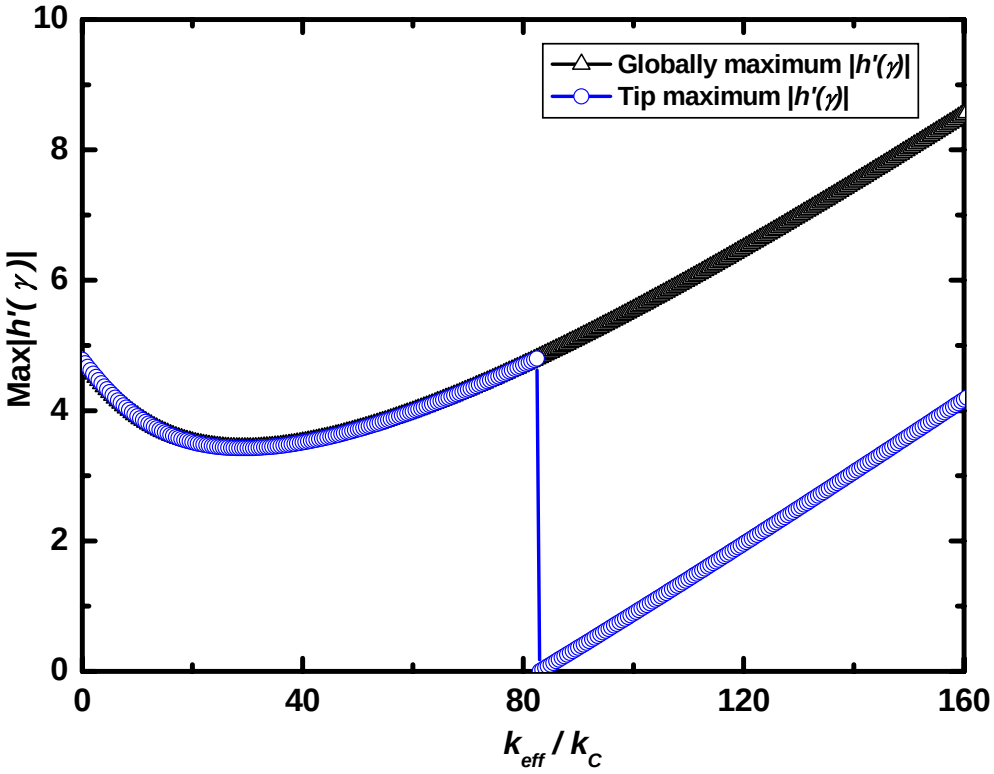

(c)

Figure 3.2 Contours of optical lever detection sensitivities in 2nd-order flexural mode plotted as function of normalized spot size τ and normalized spot location γ for different ratios of the force constant to the spring constant of the cantilever: (a) $k_{eff}/k_C = 0.01$; (b) $k_{eff}/k_C = 1000$. The locations of the globally optimized detection sensitivity are shown as white dots "o" on the contours. (c) normalized spot location γ of globally and tip maximum values of $|h'(\gamma)|$ for different k_{eff}/k_C.

An additional local maximum is also found in the third-order and fourth-order mode for large k_{eff}/k_C as shown in Figure 3.3 and Figure 3.4. Higher-order ($n > 4$) modes have also been examined, whose results are not presented here since they are similar to those of fourth-order mode. In contrast to the first and second order flexural modes, the third

and fourth-order modes always have separate globally and tip optimized detection sensitivities for any value of k_{eff}/k_C as shown in Figure 3.3(a) and Figure 3.4(a). As k_{eff}/k_C increases, both of tip and globally optimized sensitivities shift as shown in Figure 3.3(b) and Figure 3.4(b). The additional local maximum, instead of the original tip optimized sensitivity, becomes the present $|c_{tip}|$.

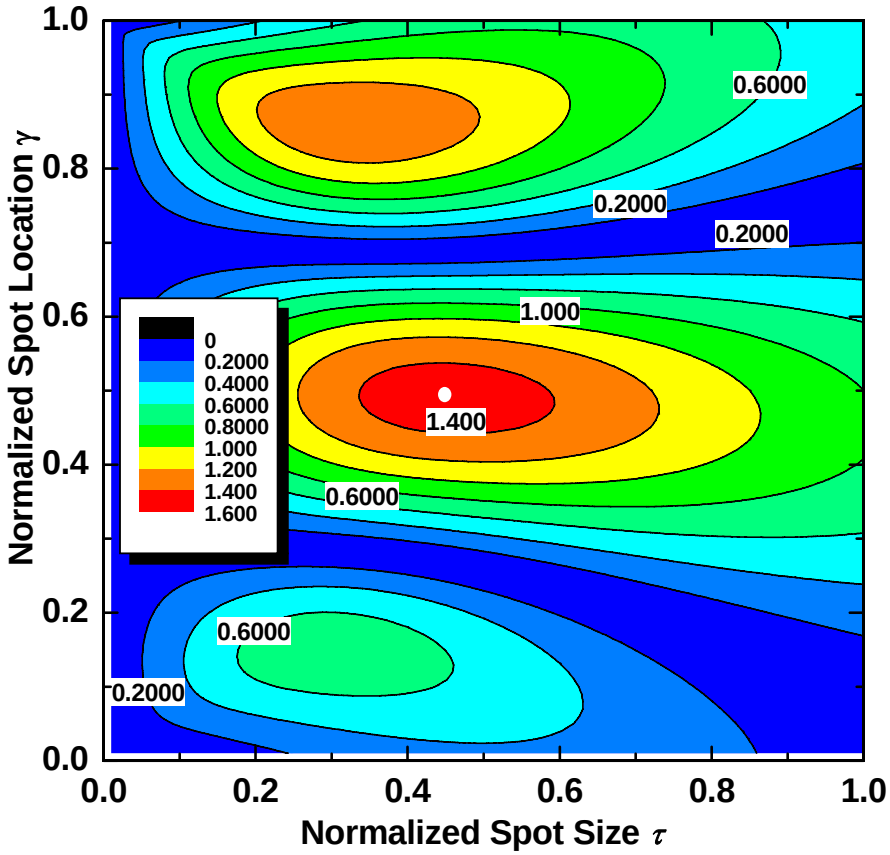

(a)

Figure 3.3 (continued)

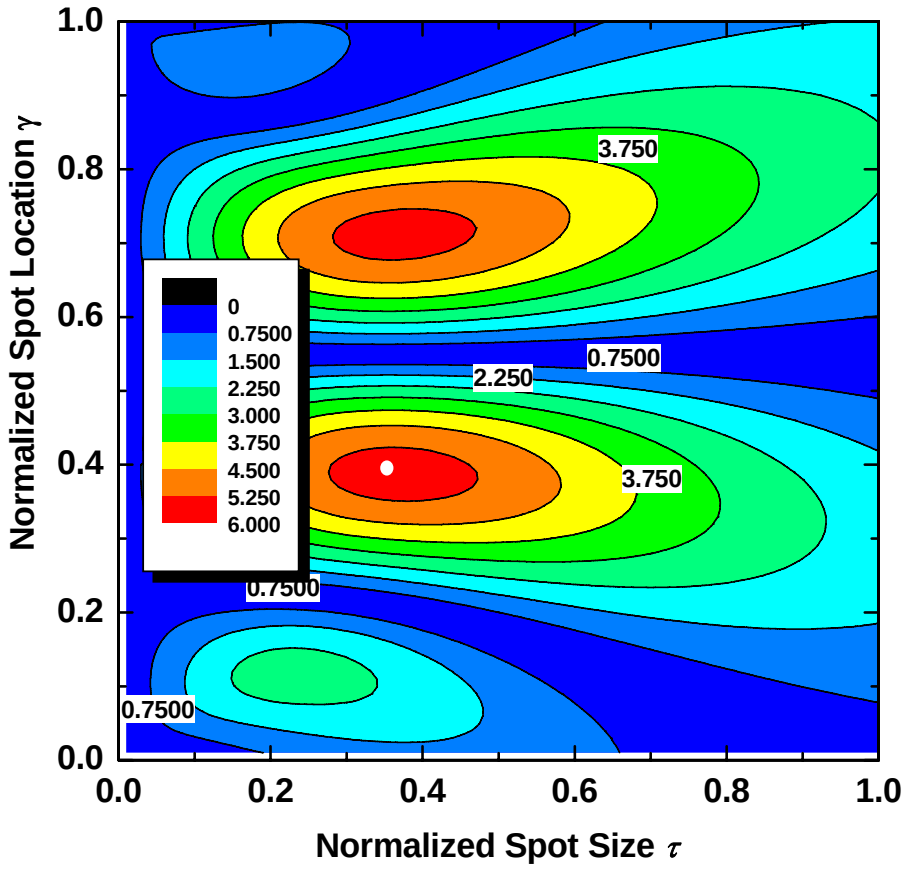

(b)

Figure 3.3 Contours of optical lever detection sensitivities in 3rd-order flexural mode plotted as function of normalized spot size τ and normalized spot location γ for different ratios of the force constant to the spring constant of the cantilever: (a) $k_{eff}/k_C = 0.01$; (b) $k_{eff}/k_C = 1000$. The locations of the globally optimized detection sensitivity are shown as white dots "o" on the contours.

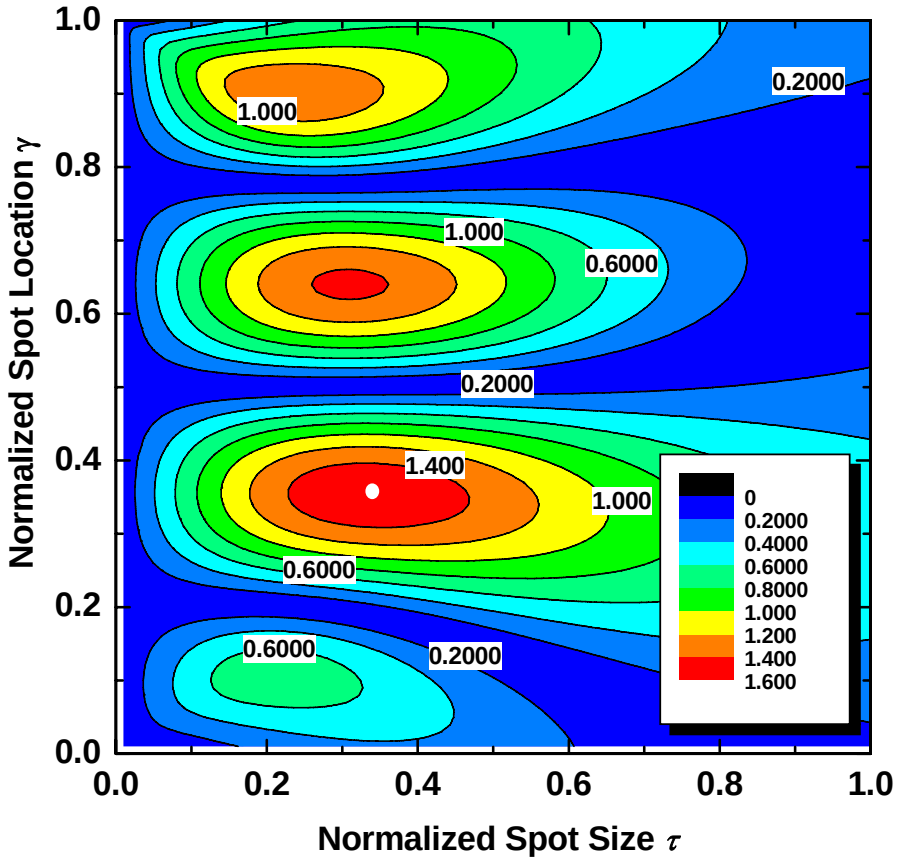

(a)

Figure 3.4 (continued)

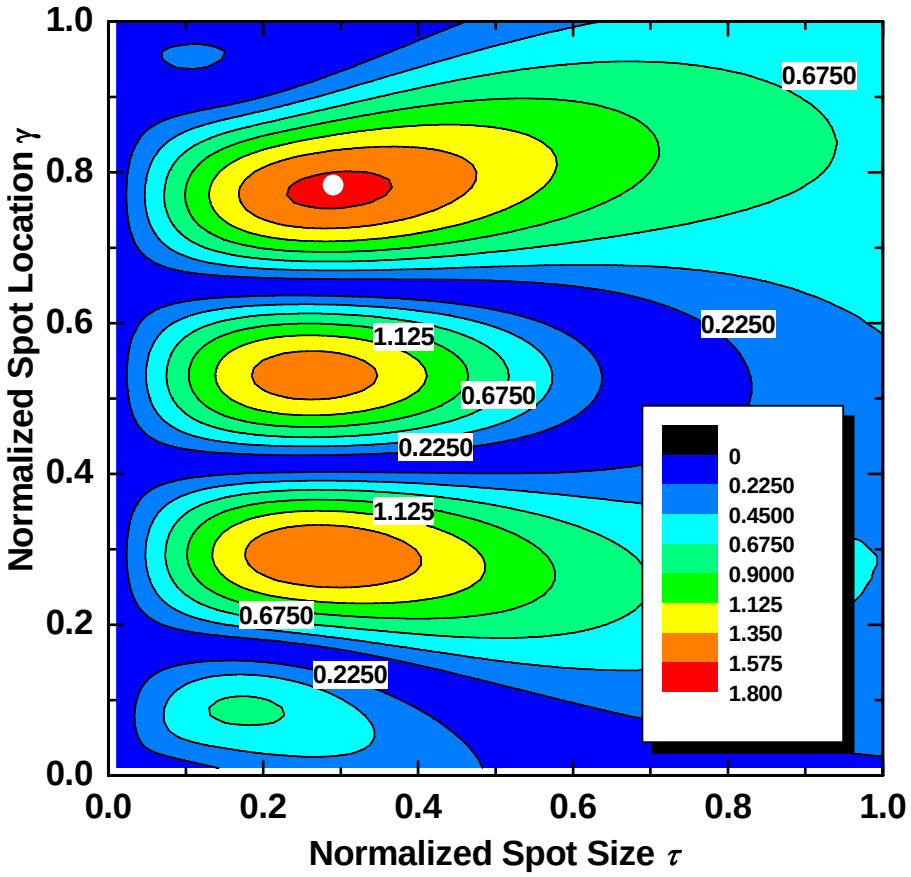

(b)

Figure 3.4 Contours of optical lever detection sensitivities in 4th-order flexural mode plotted as function of normalized spot size τ and normalized spot location γ for different ratios of the force constant to the spring constant of the cantilever: (a) $k_{eff}/k_C = 0.01$; (b) $k_{eff}/k_C = 10000$. The locations of the globally optimized detection sensitivity are shown as white dots "o" on the contours.

The values of $|c_{global}|$ and $|c_{tip}|$ in Table 3.1 show that the high-order flexural modes are less affected by the increase of k_{eff}/k_C. For example, in the first-order flexural mode

(tapping mode), the globally and tip optimized sensitivities for $k_{eff}/k_C = 100$ are about 8 and 5 times bigger than those for $k_{eff}/k_C = 0.01$, respectively. Such difference becomes much bigger for $k_{eff}/k_C = 1000$ (we extend our theoretical study to this extreme case in order to cover the full range of the force constant encountered in reality; it's worth mentioning that k_{eff}/k_C at the order of 100 is realistic). However, for the second-order flexural mode, the differences are only about 2 times even for $k_{eff}/k_C = 1000$. In high-order modes, the detection sensitivities become almost independent on k_{eff}/k_C, and only dependent on the spot size and location of the incident laser beam. This indicates that the optimized sensitivity values in high-order flexural modes become very reliable regardless of the variation of the force constant. This further leads to an important application: once the optimized sensitivity in high-order modes ($n > 3$) is calibrated, the value can be used for working on any sample with trus3 accuracy due to the reliability of the sensitivity, although the surface force field may change significantly from sample to sample. That is probably one reason why higher – order flexural mode has more reliable contrast image on material heterogeneity of surface rather than phase image of tapping mode AFM [5, 18, 19] which is easily affected by tapping conditions and surface properties.

3.3.3 Further Discussion

To require the optimization of AFM sensitivity in dynamic modes, both of spot size and spot location should be adjusted. Although previous results are only focused on rectangular cantilever, they can also be extended to triangular cantilever (not commercial available) but not for V – shaped cantilever. Especially on V – shaped cantilever, the hollow area can not allow the laser spot fully projected on the cantilever backside as well as it is impossible to position the laser spot within this area. On the other hand, in dynamic applications to resolve details of tip – sample interaction at normal direction, V – shaped cantilever is more prone to the effects of lateral forces than rectangular cantilever [48]. Therefore, rectangular cantilever is suggested to be used in applications.

Table 3.1 Normalized spot size and location of the globally optimized sensitivity and the tip optimized sensitivity as a function of k_{eff} / k_C

Mode Number	k_{eff} / k_C	Globally Optimized			Tip Optimized		
		τ_{global}	γ_{global}	$\lvert c_{global} \rvert$	τ_{tip}	γ_{tip}	$\lvert c_{tip} \rvert$
	0	**0.952**	**0.569**	**0.783**	**0.952**	**0.569**	**0.783**
	0.01	0.951	0.569	0.783	0.951	0.569	0.783
***n* =1**	0.1	0.952	0.567	0.784	0.952	0.567	0.784
	1	0.957	0.554	0.790	0.957	0.554	0.790
	10	0.881	0.430	0.939	0.881	0.430	0.939
	100	0.553	0.305	5.165	0.400	0.850	3.571
	1000	0.580	0.280	51.797	0.430	0.810	43.346
	0	**0.562**	**0.763**	**1.421**	**0.562**	**0.763**	**1.421**
	0.01	0.562	0.763	1.420	0.562	0.763	1.420
***n* =2**	0.1	0.563	0.763	1.419	0.563	0.763	1.419
	1	0.566	0.761	1.405	0.566	0.761	1.405
	10	0.595	0.745	1.317	0.595	0.745	1.317
	100	0.635	0.627	2.022	0.635	0.627	2.022
	1000	0.540	0.560	18.342	0.220	0.910	5.935
	0	**0.453**	**0.490**	**1.501**	**0.325**	**0.862**	**1.368**
	0.01	0.453	0.490	1.501	0.325	0.862	1.368
***n* =3**	0.1	0.453	0.490	1.500	0.325	0.862	1.368
	1	0.452	0.490	1.492	0.325	0.862	1.365
	10	0.449	0.486	1.413	0.331	0.859	1.340
	100	0.390	0.830	1.271	0.390	0.830	1.271
	1000	0.370	0.390	5.583	0.370	0.710	5.537
	0	**0.335**	**0.353**	**1.560**	**0.233**	**0.901**	**1.371**
	0.01	0.335	0.353	1.560	0.233	0.901	1.371
***n* =4**	0.1	0.335	0.353	1.560	0.233	0.901	1.371
	1	0.335	0.353	1.560	0.233	0.901	1.372

	10	0.334	0.352	1.560	0.234	0.900	1.383
	100	0.327	0.345	1.560	0.250	0.891	1.500
	10000	0.290	0.780	1.640	0.290	0.780	1.640
	50000	0.290	0.770	1.636	0.290	0.770	1.636

3.4 CALIBRATION OF AFM DYNAMIC SENSITIVITY

The optical lever detection sensitivity varies with many factors, such as laser alignment, cantilever backside coating, environmental medium, and optics and electronics of the AFM system. It is nearly impossible to calculate the correct detection sensitivity based on the limited information of specifications provided by manufacturers. Therefore, the detection sensitivity for an optical lever AFM is generally implemented by measuring force curves on a hard substrate, which generates an approximately linear relationship between the output voltage of the photodetector and the deflection of the cantilever with a unit of mV/nm. However, the discussion in previous sections explains the difference between dynamic sensitivity and force curve based sensitivity. We will introduce two methods for calibration of dynamic sensitivity of AFM.

In the force curve method, the deflection of the cantilever arises from a static loading at its tip end and the normalized cantilever shape function is $h_{end}(x)$. Substituting Equation (3.6) into Equation (3.13), we plot the optical lever detection sensitivity as a function of the normalized spot location and size as shown in Figure 3.5. In this method, the corresponding globally optimized sensitivity is 0.778 at $\tau \cong 0.94$ and $\gamma \cong 0.58$, which is the same as the tip optimized sensitivity. The method of static end-loading force curve has nothing to do with the force constant that however plays a major role in dynamic force modes. Herein, we established a simple calibration method to determine the optical lever detection sensitivity in high-order flexural modes with an important premise that $k_{eff} / k_C < 1$. This premise should be, and can be easily, satisfied before starting an AFM experiment through choosing an AFM cantilever with an appropriate spring constant.

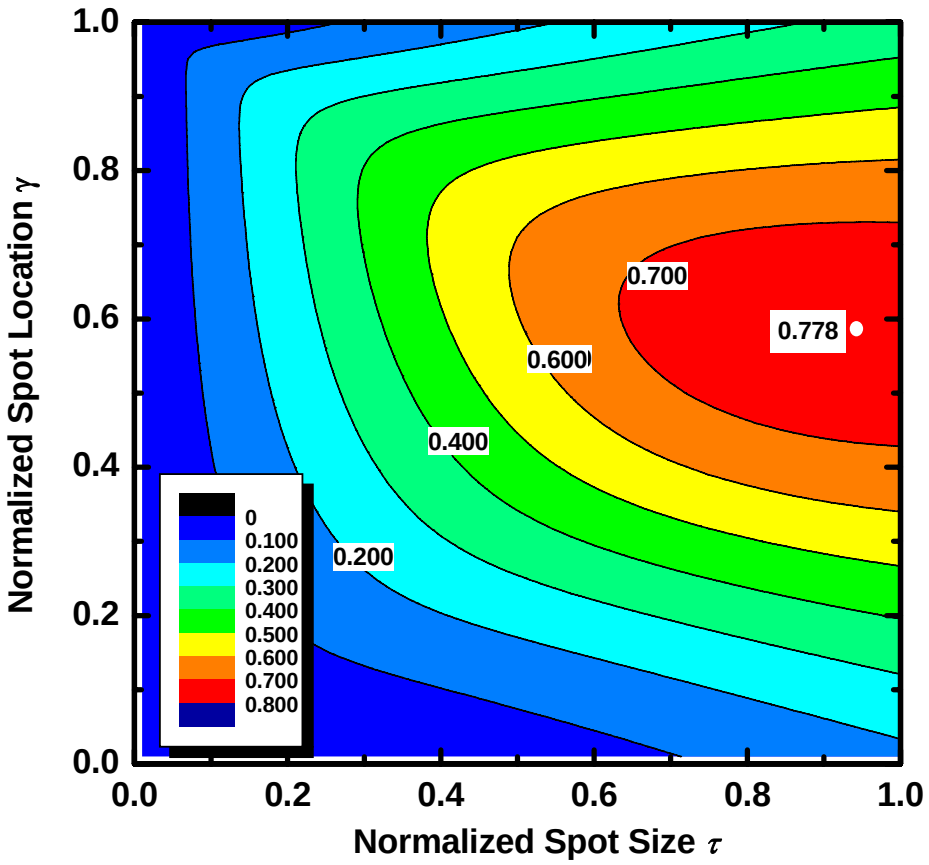

Figure 3.5 Contour of optical lever detection sensitivity of the static end-loading cantilever (force-distance curve mode) plotted as a function of the normalized spot size τ and the normalized location γ. The globally optimized and tip optimized sensitivities are identical to each other as marked by a white dot "○".

To explain the method, we are utilizing the equations (4) and (5) from the work by Schäffer and Fuchs's work [24],

$$\sigma_n(\tau,\gamma) = \sigma_0 c_n(\tau,\gamma) \tag{3.15}$$

and

$$\sigma_0 = \sqrt{\frac{\pi}{4}} \frac{4P_0\alpha(\tau,\gamma)}{\lambda} D \tag{3.16}$$

where P_0 is the laser power and D is a constant related to the title angle of the cantilever.

Considering the power loss during laser transmission, the power received by the photodetector is $P_0\alpha(\tau,\gamma)$. In practice, it is difficult to find out $\alpha(\tau,\gamma)$ due to varying experiment conditions. For operation of a well-structured AFM in air, there is less power loss related to the optical lens and transmission medium (It should be noted that for operation in liquid, the liquid medium causes more power loss [33]). Most part of $\alpha(\tau,\gamma)$ results from the misalignment of the cantilever on its holder and the non-uniformity of the cantilever backside coating. $\alpha(\tau,\gamma)$ is typically a function of the spot size and location. We need to determine both τ and γ according to the method described below.

As shown in Figure 3.6, a cantilever with a length of 230 μm was visualized under a top-view CCD camera of our AFM system Park System XE – 100. We captured the image of the whole cantilever with a laser spot on it. A good alignment in our operation ensured that the aspect ratio of the laser spot was close to 1 (i.e., a nearly circular spot). The laser spot, as shown in Figure 3.6, wholly falls on the cantilever. As a result, there is no significant light power spilled over the lateral edge of the cantilever [25]. Such a good alignment can also help eliminate the effects of the interference from the sample and the stray light. The normalized spot size and location are $\tau \cong 0.16$ and $\gamma \cong 0.59$, respectively. Correspondingly, the "effective slope" is $|c_0| \cong 0.22$. For a commercial AFM, the user has no access to adjusting the focused spot size on the cantilever. However, using a home-built tunable slit aperture [25], one can obtain $\tau \cong 0.94$. In addition, one can use a shorter cantilever in order to enlarge τ to an extent. In this study, $\tau \cong 0.16$ limits our ability to find the globally optimized detection sensitivity. Hence we can only fine tune the spot location.

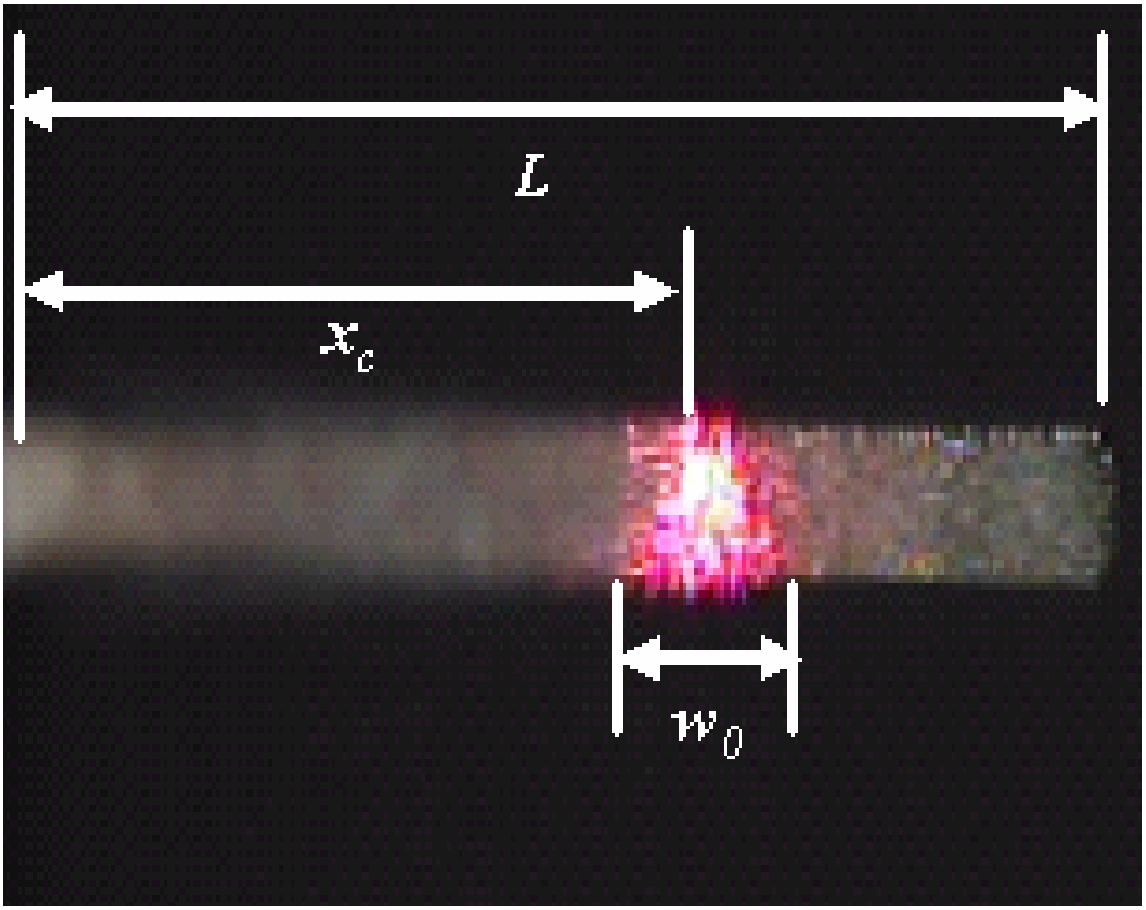

Figure 3.6 Focused laser spot on the cantilever backside with the normalized spot size τ = 0.16 and normalized spot location γ = 0.59. The length of the cantilever L is 230 μm.

Subsequently, the slope of the force curve in Figure 3.7 for this cantilever–laser spot ensemble was used to determine the sensitivity of the cantilever with static end-loading, σ_{FD}, which was equal to 41.5 mV/nm. Based on Equation (13), the corresponding σ_0 is $\frac{\sigma_{FD}}{|c_0|} \cong 188.6$ mV/nm. From Equation (3.13), we also have the value of the "effective slope" of the cantilever in high-order flexural modes when $\tau \cong 0.16$ and $\gamma \cong 0.59$: $|c_1| \cong 0.20$, $|c_2| \cong 0.30$, $|c_3| \cong 0.61$ and $|c_4| \cong 0.90$. Therefore, the detection sensitivities in the high-order flexural modes are: $\sigma_1 \cong 37.7$ mV/nm , $\sigma_2 \cong 56.6$ mV/nm ,

$\sigma_3 \cong 115.0$ mV/nm and $\sigma_4 \cong 169.7$ mV/nm, respectively. The results demonstrate that the higher order of the flexural vibration mode, the larger detection sensitivity, which is in good agreement with previous works (e.g., Refs.[12, 14, 15]). As we mentioned earlier in this article, in order to adopt this calibration method a cantilever having a spring constant larger than the force constant should be chosen for AFM experiments. This is indeed consistent with the practice for tapping mode where a stiff cantilever is preferred in order to avoid instability caused by a rather large attractive force constant during operation, which may amount to 10 N/m or more [49] for many samples.

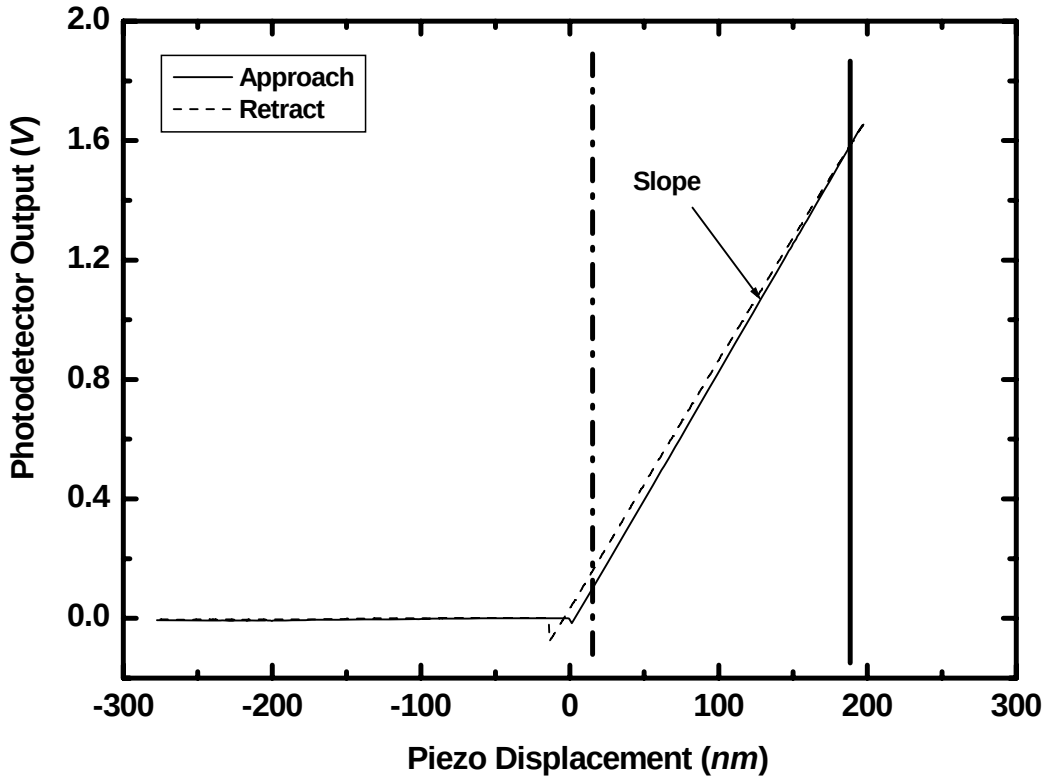

Figure 3.7 A force-distance curve obtained in contact mode AFM. The slope of the loading portion of this force-distance curve is used to determine the sensitivity of the static end-loading cantilever, which is further used to demonstrate the calibration method for detection sensitivity in the high-order flexural vibration modes.

3.5 AMPLITUDE SENSITIVITY AT TAPPING FREQUENCY

The calibration of cantilever spring constant is critically important for quantitatively determining tip – sample interaction. In the Chapter 1, we reviewed the different methods for the spring constant calibration; and thermal method [32] is one most convenient way without any damage on the cantilever during calibration process. In thermal method, high – speed data acquisition hardware is applied to sample thousands of points about the amplitudes of the dynamic cantilever beam, which is freely vibrating with thermal noise in the ambient. The set of amplitude data are converted into thermal spectrum through fast Fourier transformation. Lorentzian curve is applied to fit the peak of the thermal spectrum at the fundamental (tapping) resonance of the cantilever. Finally, the Equation (1.16) is applied to calculate the spring constant from known Boltzmann constant and measured temperature in Kelvin. We will take this section to further discuss dynamic sensitivity at tapping frequency.

As we interpreted before, the optical – lever technique is indeed working to detect the cantilever bending angle θ_{bend} rather and the cantilever deflection δ. There is clear difference between σ_{end} and dynamic sensitivity σ_1 where the subscript "1" represents first order or tapping resonance. In details, a correction factor χ is defined by:

$$\chi = \frac{\sigma_{end}}{\sigma_1} \tag{3.17}$$

As shown in Figure 3.8, the correction factor (the deviation between σ_{end} and σ_1) is dependent on k_{eff} / k_C, laser spot location and laser spot size. The figure also reveals that, for a normalized spot location x / L_{eff} around 0.6, the correction factor χ becomes 1 for all the different values of k^* / k_c.

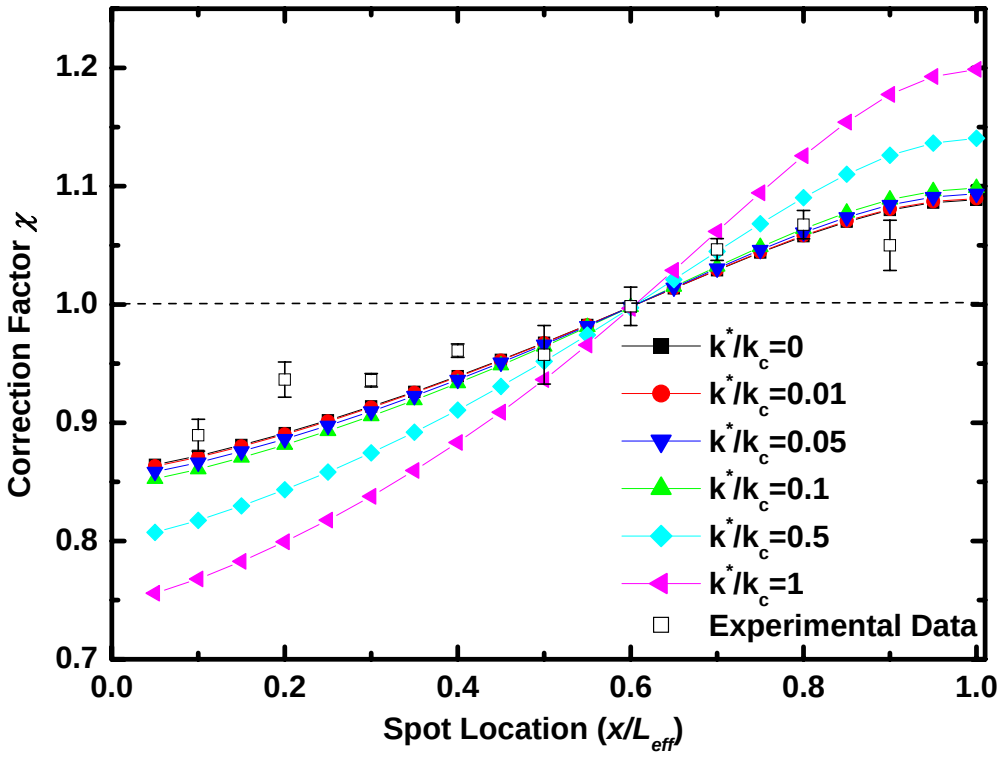

Figure 3.8 Dependence of correction factor χ on different k_{eff}/k_C and spot location for spot size $w_0/L_{eff} = 0.1$

We have already mentioned that the photodetector output is sensitive to the cantilever slope rather than its deflection. In author and his colleagues' work [29], as Figure 3.9 shows, the slopes for all the cantilevers are equal around the 0.6 normalized spot location (x/L_{eff}) so that the correction factor becomes 1. This implies the sensitivity to be same for the different cantilever end loadings at 0.6 normalized spot location (x/L_{eff}). In other words, when the spot is located close to $x/L_{eff} = 0.6$, the sensitivity σ_{end} obtained by force curve can be directly used in thermal method to calibrate the spring constant of cantilever. Otherwise, the sensitivity for thermal method should be obtained by multiplying σ_{end} by $1/\chi$. If we do not locate the spot close to 0.6, the dynamic

sensitivity at tapping frequency is varied up to 30% when k^* is increased from 0 to k_C. In other words, the sensitivity during tapping cycles is changing. However if the laser spot is located at $x / L_{eff} = 0.6$, there is no such worry.

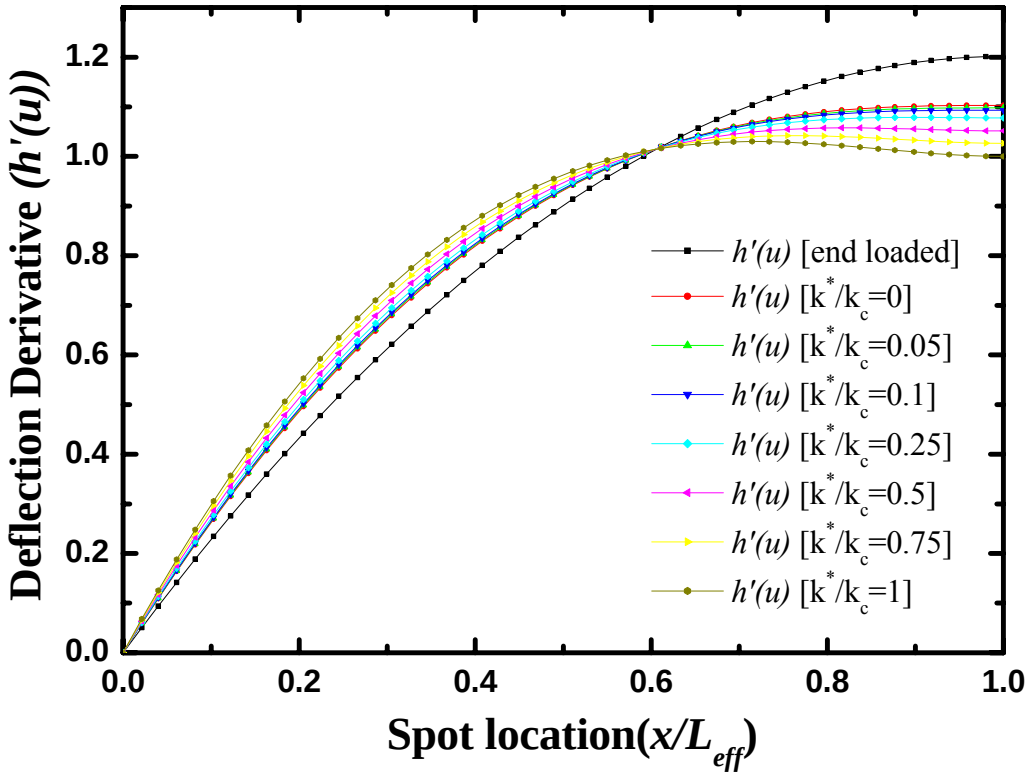

Figure 3.9 Dependence of cantilever slope on different k_{eff} / k_C and spot location

The dynamic sensitivity at tapping frequency is important for spring constant calibration. Instead of using the force curve method to obtain sensitivity, we could use monitoring the peak amplitude change of the cantilever at its tapping resonance during approaching/retracting process. Within a small approaching range, the amplitude – to – distance sensitivity which we obtain is approximating to the dynamic sensitivity in tapping AFM mode. We compared the sensitivities from the force curve and amplitude-distance methods at different spot locations (Figure 3.10), and drawn their ratio as symbolized by "□" as shown in Figure 3.8. The experimental results are falling

within the predicated ranges according to our model. Especially, at $x / L_{eff} = 0.6$ both sensitivities are same. The immunity of dynamic sensitivity to tip – sample interaction is best. Efforts in literature have been done to resolve the force constant between tip and sample based on monitoring tapping amplitude, and therefore our results in this work point out a more accurate way for this purpose. That is 0.6.

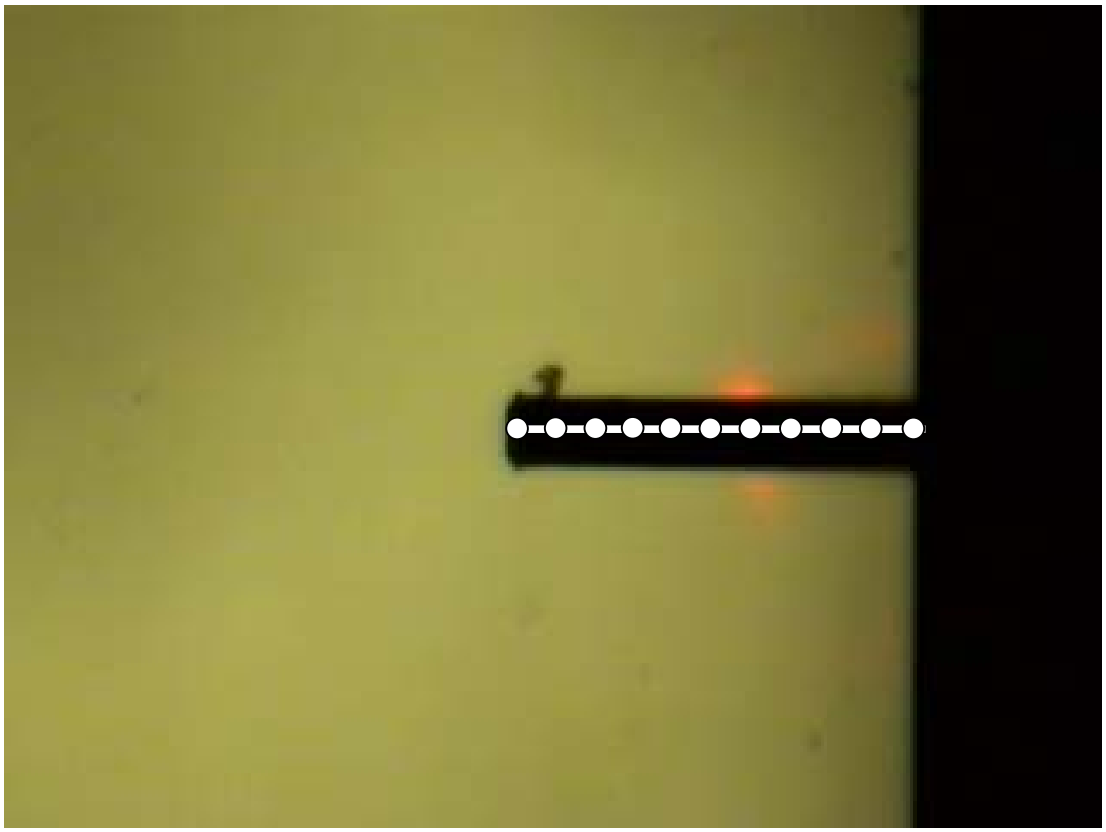

Figure 3.10 Measurement points along cantilever for sensitivities based on force curve and amplitude – distance method.

The amplitude sensitivity is an approximating alternative for dynamic sensitivity. We applied the amplitude sensitivities measured at different spot locations to calibrate the spring constant through the thermal method. The results are compared with those obtained by reference lever method [50] in Table 3.2. Amplitude sensitivity at

$x / L_{eff} = 0.6$ can provide enough accuracy to calibrate the spring constant.

Table 3.2 Calibration Results of Spring Constant by Reference Lever Method and Thermal Method with Using Amplitude Sensitivity

Reference Lever Method (N/m)	Thermal Method with using Amplitude Sensitivity (N/m)
6.47 ±0.06	6.27 ±0.19 (along whole cantilever) 7.09 ±0.18 (at $x / L_{eff} = 0.1$) 6.01 ±0.09 (at $x / L_{eff} = 0.2$) 6.74 ±0.04 (at $x / L_{eff} = 0.3$) 6.57 ±0.04 (at $x / L_{eff} = 0.4$) 6.59 ±0.16 (at $x / L_{eff} = 0.5$) 6.31 ±0.08 (at $x / L_{eff} = 0.6$) 6.03 ±0.06 (at $x / L_{eff} = 0.7$) 5.91 ±0.08 (at $x / L_{eff} = 0.8$) 6.01 ±0.13 (at $x / L_{eff} = 0.9$)

3.6 CONCLUSIONS

For dynamic force microscopy applications of an optical lever AFM system, the optimal detection sensitivity is determined in this study as a function of the order of the flexural vibration mode, the ratio of the force constant to the cantilever stiffness (k_{eff} / k_C), the laser spot size and location on the cantilever. We have tabulated a chart of the globally optimized detection sensitivity and the tip optimized detection sensitivity in the fundamental and high-order flexural modes for different k_{eff} / k_C. The optimized sensitivities in high-order flexural modes are less affected by k_{eff} / k_C. They are more stable than that of the fundamental mode (e.g., tapping mode). For k_{eff} / k_C <1, we have developed a calibration method for the detection sensitivity in high-order modes. Our results have shown that the detection sensitivity is not only more stable but also largely enhanced in high-order flexural modes. In further, we introduced a calibration method for higher – order mode AFM. At the last, we described the sensitivity at tapping frequency

and proposed that amplitude sensitivity can be adopted as a possible alternative for this tapping sensitivity. As a result, the spring constant can be successfully calibrated through thermal method.

3.7 REFERENCES

1. Zhong, Q., Inniss, D., Kjoller, K., and Elings, V.B., *Fractured Polymer Silica Fiber Surface Studied by Tapping Mode Atomic-Force Microscopy*. Surface Science, 1993. **290**(1-2): p. L688-L692.
2. Jiao, Y. and Schaffer, T.E., *Accurate height and volume measurements on soft samples with the atomic force microscope*. Langmuir, 2004. **20**(23): p. 10038-10045.
3. Burnham, N.A., Behrend, O.P., Oulevey, F., Gremaud, G., Gallo, P.J., Gourdon, D., Dupas, E., Kulik, A.J., Pollock, H.M., and Briggs, G.A.D., *How does a tip tap?* Nanotechnology, 1997. **8**(2): p. 67-75.
4. Hoper, R., Gesang, T., Possart, W., Hennemann, O.D., and Boseck, S., *Imaging Elastic Sample Properties with an Atomic-Force Microscope Operating in the Tapping Mode*. Ultramicroscopy, 1995. **60**(1): p. 17-24.
5. Bostanci, U., Abak, M.K., Aktas, O., and Dana, A., *Nanoscale charging hysteresis measurement by multifrequency electrostatic force spectroscopy*. Applied Physics Letters, 2008. **92**(9): p. 093108.
6. Tamayo, J. and Garcia, R., *Effects of elastic and inelastic interactions on phase contrast images in tapping-mode scanning force microscopy*. Applied Physics Letters, 1997. **71**(16): p. 2394-2396.
7. Cleveland, J.P., Anczykowski, B., Schmid, A.E., and Elings, V.B., *Energy dissipation in tapping-mode atomic force microscopy*. Applied Physics Letters, 1998. **72**(20): p. 2613-2615.
8. Garcia, R., Tamayo, J., and San Paulo, A., *Phase contrast and surface energy hysteresis in tapping mode scanning force microsopy*. Surface and Interface Analysis, 1999. **27**(5-6): p. 312-316.
9. Hillenbrand, R., Stark, M., and Guckenberger, R., *Higher-harmonics generation in tapping-mode atomic-force microscopy: Insights into the tip-sample interaction*. Applied Physics Letters, 2000. **76**(23): p. 3478-3480.
10. Song, Y.X. and Bhushan, B., *Simulation of dynamic modes of atomic force microscopy using a 3D finite element model*. Ultramicroscopy, 2006. **106**(8-9): p. 847-873.
11. Minne, S.C., Manalis, S.R., Atalar, A., and Quate, C.F., *Contact imaging in the atomic force microscope using a higher order flexural mode combined with a new sensor*. Applied Physics Letters, 1996. **68**(10): p. 1427-1429.
12. Hoummady, M. and Farnault, E., *Enhanced sensitivity to force gradients by using higher flexural modes of the atomic force microscope cantilever*. Applied Physics a-Materials Science & Processing, 1998. **66**: p. S361-S364.
13. Stark, R.W. and Heckl, W.M., *Higher harmonics imaging in tapping-mode*

atomic-force microscopy. Review of Scientific Instruments, 2003. **74**(12): p. 5111-5114.

14. Stark, R.W. and Heckl, W.M., *Fourier transformed atomic force microscopy: tapping mode atomic force microscopy beyond the Hookian approximation*. Surface Science, 2000. **457**(1-2): p. 219-228.
15. Stark, M., Stark, R.W., Heckl, W.M., and Guckenberger, R., *Inverting dynamic force microscopy: From signals to time-resolved interaction forces*. Proceedings of the National Academy of Sciences of the United States of America, 2002. **99**(13): p. 8473-8478.
16. Rodriguez, T.R. and Garcia, R., *Compositional mapping of surfaces in atomic force microscopy by excitation of the second normal mode of the microcantilever*. Applied Physics Letters, 2004. **84**(3): p. 449-451.
17. Martinez, N.F., Patil, S., Lozano, J.R., and Garcia, R., *Enhanced compositional sensitivity in atomic force microscopy by the excitation of the first two flexural modes*. Applied Physics Letters, 2006. **89**(15): p. 153115.
18. Lozano, J.R. and Garcia, R., *Theory of phase spectroscopy in bimodal atomic force microscopy*. Physical Review B, 2009. **79**(1): p. 014110.
19. Proksch, R., *Multifrequency, repulsive-mode amplitude-modulated atomic force microscopy*. Applied Physics Letters, 2006. **89**(11): p. 113121.
20. Sahin, O., Magonov, S., Su, C., Quate, C.F., and Solgaard, O., *An atomic force microscope tip designed to measure time-varying nanomechanical forces*. Nature Nanotechnology, 2007. **2**(8): p. 507-514.
21. Sahin, O., Yaralioglu, G., Grow, R., Zappe, S.F., Atalar, A., Quate, C., and Solgaard, O., *High-resolution imaging of elastic properties using harmonic cantilevers*. Sensors and Actuators a-Physical, 2004. **114**(2-3): p. 183-190.
22. Martin, Y., Williams, C.C., and Wickramasinghe, H.K., *Atomic Force Microscope Force Mapping and Profiling on a Sub 100-a Scale*. Journal of Applied Physics, 1987. **61**(10): p. 4723-4729.
23. Beaulieu, L.Y., Godin, M., Laroche, O., Tabard-Cossa, V., and Grutter, P., *Calibrating laser beam deflection systems for use in atomic force microscopes and cantilever sensors*. Applied Physics Letters, 2006. **88**(8): p. 082108.
24. Schaffer, T.E. and Fuchs, H., *Optimized detection of normal vibration modes of atomic force microscope cantilevers with the optical beam deflection method*. Journal of Applied Physics, 2005. **97**(8): p. 083524.
25. Schaffer, T.E. and Hansma, P.K., *Characterization and optimization of the detection sensitivity of an atomic force microscope for small cantilevers*. Journal of Applied Physics, 1998. **84**(9): p. 4661-4666.
26. Sarid, D., *Scanning Force Microscopy with Applicaitons to Electric, Magnetic and Atomic Forces* 1994: Oxford: Oxford University Press.
27. Butt, H.J. and Jaschke, M., *Calculation of Thermal Noise in Atomic-Force Microscopy*. Nanotechnology, 1995. **6**(1): p. 1-7.
28. Rugar, D., Mamin, H.J., Erlandsson, R., Stern, J.E., and Terris, B.D., *Force Microscope Using a Fiber-Optic Displacement Sensor*. Review of Scientific Instruments, 1988. **59**(11): p. 2337-2340.
29. Naeem, S., Liu, Y., Nie, H.Y., Lau, W.M., and Yang, J., *Revisiting atomic force microscopy force spectroscopy sensitivity for single molecule studies*. Journal of

Applied Physics, 2008. **104**(11): p. 114504.
30. Walters, D.A., Cleveland, J.P., Thomson, N.H., Hansma, P.K., Wendman, M.A., Gurley, G., and Elings, V., *Short cantilevers for atomic force microscopy*. Review of Scientific Instruments, 1996. **67**(10): p. 3583-3590.
31. Proksch, R., Schaffer, T.E., Cleveland, J.P., Callahan, R.C., and Viani, M.B., *Finite optical spot size and position corrections in thermal spring constant calibration*. Nanotechnology, 2004. **15**(9): p. 1344-1350.
32. Hutter, J.L. and Bechhoefer, J., *Calibration of Atomic-Force Microscope Tips*. Review of Scientific Instruments, 1993. **64**(7): p. 1868-1873.
33. Liu, Y. and Yang, J., *Coupling effects of refractive index discontinuity, spot size and spot location on the deflection sensitivity of optical-lever based atomic force microscopy*. Nanotechnology, 2008. **19**(23): p. 235501.
34. Rabe, U., Hirsekorn, S., Reinstadtler, M., Sulzbach, T., Lehrer, C., and Arnold, W., *Influence of the cantilever holder on the vibrations of AFM cantilevers*. Nanotechnology, 2007. **18**(4): p. 044008.
35. Timoshenko, S., *Vibration Problems in Engineering, 4th Ed.* 1974: Wiley, New York.
36. Rabe, U., Janser, K., and Arnold, W., *Vibrations of free and surface-coupled atomic force microscope cantilevers: Theory and experiment*. Review of Scientific Instruments, 1996. **67**(9): p. 3281-3293.
37. Turner, J.A. and Wiehn, J.S., *Sensitivity of flexural and torsional vibration modes of atomic force microscope cantilevers to surface stiffness variations*. Nanotechnology, 2001. **12**(3): p. 322-330.
38. Stark, R.W., *Optical lever detection in higher eigenmode dynamic atomic force microscopy*. Review of Scientific Instruments, 2004. **75**(11): p. 5053-5055.
39. Hecht, E., *Optics 4th edn*. 2002: Reading, MA: Addison Wesley Longman.
40. Rabe, U., Turner, J., and Arnold, W., *Analysis of the high-frequency response of atomic force microscope cantilevers*. Applied Physics a-Materials Science & Processing, 1998. **66**: p. S277-S282.
41. Giessibl, F.J., *Advances in atomic force microscopy*. Reviews of Modern Physics, 2003. **75**(3): p. 949-983.
42. Chen, X., Davies, M.C., Roberts, C.J., Tendler, S.J.B., Williams, P.M., and Burnham, N.A., *Optimizing phase imaging via dynamic force curves*. Surface Science, 2000. **460**(1-3): p. 292-300.
43. Boisgard, R., Michel, D., and Aime, J.P., *Hysteresis generated by attractive interaction: oscillating behavior of a vibrating tip-microlever system near a surface*. Surface Science, 1998. **401**(2): p. 199-205.
44. Sugawara, Y., Kobayashi, N., Kawakami, M., Li, Y.J., Naitoh, Y., and Kageshima, M., *Elimination of instabilities in phase shift curves in phase-modulation atomic force microscopy in constant-amplitude mode*. Applied Physics Letters, 2007. **90**(19): p. 194104.
45. Warren, O.L., Graham, J.F., and Norton, P.R., *Tapping mode imaging with an interfacial force microscope*. Review of Scientific Instruments, 1997. **68**(11): p. 4124-4131.
46. Joyce, S.A. and Houston, J.E., *A New Force Sensor Incorporating Force-Feedback Control for Interfacial Force Microscopy*. Review of Scientific

Instruments, 1991. **62**(3): p. 710-715.
47. Kato, N., Suzuki, I., Kikuta, H., and Iwata, K., *Force-balancing force sensor with an optical lever*. Review of Scientific Instruments, 1995. **66**(12): p. 5532-5536.
48. Sader, J.E., *Susceptibility of atomic force microscope cantilevers to lateral forces*. Review of Scientific Instruments, 2003. **74**(4): p. 2438-2443.
49. Giessibil, F.J., *Higher-harmonic atomic force microscopy*. Surface and Interface Analysis, 2006. **38**(12-13): p. 1696-1701.
50. Gates, R.S. and Reitsma, M.G., *Precise atomic force microscope cantilever spring constant calibration using a reference cantilever array*. Review of Scientific Instruments, 2007. **78**(8): p. 086101.

CHAPTER 4
A NEW AFM NANOTRIBOLOGY MODE FOR FRICTION COEFFICIENT*

Lateral scanning mode based on AFM provides frictional image on samples, for example HOPG image in Figure 1.13. It has also played an important role in the fundamental study of friction mechanism at nanoscale. In addition, literatures have developed the lateral friction AFM as a chemical force microscopy to distinguish chemical groups on the surfaces. This chapter will describe a newly developed method for friction coefficient measurement, based on utilization of a T – shape cantilever with its off-axis tip [1] which has been discussed in the Chapter 1 of this thesis.

4.1 INTRODUCTION

Tribology covers fundamental researches and practical applications involving friction, lubrication, and wear of interacting surfaces in relative motion. The existence of tribology has been witnessed everywhere in our daily life and modern industry. Appropriate utilization of tribology can reap a significant amount of economic and environmental benefits such as the reduction in use of both energy and materials. Therefore, understanding the tribological phenomena especially frictional mechanisms of interfaces is of fundamental significance. With the recent trend of science and technology in making miniaturized devices at micro- and/or nano-scales [2-4], study of micro/nanotribology has become more important. To date, AFM has been developed as a powerful tool in lateral friction measurement [5-9], and for compositional mapping of surfaces at the nanometer scale [10, 11] as well.

In literature, two AFM methods have been proposed for friction coefficient measurement. The first one includes successive steps of calibrating the normal signal sensitivity, normal

* A modified version of this part has been published as: Liu, Y., Leung, K.M., Nie, H.Y., Lau, W.M., and Yang, J., “A new AFM nanotribology method using a T-shape cantilever with an off-axis tip for friction coefficient measurement with minimized Abbé error”, Tribology Letters, 2010.

stiffness, lateral signal sensitivity and lateral stiffness before measuring the friction coefficient. Although the normal sensitivity can be directly calibrated in the contact mode, it requires access to the optical geometry of AFM systems in order to calibrate the lateral sensitivity [12]. However access to the optical path is generally unavailable in commercial AFM systems. Therefore a number of special accessories were designed for measuring the lateral signal sensitivity [13-16] as shown in Figure 1.8. However strict requirements for the alignment tolerance increase the design complexity and related manufacturing cost. On the other hand, calculation of the lateral stiffness requires accurate information about the cantilever geometry and high degree of material homogeneity of the cantilever [17-19]. It is difficult for information of cantilever geometrical parameters to meet the required accuracy, and for the rigorous requirements to be satisfied.

As a result, the second method was developed for directly determining the conversion relationship between friction force coefficient and lateral voltage response, which bypasses the aforementioned difficulties in separate measurements of the lateral sensitivity and stiffness in the first method [10, 20, 21]. However this direct method needs a well-defined wedge as a tribolgoical reference, shown in Figure 1.10. Additional steps are required to scan both of the tilted and flat surfaces of the wedge at a given load to calculate the friction force calibration factor. Since the tilt angle of the wedge needs to be known exactly, the originally proposed calibration standard [20] used a treated $SrTiO_3$ specimen. Owing to the small dimensions of its terraces, the $SrTiO_3$ specimen is only suitable for very sharp probe. As an alternative, Tocha et al. [10] fabricated an universal calibration platform on a Si(100) wafer. The platform contains several notches with four different slopes with respect to the wafer surface. Accurate microfabrication process using focused ion beam milling was involved.

In this study, we have developed a simple AFM method by only using a T-shape cantilever with an off-axis tip for measuring friction coefficient. This new method does not require the aforementioned accessories and additional calibration steps. Thus it is easy-to-use, and needs the least operating procedures among the existing methods. In

addition, a very practical method has also been introduced, which can significantly reduce Abbé error.

4.2 THEORY

Recent progress in micro-/nano-fabrication technology allows us to fabricate T–shape optical-lever AFM cantilevers with an off-axis tip as shown in Figure 4.1, which are actually commercially available now. This type of cantilever has been extensively studied on torsional harmonic AFM for mapping materials properties at nanoscale [22-24]. Sahin and co-workers have developed the so-called HarmoniX® mode by tapping such a T-shape cantilever on a polymer sample, in which force-distance curves per tapping cycle are reconstructed and analyzed in real time for compositional mapping of Young's modulus, adhesion and energy dissipation of the sample [1].

We report here that, for the first time, a T-shape cantilever is applied in contact mode for fast friction coefficient measurement due to its unique T–shape design, as shown in Figure 4.2. The typical radius of the off-axis tip of a T-shape cantilever is less than 10 nm, which ensures that our measurement is in nanoscale contact. In contact mode, the change in normal voltage signal ΔV_n on the AFM photodetector is proportional to the normal loading force F_n by [10, 12, 16]

$$F_n = k_c S_n \Delta V_n \tag{4.1}$$

where S_n is deflection sensitivity and k_c is the normal stiffness of the cantilever used in this paper, nominally ~4N/m (HMX – 10, Veeco, Inc.). Both of the sensitivity and the stiffness can be accurately calibrated in experiments if the normal force needs to be known [25]. However, to be discussed in the following part, our technique saves the effort to calibrate the normal stiffness and lateral stiffness for friction coefficient measurement. We notice that, although this kind of cantilever was originally designed for tapping HarmoniX mode[1], such stiffness is much smaller than conventional tapping cantilever with typical stiffness ~ 40N/m. Therefore, they can be successfully applied in contact mode for many materials [8, 10, 26, 27].

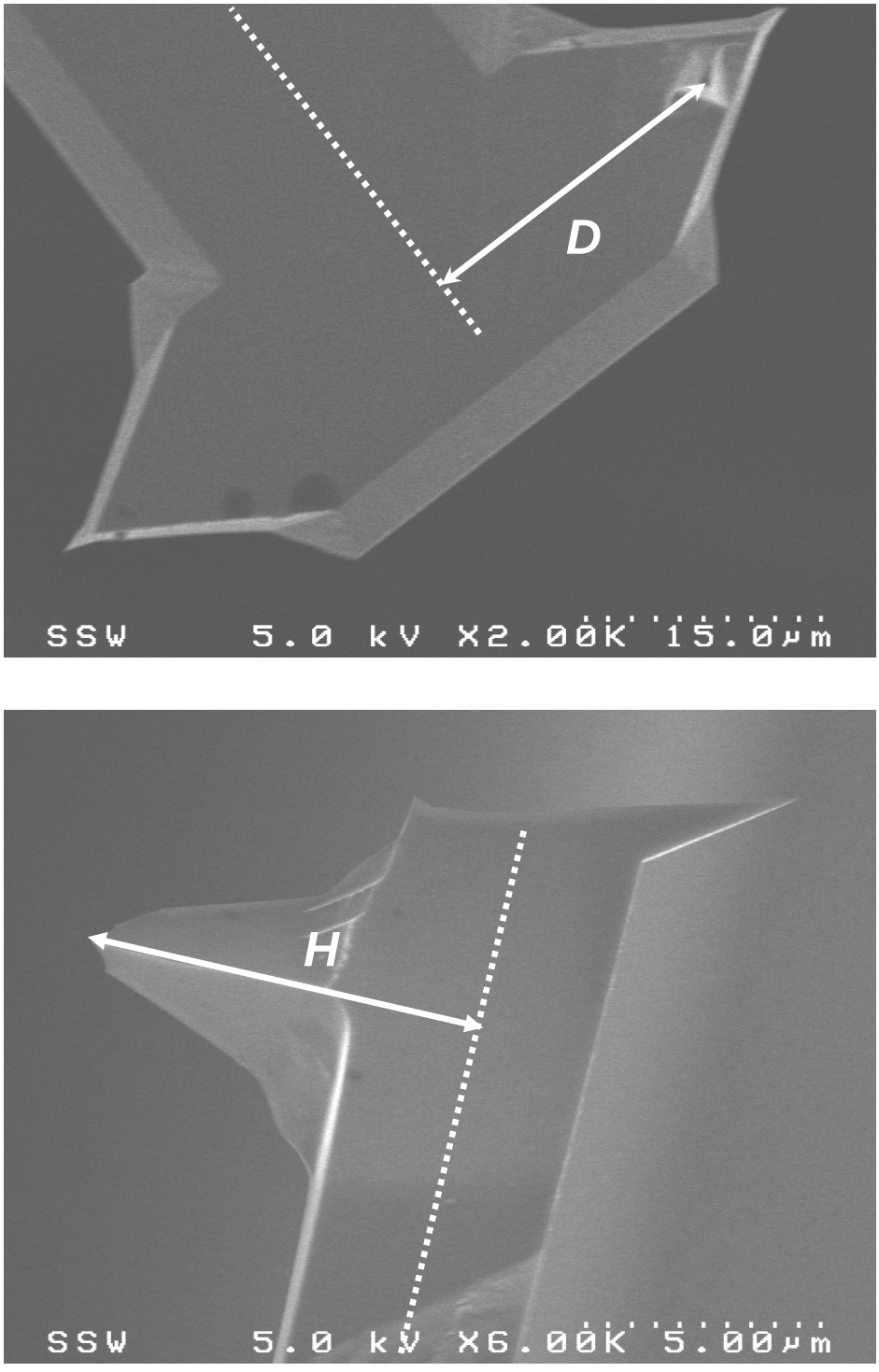

Figure 4.1 Scanning electron microscopic (SEM) images of a T–shaped cantilever whose tip height (*H*) of 8.45µm and tip offset (*D*) of 21.12µm have been characterized.

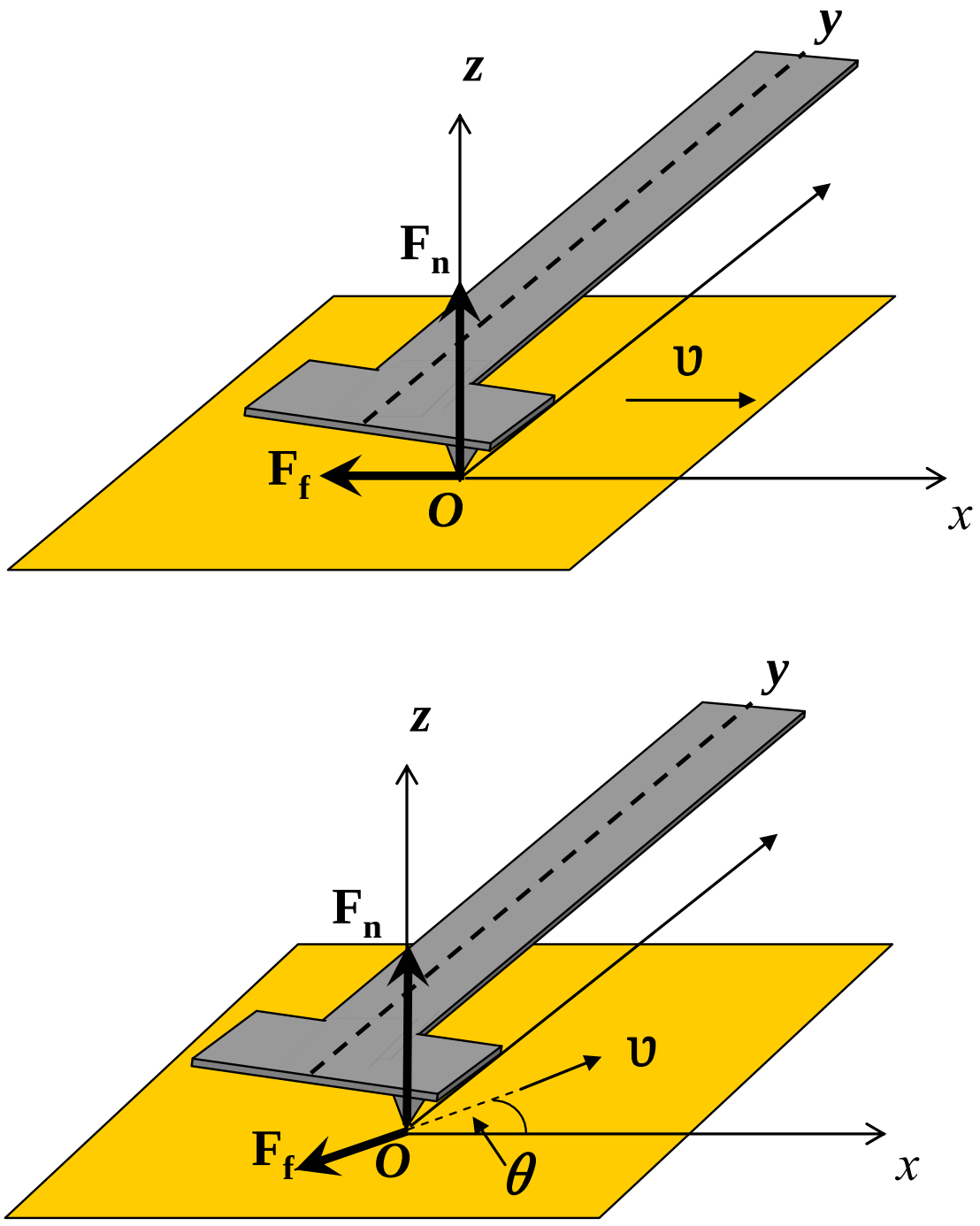

Figure 4.2 Schematics of using T–shape cantilever for measuring friction coefficient in contact mode. Left: (a) perfect alignment between the cantilever width axis and the scanning line; Right: (b) Abbé error *sinθ* involved due to misalignment between the cantilever width axis and the scanning line.

Due to the position of the off-axis tip, the normal load F_n induces a torque that twists the cantilever as shown in Figure 4.3(up), and the resultant change in the lateral voltage signal detected by the AFM photodetector is

$$\Delta V_{Ln} = C_0 F_n = C_0 k_c S_n \Delta V_n = C'_0 \Delta V_n \tag{4.2}$$

C'_0 is a coefficient constant as calibrated by monitoring the lateral signal through increasing the normal voltage but without commencing scan (scan size = 0 nm or the tip is not moving). C'_0 is independent of the substrate in calibration, but affected by laser spot size, spot location and effective power received by the photodetector [28, 29]. Therefore the coefficient C'_0 should be always re-calibrated whenever the cantilever is changed. The calibration of C'_0 can be implemented on the measured sample so that there is no any additional accessory in need for reference.

Once commencing the lateral scan, under the normal force F_n there is a friction force F_f between the tip and the sample. Both F_n and F_f can cause twisting of the T-shape cantilever as shown in Figure 4.3(bottom), and hence cause a additional change of lateral voltage signal on the photodetector. However, the change of the lateral voltage due to F_n can be decoupled and offset from the total lateral voltage. Therefore, we are able to detect the lateral voltage change due to F_f, ΔV_{Lf}, only. ΔV_{Lf} is the half-width of the "friction loop" during lateral scanning as shown in Figure 4.4.

The lateral voltage change due to F_f can be expressed as

$$\Delta V_{Lf} = C_1 F_f = C_0 F'_n \tag{4.3}$$

where F'_n is an equivalent normal force of F_f assuming that F'_n causes the same torsional moment as F_f about the longitudinal axis of the cantilever. They can be correlated as

$$F'_n = \frac{F_f H}{D} \tag{4.4}$$

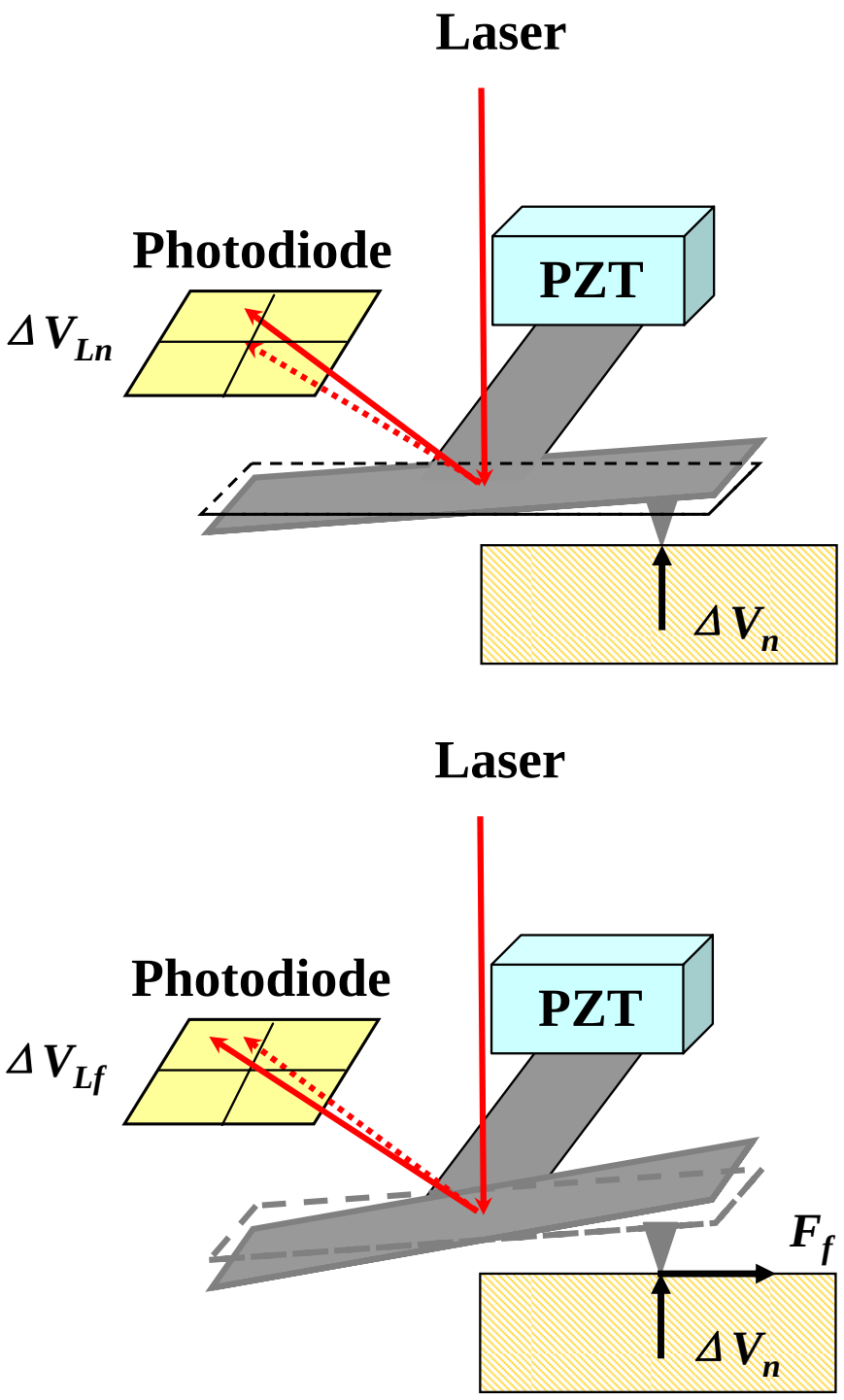

Figure 4.3 The principle of measuring friction coefficient: (up) without scanning, the increase of loading twists the T – shape cantilever; (bottom) with lateral scanning, the friction force further twists the cantilever.

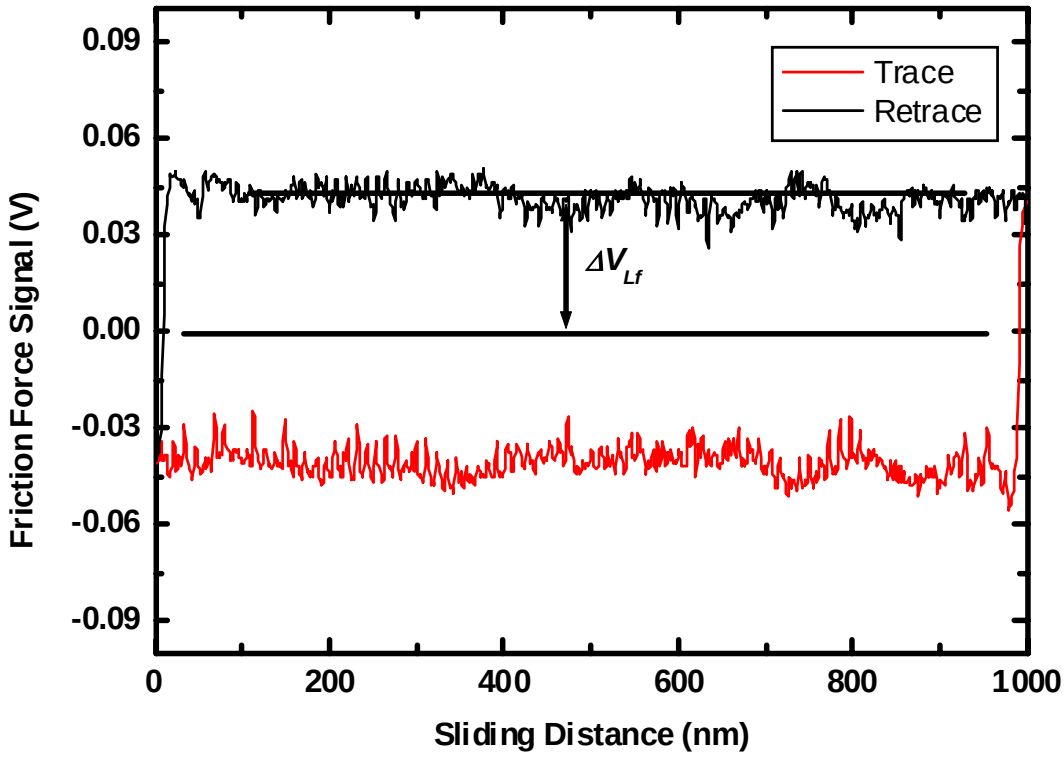

Figure 4.4 Determination of ΔV_{Lf} from the half-width of "friction loop" obtained in lateral scanning

Therefore

$$F_f = \frac{\Delta V_{Lf} D}{C_0 H} \tag{4.5}$$

where H is the height of the tip and D is the distance from the tip to the longitudinal axis of the cantilever as depicted in the scanning electron microscopy (SEM) images shown in Figure 4.1.

The friction coefficient can be finally expressed as [20]

$$\mu = \frac{F_f}{F_n} = \frac{\Delta V_{Lf}}{C_0 F_n} \frac{D}{H} = \frac{\Delta V_{Lf} D}{C_0 k_c S_n \Delta V_n H} = \frac{\Delta V_{Lf}}{C'_0 \Delta V_n} \frac{D}{H} \tag{4.6}$$

As a result, our method only needs to detect the normal voltage signal ΔV_n and the lateral voltage signal related to F_f, ΔV_{Lf}, for measuring the friction coefficient.

4.3 DISCUSSION OF ERROR SOURCES

Abbé error, which is encountered in friction coefficient measurement, is engendered by misalignment between measuring straight line (x – axis) and scanning straight line [30]. Herein we provide a solution to minimize its effect. Firstly, we define a Cartesian reference coordinate *O-xyz*: x axis and y axis are along the width direction and the length or longitudinal direction of the cantilever, respectively, and they are located in the scanning $x - y$ plane; z axis is normal to the scanning plane (see Figure 4.2). Ideally, we expect that the lateral scanning line is in perfect coincidence with the x axis. However, when loading the cantilever on the probe holder, there is always misalignment between the cantilever longitudinal axis and y axis. As a result, Abbé error, $\sin\theta$, is introduced and the y-axis component of friction force causes a longitudinal buckling on the cantilever by [30]

$$V_{Vn} = C_1 F_f \sin\theta \tag{4.7}$$

where θ is the Abbé (misalignment) angle.

Such buckling results in additional deflection of the cantilever and introduces additional normal voltage signal on V_n. It causes an error in measurement of friction coefficient. Nevertheless, based on Equation (4.7), if we can adjust the scanning angle in $x - y$ plane to compromise the Abbé angle θ, there is a possibility to reduce the related effect. As demonstrated in Figure 4.5, when the tip scans with perfect alignment $\theta = 90°$, there is no friction loop on the normal voltage signal, and both of trace and retrace scan lines overlap; in other misalignment cases such as $\theta = 0°$, 89° or 92° friction loops clearly appear, where the upper curve is due to positive buckling and lower curve is due to negative buckling. Through this no-friction-loop method, we can effectively minimize the Abbé error within 1° in our experiments. Our AFM system can only allow the least increment or decrement of scanning angle by 1°, thus 1° is the limit for the minimization of the Abbé angle.

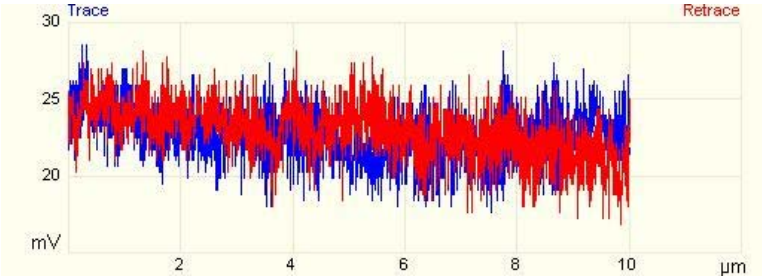

90 °

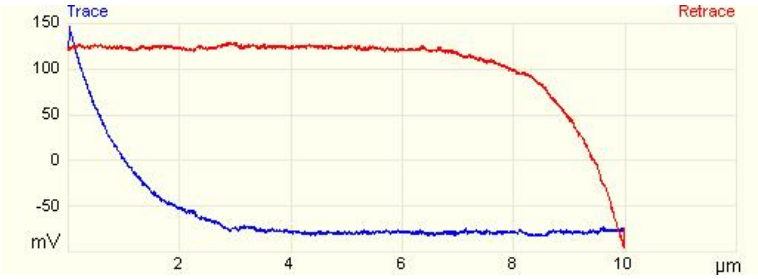

0 °

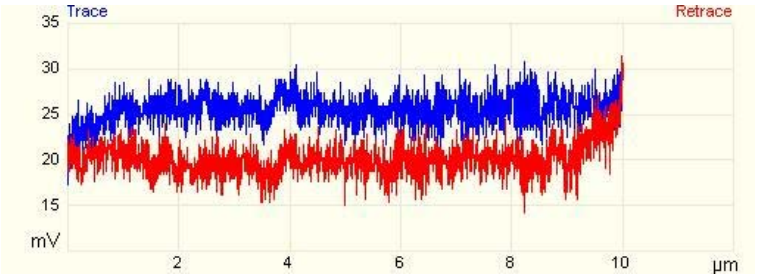

92 °

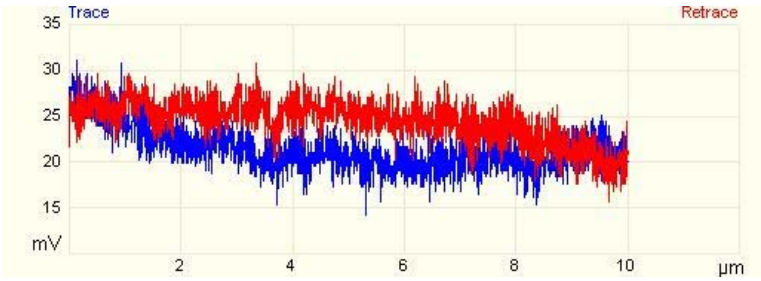

89 °

Figure 4.5 Normal voltage signals of the AFM photodetector at different θ with lateral scanning size 10 μm on sapphire. Top left: $\theta = 90^{\circ}$; Top right: $\theta = 0^{\circ}$; Bottom Left: $\theta = 92^{\circ}$; Bottom right: $\theta = 89^{\circ}$.

4.4 EXPERIMENTS

4.4.1 Friction Coefficients of polystyrene, mica and HOPG

In the first study, the coefficient constant C'_0 of the T-shape cantilever in Equation (4.2) is 0.1586 as shown in Figure 4.6, which was calibrated on a sapphire sample. For the cantilever used here, *H* and *D* were measured on SEM to be 8.45 μm and 21.12 μm, respectively. SEM is a convenient tool in precisely measuring these two geometrical parameters of the T-shaped cantilever. The SEM we used was a Hitachi S-4500, which was calibrated using a standard for dimension measurements. Because the resolution of an SEM is usually several nanometres, the characterization of the micrometer-scale *H* and *D* of a cantilever is simple and fast. For example, it took less than half an hour for us to obtain the images shown in Figure 4.1. This step can even be done after all experiments have been finished. For commercially available cantilevers, their dimensions, such as cantilever thickness and tip height, can vary to a substantial extent. For example, according to the manufacturer, the tip height, *H*, of the T-shaped cantilever we used is specified within the range of 4 to 10 μm. *D* is not even specified by the manufacturer, though it may be close to the width of the cantilever. Therefore, it is necessary for us to actually measure the dimensions such as *H* and *D* in order to ensure accurate measurement of friction coefficient in our method. SEM appears to be the most practical technique to measure cantilever dimensions.

As shown in Figure 4.7, the measured slopes $\frac{\Delta V_{Lf}}{\Delta V_n}$ on polystyrene (PS), freshly cleaved mica and HOPG are 0.02484, 0.02359 and 0.00035 in ambient environment (humidity ~50% and at temperature ~22°C), respectively. The corresponding friction coefficients according to Equation (4.6) are listed in Table 4.1. These values fall correspondingly in the ranges of friction coefficients reported in literature for these samples [31-34] as shown in Table 4.1 as well. We therefore confirm the validation of the proposed method for friction coefficient measurement. Specially, a softer T – shaped cantilever with stiffness ~0.18N/m was recently customized by Dong et al. [35]. Softer T – shape cantilevers with spring constant less than 1N/m have also been commercially available

(HXMS, Veeco. Inc) and therefore our technique could be extended for imaging much softer samples including self-assemble monolayers [36] and living cells [37] in contact mode.

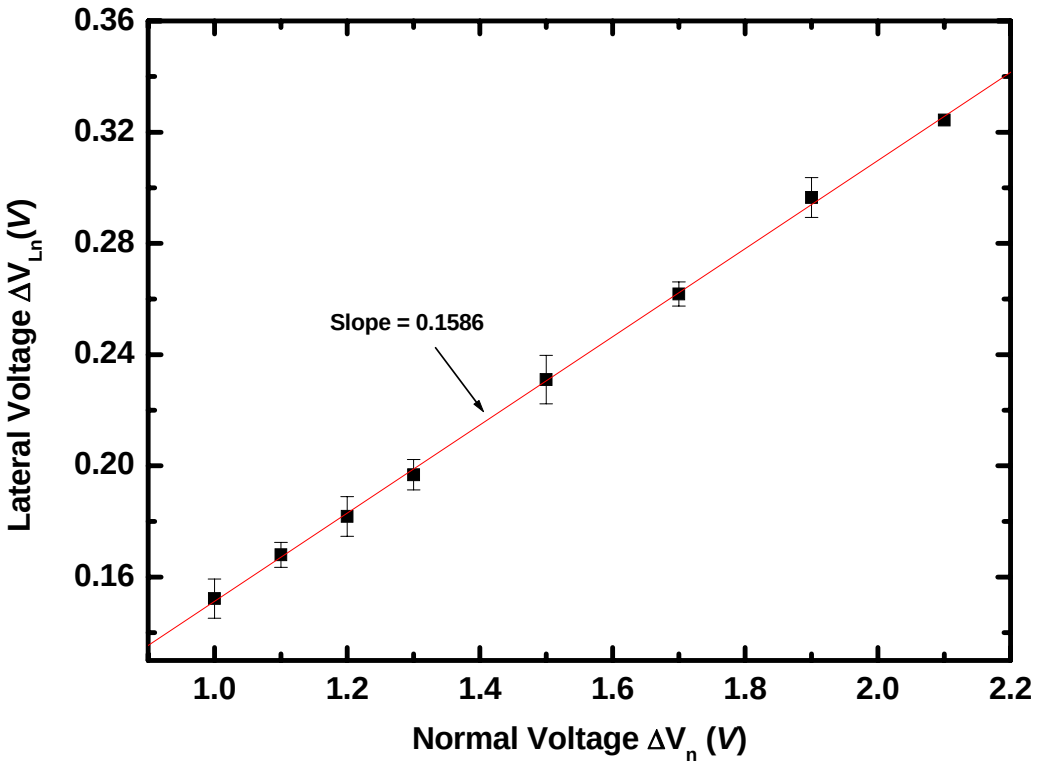

Figure 4.6 Calibration of the coefficient C'_0 according to the linear relationship between the resultant lateral voltage signal ΔV_{Ln} and the normal voltage ΔV_n when an increasing normal load applied to the tip without scanning.

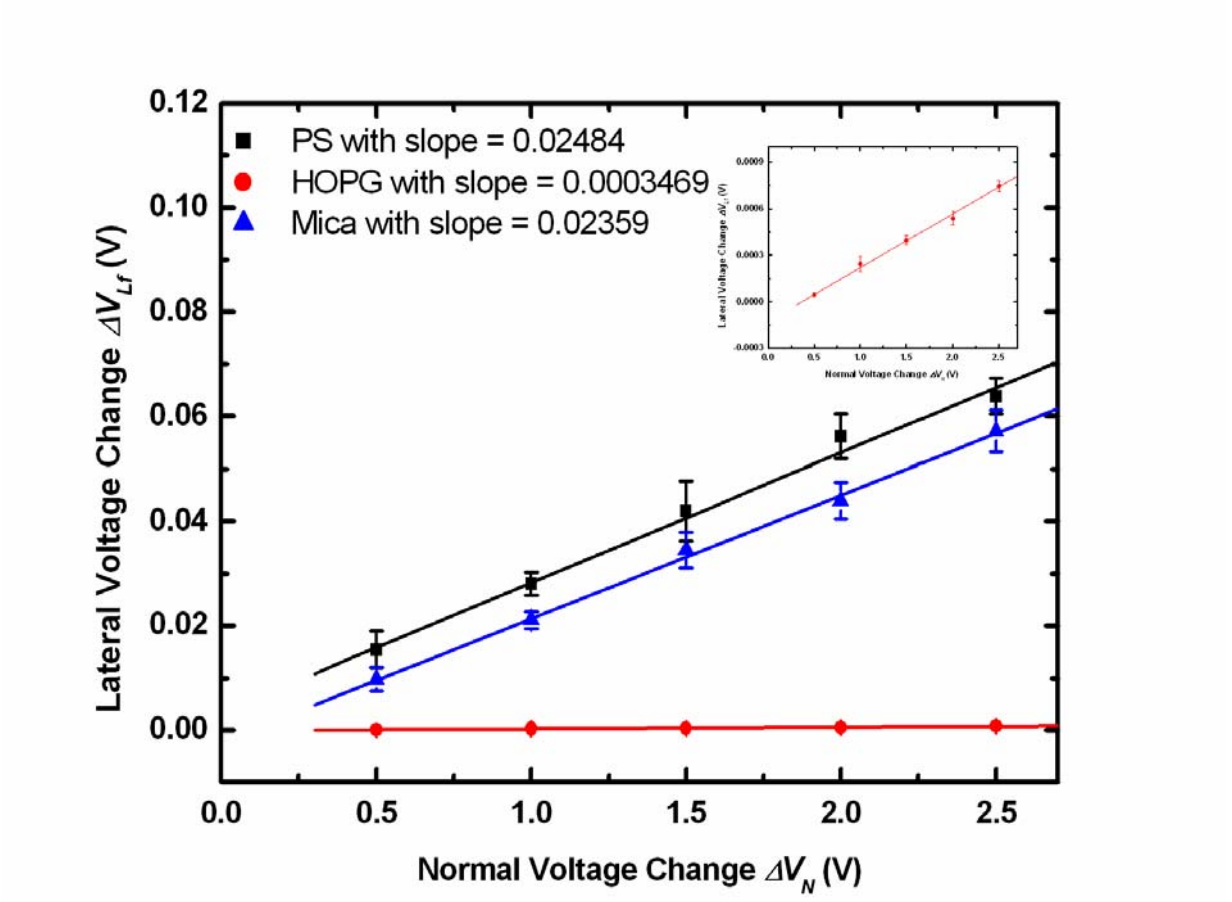

Figure 4.7 The relationship between the lateral voltage signal related to F_f, ΔV_{Lf}, and the normal voltage signal ΔV_n when increasing the normal load with scan size 1 um and scan rate 1 Hz on samples of polystyrene, freshly cleaved mica and freshly cleaved HOPG in ambient air with humidity 50% and at temperature 22°C.

4.4.2 Chemical Force Microscopy to Distinguish Chemical Groups on Self – Assembled Monolayers

As an advancement of the proposed cantilever method as applied in chemical force microscopy, we have designed another experiment of mapping quantitatively friction coefficient distribution of a composite surface consisted of self-assembled monolayers (SAMs). The composite surface was made by the micro-contact printing method [38]

patterning two different self-assembled monolayers (SAMs), mercaptoundecanoic acid (MUDA) $HS(CH_2)_{10}COOH$ and dodecanethoil(DCT) $HS(CH_2)_{11}CH_3$, on Au surface.

All chemicals were used as received, unless otherwise stated. MUDA and DCT were purchased from Sigma Aldrich. Bare and fresh Si (100) wafer was cleaned and cut into ~1.5cm by 1.5cm pieces. And a thin gold layer with thickness around 40 ~ 50nm was sputtered on each piece of Silicon. The Au substrate was immediately sent for micro-contact printing.

Micro-contact-printed self-assembled monolayers (SAMs) on Au substrates were prepared according to published procedures[38]. The PDMS stamp was fabricated on the prepared pattern by curing the degassed pre-polymer and initiator (10:1) mixture in a heater for 2 hours at 80ºC, and then peeled off gently. The PDMS stamp was fixed on a customized printing device for printing as shown in Figure 4.8. We first wetted the stamp with an "ink" of MHDA solution (~2mM in ethanol) and bring it into contact with the Au substrate for 10 ~20s. The MHDA transfers from the stamp to the gold upon contact, forms patterns (brighter areas) as shown in Figure 1.14. The patterned SAM with –COOH groups was rinsed with ethanol, DI water and dried in a N_2 stream. Then the whole Au substrate was immersed into ~2mM solution of ODT for 10 ~20s, followed by rinsing with ethanol, DI water and dried in a N_2 stream. The whole process is summarized in Figure 4.9.

We carried the friction coefficient measurement on the composite surface using the newly developed method as described before. In friction measurements of the SAMs, the scanning rate was setting as 40μm/s (1Hz and 20μm by 20μm scan size). Figure 4.10 clearly shows the contrast between –COOH domain and $–CH_3$ domain. In this second experiment as chemical force microscopy, the required dimensions of T – shape cantilever are measured as D = 19.21μm and tip height H = 6.26μm on SEM. The corresponding coefficient C'_0 is calibrated as shown in Figure 4.11 and equal to 0.2214.

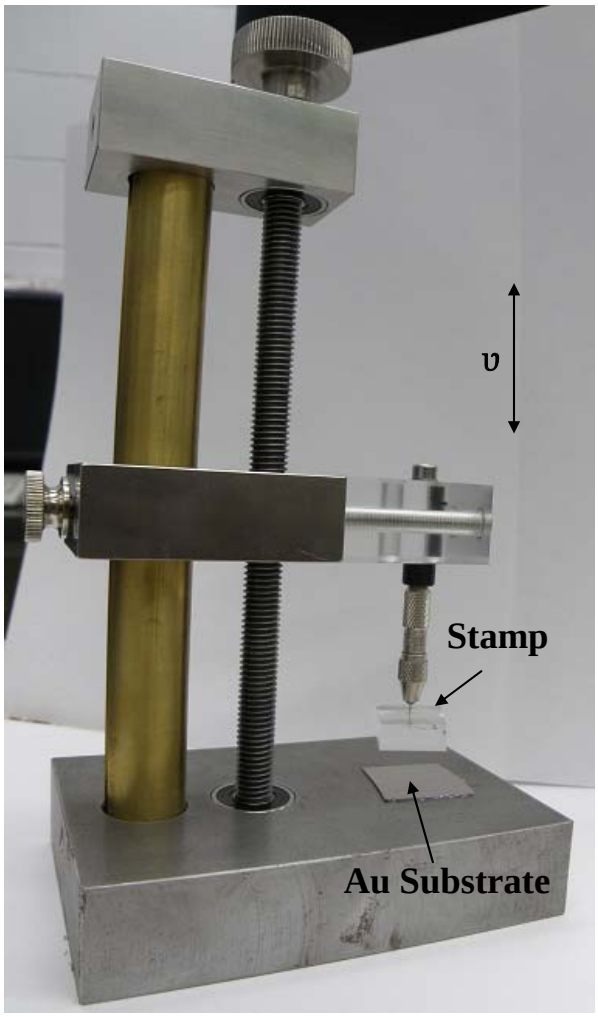

Figure 4.8 Experimental setup of micro-contact printing system by manual.

After laterally scanning the surface with increasing the normal load, the lateral friction images in Figure 4.10 show higher contrast between –COOH and $–CH_3$ head groups. The corresponding friction force distributions reveal that both the difference between the mean (peak point) friction forces as well as the peak widths increase with higher normal load. This is due to a higher friction coefficient of the hydrophilic areas compared to the hydrophobic areas for the hydrophilic silicon tip as used in this measurement. Therefore, the slopes for –COOH domain and $–CH_3$ domain were obtained as shown in Figure 4.12: 0.0097 ± 0.0011 and 0.0066 ± 0.0008, respectively. Based on Equation (4.6), the friction coefficients for mercaptoundecanoic $HS(CH_2)_{10}COOH$ and dodecanethoil $HS(CH_2)_{11}CH_3$

are 0.134 ± 0.015and 0.091 ± 0.011, respectively. These values are in match with the reported results from the literatures [39, 40] for the same SAMs molecules under a similar humidity condition. Table 4.1 provides a comparison between our results and results in literatures.

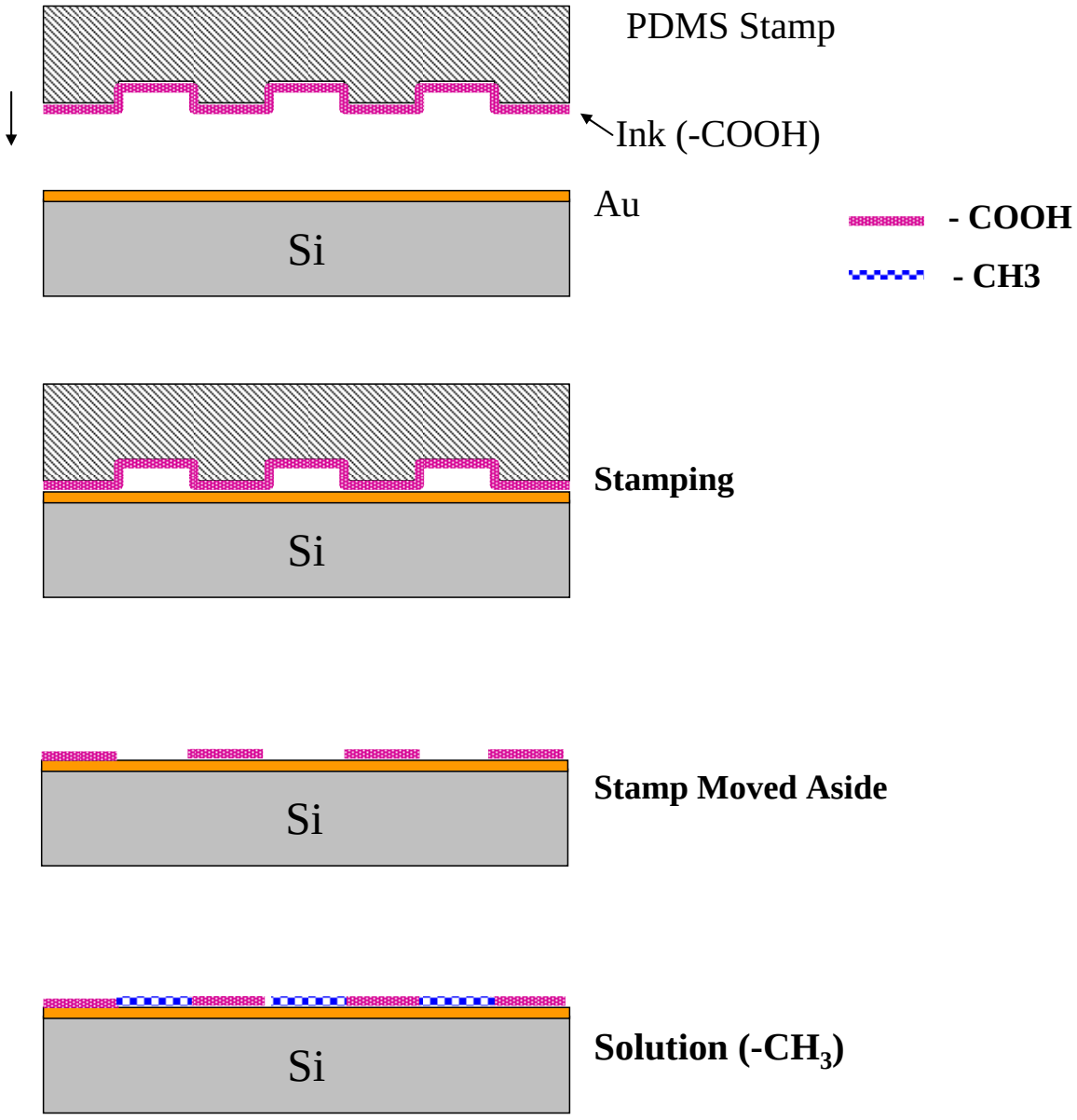

Figure 4.9 Procedures of micro-contact printing SAMs

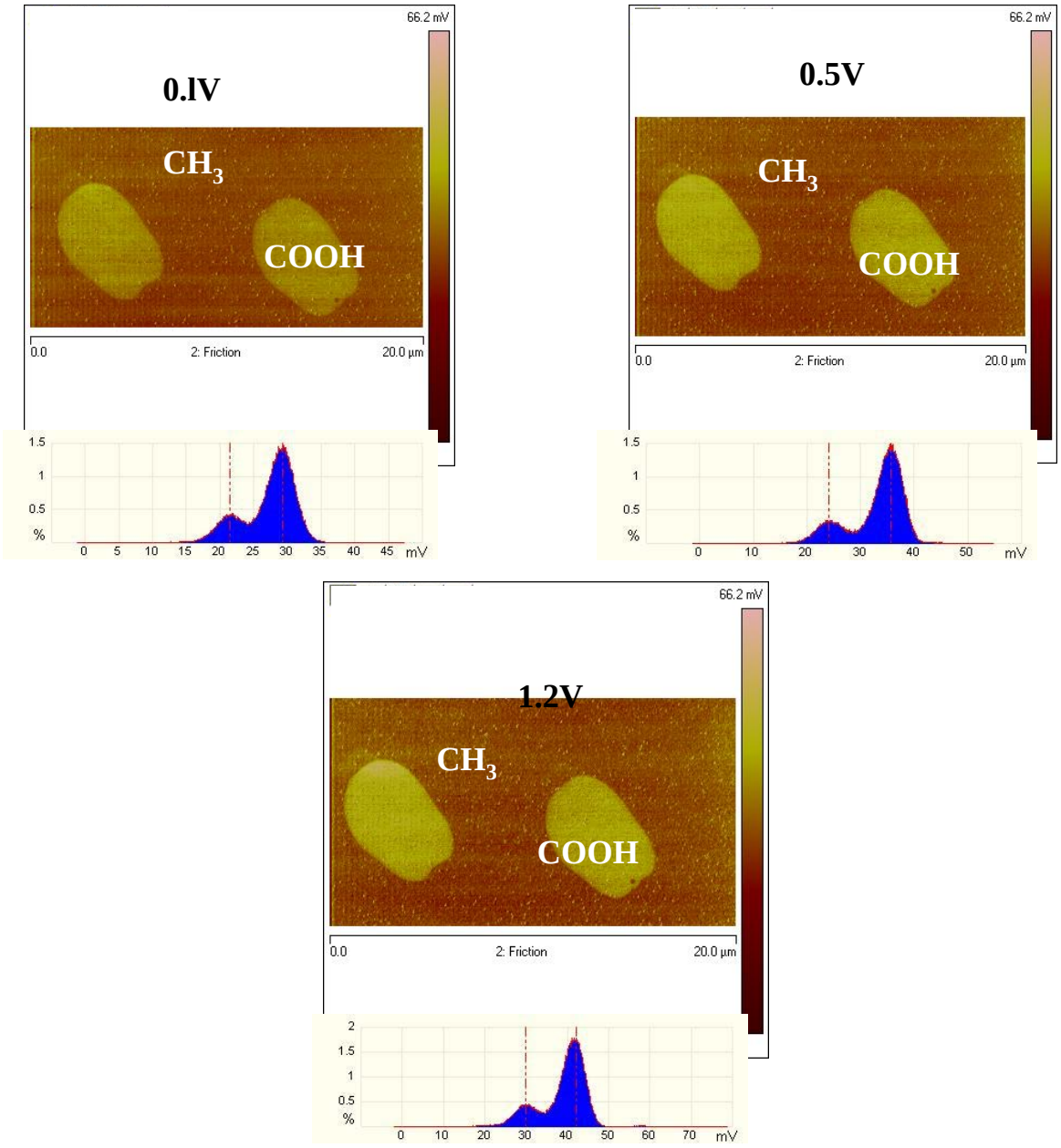

Figure 4.10 Friction contrast of a –COOH and –CH_3 SAMs pattern under different normal load. Experiments were performed by the newly developed nanotribology method using a silicon HXMS-T – shape cantilever with nominal spring constant less than 1.0N/m from Veeco, Inc. The scanning speed is 40µm/s.

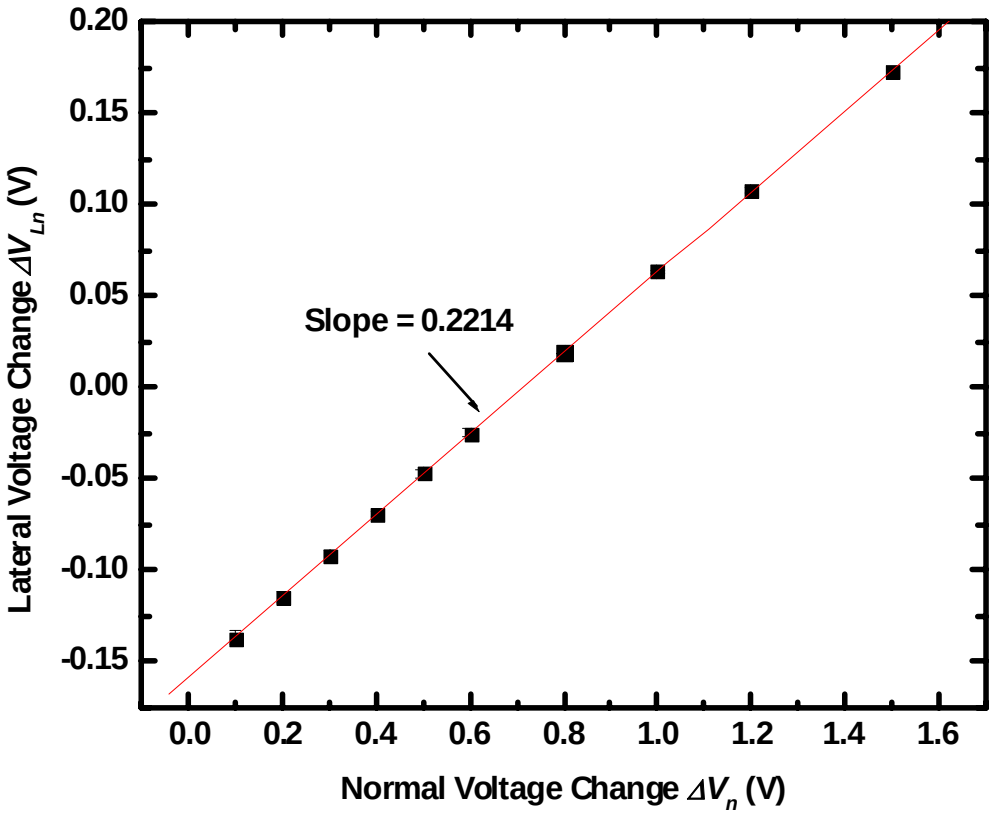

Figure 4.11 Calibration of the coefficient C'_0.

4.4.3 Further Discussion

Our method relies on the use of the T–shape cantilever in contact mode. For a traditional cantilever, there is always, more or less, a tip offset *D* due to microfabrication defects. However, for them, the uncertainty in measuring *D* using SEM probably is at the same order of the value of *D,* which will cause large deviation if we use Equation (4.6). But the uncertainty in measuring *D* of a T–shape cantilever is negligible compared with the value of *D*. In further, larger *D* will generate larger twist signal on photodetector due to normal load at zero scanning and therefore the slope C'_0 is larger. Based on Equation (4.6), the larger C'_0 can provide higher sensitivity to measuring smaller friction coefficient. Thus T–shape cantilever design with deliberated tip offset improves the experimental accuracy

in this method. In friction coefficient measurement, experimental errors may come from scan size, noise level, and sample roughness.

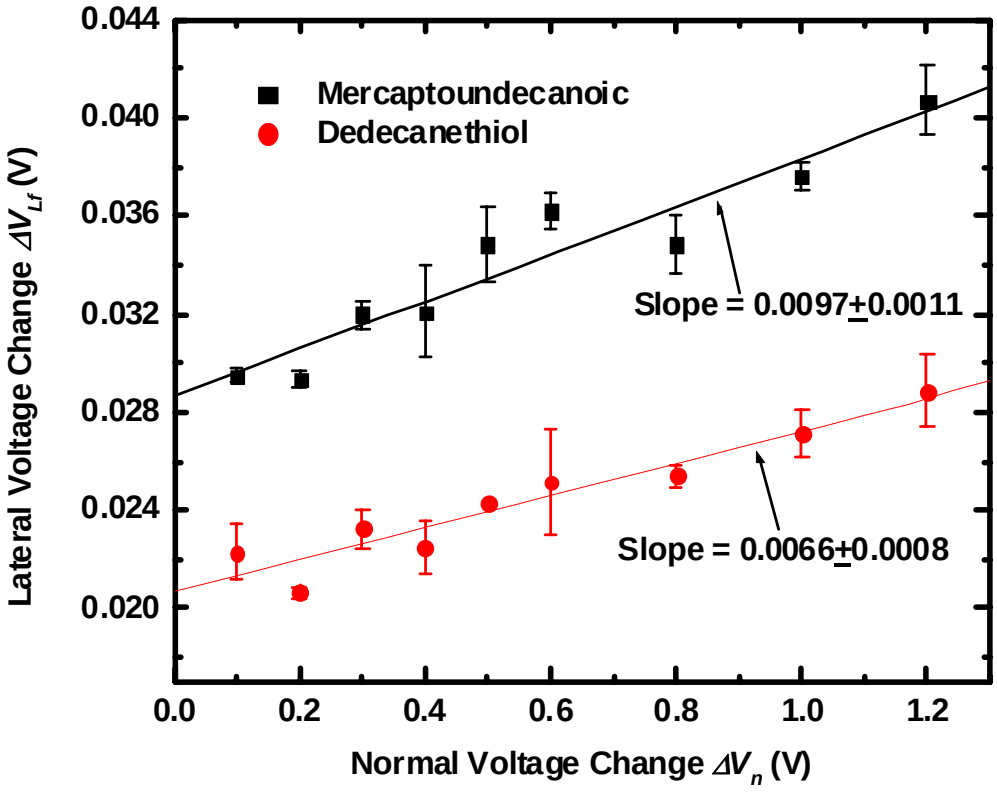

Figure 4.12 Calibration of the relationship between ΔV_{Lf} and ΔV_n for hydrophilic and hydrophobic groups.

4.5 CONCLUSIONS

In summary, we have developed a simple and accurate AFM nanotribology method for fast friction coefficient measurement at nanometer scale. This method takes advantage of a T-shape cantilever with an off-axis tip AFM, and eliminates necessities of complex and rigorous calibration procedures in advance and/or any accessories during experimental preparation. The T-shape cantilever as applied in contact can decouple the linear

relationship between the lateral signal and friction force, from that between the lateral signal and normal force. Friction coefficient is completely determined by the calibrated relationships. With this proposed method, we examined the major error source and introduced the no-friction-loop method for minimizing Abbé error. This work has enriched our capability to apply AFM methodology for nanotribology research as well as in chemical force microscopy to map chemical groups on complex surface at nanometer scale.

Table 4.1: Comparison of friction coefficients measured by our T – shape cantilever method and the conventional AFM methods. All experiment conditions are similar: room temperature and relative humidity, RH ~ 50%.

Sample	T – shape Cantilever method	Conventional method(s)
PS	0.391	0.33 – 0.50 [32] 0.458 [34]
Fresh Cleaved Mica	0.371	~ 0.33 [33] 0.05 – 0.3 [32]
HOPG	0.005	~0.006 [31]
$HS(CH_2)_{10}CO_2H$	0.134	~0.15[40]
$HS(CH_2)_{11}CH_3$	0.091	~0.081[39]

4.6 REFERENCES

1. Sahin, O., Magonov, S., Su, C., Quate, C.F., and Solgaard, O., *An atomic force microscope tip designed to measure time-varying nanomechanical forces*. Nature Nanotechnology, 2007. **2**(8): p. 507-514.
2. Maboudian, R. and Carraro, C., *Surface chemistry and tribology of MEMS*. Annual Review of Physical Chemistry, 2004. **55**: p. 35-54.
3. Canter, N., *Understanding friction laws at the nanoscale and their relation to the macroscale*. Tribology & Lubrication Technology, 2009. **65**(7): p. 10-11.
4. Mo, Y.F., Turner, K.T., and Szlufarska, I., *Friction laws at the nanoscale*. Nature, 2009. **457**(7233): p. 1116-1119.

5. Gerbig, Y.B., Ahmed, S.I.U., Chetwynd, D.G., and Haefke, H., *Effect of nanoscale topography and chemical composition of surfaces on their microfrictional behaviour*. Tribology Letters, 2006. **21**(2): p. 161-168.
6. Terada, Y., Harada, M., Ikehara, T., and Nishi, T., *Nanotribology of polymer blends*. Journal of Applied Physics, 2000. **87**(6): p. 2803-2807.
7. Szlufarska, I., Chandross, M., and Carpick, R.W., *Recent advances in single-asperity nanotribology*. Journal of Physics D-Applied Physics, 2008. **41**(12): p. 123001.
8. Mate, C.M., Mcclelland, G.M., Erlandsson, R., and Chiang, S., *Atomic-Scale Friction of a Tungsten Tip on a Graphite Surface*. Physical Review Letters, 1987. **59**(17): p. 1942-1945.
9. Li, J.W., Wang, C., Shang, G.Y., Xu, Q.M., Lin, Z., Guan, J.J., and Bai, C.L., *Friction coefficients derived from apparent height variations in contact mode atomic force microscopy images*. Langmuir, 1999. **15**(22): p. 7662-7669.
10. Tocha, E., Schonherr, H., and Vancso, G.J., *Quantitative nanotribology by AFM: A novel universal calibration platform*. Langmuir, 2006. **22**(5): p. 2340-2350.
11. Tamayo, J., Gonzalez, L., Gonzalez, Y., and Garcia, R., *Compositional mapping of semiconductor structures by friction force microscopy*. Applied Physics Letters, 1996. **68**(16): p. 2297-2299.
12. Liu, E., Blanpain, B., and Celis, J.P., *Calibration procedures for frictional measurements with a lateral force microscope*. Wear, 1996. **192**(1-2): p. 141-150.
13. Bogdanovic, G., Meurk, A., and Rutland, M.W., *Tip friction - torsional spring constant determination*. Colloids and Surfaces B-Biointerfaces, 2000. **19**(4): p. 397-405.
14. Xie, H., Vitard, J., Haliyo, S., and Regnier, S., *Optical lever calibration in atomic force microscope with a mechanical lever*. Review of Scientific Instruments, 2008. **79**(9): p. 096101.
15. Li, Q., Kim, K.S., and Rydberg, A., *Lateral force calibration of an atomic force microscope with a diamagnetic levitation spring system*. Review of Scientific Instruments, 2006. **77**(6): p. 065105.
16. Cannara, R.J., Eglin, M., and Carpick, R.W., *Lateral force calibration in atomic force microscopy: A new lateral force calibration method and general guidelines for optimization*. Review of Scientific Instruments, 2006. **77**(5): p. 053701.
17. Green, C.P., Lioe, H., Cleveland, J.P., Proksch, R., Mulvaney, P., and Sader, J.E., *Normal and torsional spring constants of atomic force microscope cantilevers*. Review of Scientific Instruments, 2004. **75**(6): p. 1988-1996.
18. Neumeister, J.M. and Ducker, W.A., *Lateral, Normal, and Longitudinal Spring Constants of Atomic-Force Microscopy Cantilevers*. Review of Scientific Instruments, 1994. **65**(8): p. 2527-2531.
19. Wei, Z.Q., Wang, C., and Bai, C.L., *Investigation of nanoscale frictional contact by friction force microscopy*. Langmuir, 2001. **17**(13): p. 3945-3951.
20. Ogletree, D.F., Carpick, R.W., and Salmeron, M., *Calibration of frictional forces in atomic force microscopy*. Review of Scientific Instruments, 1996. **67**(9): p. 3298-3306.

21. Varenberg, M., Etsion, I., and Halperin, G., *An improved wedge calibration method for lateral force in atomic force microscopy*. Review of Scientific Instruments, 2003. **74**(7): p. 3362-3367.
22. Mullin, N., Vasilev, C., Tucker, J.D., Hunter, C.N., Weber, C.H.M., and Hobbs, J.K., *"Torsional tapping" atomic force microscopy using T-shaped cantilevers*. Applied Physics Letters, 2009. **94**(17): p. 173109.
23. Sahin, O. and Erina, N., *High-resolution and large dynamic range nanomechanical mapping in tapping-mode atomic force microscopy*. Nanotechnology, 2008. **19**(44): p. 445717.
24. Legleiter, J., *The effect of drive frequency and set point amplitude on tapping forces in atomic force microscopy: simulation and experiment*. Nanotechnology, 2009. **20**(24): p. 245703.
25. Hutter, J.L. and Bechhoefer, J., *Calibration of Atomic-Force Microscope Tips*. Review of Scientific Instruments, 1993. **64**(7): p. 1868-1873.
26. Nie, H.Y., Motomatsu, M., Mizutani, W., and Tokumoto, H., *Local elasticity measurement on polymers using atomic force microscopy*. Thin Solid Films, 1996. **273**(1-2): p. 143-148.
27. Hoh, J.H. and Engel, A., *Friction Effects on Force Measurements with an Atomic-Force Microscope*. Langmuir, 1993. **9**(11): p. 3310-3312.
28. Proksch, R., Schaffer, T.E., Cleveland, J.P., Callahan, R.C., and Viani, M.B., *Finite optical spot size and position corrections in thermal spring constant calibration*. Nanotechnology, 2004. **15**(9): p. 1344-1350.
29. Liu, Y. and Yang, J., *Coupling effects of refractive index discontinuity, spot size and spot location on the deflection sensitivity of optical-lever based atomic force microscopy*. Nanotechnology, 2008. **19**(23): p. 235501.
30. Pegna, J., *Generalized Abbe principle: Position error propagation in machine elements*. Journal of Mechanical Design, 1997. **119**(1): p. 1-7.
31. Ruan, J.A. and Bhushan, B., *Atomic-Scale Friction Measurements Using Friction Force Microscopy .1. General-Principles and New Measurement Techniques*. Journal of Tribology-Transactions of the Asme, 1994. **116**(2): p. 378-388.
32. Schumacher, A., Kruse, N., Prins, R., Meyer, E., Luthi, R., Howald, L., Guntherodt, H.J., and Scandella, L., *Influence of humidity on friction measurements of supported MoS2 single layers*. Journal of Vacuum Science & Technology B, 1996. **14**(2): p. 1264-1267.
33. Schwarz, U.D., Zworner, O., Koster, P., and Wiesendanger, P., *Quantitative analysis of the frictional properties of solid materials at low loads .2. Mica and germanium sulfide*. Physical Review B, 1997. **56**(11): p. 6997-7000.
34. Breakspear, S., Smith, J.R., Nevell, T.G., and Tsibouklis, J., *Friction coefficient mapping using the atomic force microscope*. Surface and Interface Analysis, 2004. **36**(9): p. 1330-1334.
35. Dong, M.D., Husale, S., and Sahin, O., *Determination of protein structural flexibility by microsecond force spectroscopy*. Nature Nanotechnology, 2009. **4**(8): p. 514-517.
36. Oncins, G., Vericat, C., and Sanz, F., *Mechanical properties of alkanethiol monolayers studied by force spectroscopy*. Journal of Chemical Physics, 2008. **128**(4): p. 044701.

37. Le Grimellec, C., Lesniewska, E., Giocondi, M.C., Finot, E., Vie, V., and Goudonnet, J.P., *Imaging of the surface of living cells by low-force contact-mode atomic force microscopy*. Biophysical Journal, 1998. **75**(2): p. 695-703.
38. Xia, Y.N. and Whitesides, G.M., *Soft lithography*. Angewandte Chemie-International Edition, 1998. **37**(5): p. 551-575.
39. Li, L.Y., Chen, S.F., and Jiang, S.Y., *Nanoscale frictional properties of mixed alkanethiol self-assembled monolayers on Au(111) by scanning force microscopy: Humidity effect*. Langmuir, 2003. **19**(3): p. 666-671.
40. Li, L.Y., Yu, Q.M., and Jiang, S.Y., *Quantitative measurements of frictional properties of n-alkanethiols on Au(111) by scanning force microscopy*. Journal of Physical Chemistry B, 1999. **103**(39): p. 8290-8295.

CHAPTER 5
AFM CHARACTERIATION OF THIN FILMS UNDER LOW-ENERGY HYROGEN BOMBARDMENT*

A low-energy hydrogen bombardment process has been recently developed for engineering polymeric surface. AFM is applied in this study as one major tool to characterize the physical effects of the hydrogen bombardment on surfaces properties of thin films.

5.1 INTRODUCTION

There has been a remarkable growth of applications of organic thin films over the past years, such as wetting control [1], biotechnology [2], organic electronics [3, 4], optics and photonics [5, 6], data storage [7, 8] and chemical sensors [9, 10]. These applications need novel surface techniques to modify physical and/or chemical properties of thin films to meet various requirements. Traditional approaches for molecular cross-linking on a surface are wet chemical processes that rely on reactions of radicals and/or ions with organic molecules [11-15]. In these processes, specific chemical additives are used to introduce reactive sites for cross-linking[12], and consequently chemical disposal needs to be properly handled in the post processes.

Environmental sustainability has become an emerging issue, which therefore requires us to develop more environmentally-friendly green techniques to maintain our ecosystem by minimizing disposal of pollutant chemicals into environment. To lessen chemical usage and disposal, a promising technique for surface modification has been invented using mass-separated ion beam to modify solid surfaces [16]. In this study, we applied a newly developed green process, a low-energy hydrogen bombardment method, to modify the physical properties of organic thin films. This method precisely controls neutral-charge

* A modified version of this part has been submitted to ACS Applied Materials and Interfaces: Liu, Y., Yang, D.Q., Nie, H.Y., Lau, W.M., and Yang, J. “Study of a Hydrogen bombardment process for molecular cross-linking with thin films”.

hydrogen projectiles, which carry ~10eV kinetic energy, to bombard the thin films. In such a way, this method enables modification of physical properties of thin films without using any chemical additives. Because of the use of the neutral-charge hydrogen projectiles, this method largely alleviates the surface charging effect that is commonly found in conventional ion/plasma-based bombardments [17-20]. In addition, this technique owns the potential to avoid dielectric damage on coatings esp. in the applications of semiconductor industry [21, 22].

The physical principle of hydrogen bombardment is straightforward. According to the first-approximation of hard-sphere binary collision, when a projectile collides head-on with a target its energy can be most effectively transferred. The energy transfer fraction can be determined by $4M_tM_p/(M_t+M_p)^2$ [23, 24] as listed in Table 5.1. Theoretically, the maximum energy transferred from a 10eV hydrogen projectile to a hydrogen atom of the molecule charin is 10eV. From the atomic point of view, the effective energy left after collision, between the hydrogen projectile and the H atom, can break a C–H bond with bond energy 4.3eV (as listed in Table 5.2). However, if the 10eV hydrogen projectile colloids with a C atom of the molecule chain, the maximum energy transferred is only 2.8eV, which is not enough to break a C – C bond with energy 3.6eV. The schematic illustration of the hydrogen bombardment process is depicted in Figure 5.1.

Table 5.1 Maximum energy transferred from hydrogen projectiles to target atoms

Atom – Atom Interaction	10eV H – H	10eV H – C	5eV H – H	5eV H – C	15eV H – H	15eV H – C
Transferred Energy (eV)	10	2.8	5	1.4	15	4.3

Table 5.2 Bond energy for typical chemical bonds

Chemical bond	C – H	C – C	C = C (π bond)
Bond Energy (eV)	4.3	3.6	2.7

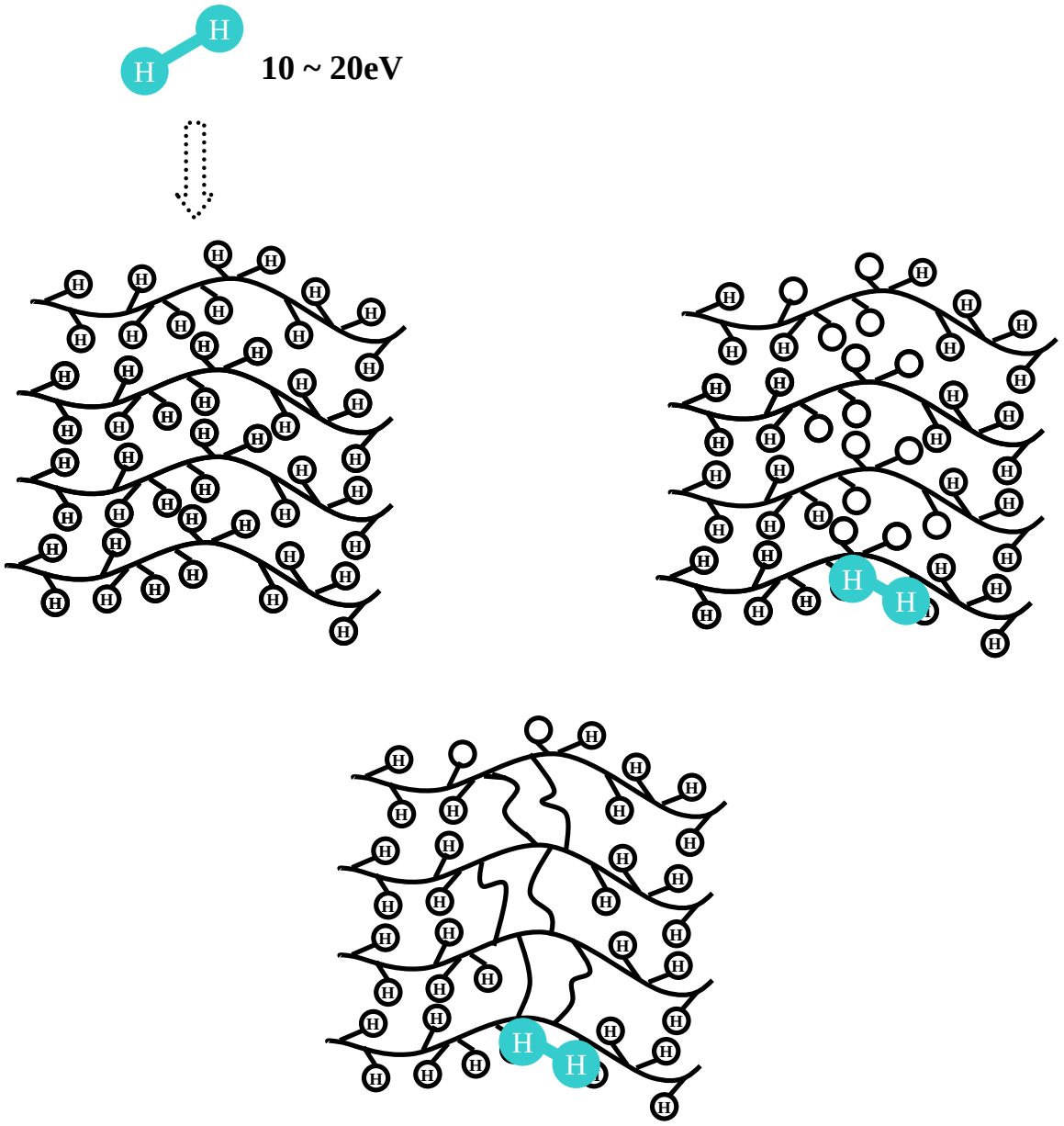

Figure 5.1 Schematics of generation of carbon radicals and formation of cross-linked chains due to the low-energy hydrogen bombardment.

Long-chain n-alkane molecules $CH_3(CH_2)nCH_3$ have been recognized as main ingredients of organic and biological molecules [25, 26], which have led to a great amount of theoretical and experimental research in polymer science and engineering [27-29]. They are also of industrial importance as lubricant additives in applications of

adhesion, lubrication and coatings [30]. Since n-alkane molecules have linear molecular structure and have only saturated C-C, they are good sample molecules for characterizing our hydrogen bombardment process. Herein dotriacontane $C_{32}H_{66}$ was chosen as a prototypical molecule system for this study.

Two characterization tools were used: X-ray photoelectron spectroscopy (XPS) and atomic force microscopy (AFM). XPS was first used to determine chemical component, i.e. carbon. AFM was used as the major tool to interpret the physical effects of the low-energy hydrogen bombardment on the $C_{32}H_{66}$ monolayers, i.e. morphological and mechanical properties at the nanoscale. Both contact and tapping AFM modes have been successfully applied to study thin layers from different aspects [31-34]. In this paper HarmoniX^{TM} [35, 36] and force modulation [37] AFM modes were utilized to characterize the mechanical strength of the thin films before and after the treatment of the hydrogen bombardment.

5.2 THEORY

5.2.1 Brief of XPS Principle

XPS, also named as electron spectroscopy for chemical analysis, is a sensitive and quantitative spectroscopic technique to measure the elemental compositions within a material. It can provide information on both atomic concentration and chemical states of the surface constituents [38]. XPS utilizes a source of X – rays with a known energy of E_{photo} to irradiate a sample surface under ultra – high vacuum condition. The X – ray photos penetrate and interact with the inner – shell electrons of the atom. If the irradiation energy is sufficiently high, these electrons interacting with the photos are able to leave the atoms by overcoming the work function ϕ of the spectrometer. Therefore, we have the binding energy according to [38]:

$$E_{binding} = E_{photo} - \left(E_{kinetic} + \phi\right) \tag{5.1}$$

where $E_{kinetic}$ is the kinetic energy of the electron as collected and measured by the spectroscopy. In order to eliminate the term ϕ, the binding energy of a stable element can

be used as a reference, such as a sputter – cleaned Au standard surface which is grounded to the spectrometer. Finally, according to the Equation (5.1), once the value of $E_{kinetic}$ is measured, XPS can offer us identification of elements with specific binding energy $E_{binding}$.

5.2.2 AFM: Tapping Mode, Force Modulation and HarmoniX™

AFM can provide both of topography and other properties of the surface at nanometer scale. We are especially interested in the mechanical property of surface which may be affected by the hydrogen bombardment.

Through tapping mode AFM, the phase shift can be approximately proportional to reduced Young's modulus of the sample [39] by:

$$\Delta\phi \approx \zeta \langle a \rangle E^* \left(\frac{Q}{k_c} \right) \tag{5.2}$$

where ζ is a number between 1.9 and 2.4 [39], Q is the quality factor, k_c is cantilever stiffness, and $\langle a \rangle$ is time-average contact radius over one oscillating cycle of the tapping AFM. E^* is the reduced Young's modulus as:

$$\frac{1}{E^*} = \frac{1-\nu_{tip}^2}{E_{tip}} + \frac{1-\nu_{sample}^2}{E_{sample}} \tag{5.3}$$

E_{tip} and E_{sample} are Young's moduli, and ν_{tip} and ν_{sample} are Poisson's ratios, of the tip and sample, respectively.

With the tapping condition such that setting point is ~ 60% of the freely vibrating amplitude[40], in phase image we can visibly distinguish softer and harder areas on the surface. However, the phase shift in tapping mode AFM could only be qualitatively associated with mechanical property variations in the presence of viscoelasticity and/or adhesion hysteresis [41].

To quantitatively understand the enhanced stiffness of bombarded layers, force modulation [37] mode and HamoniX™ [36] mode were applied. In force modulation AFM, the cantilever basis is low frequency modulated while tip is in contact with the surface. A stiffer area on the surface deforms less than a softer area and generates higher vibrating amplitude. With the Hertzian theory of elastic circular point contact applied, the Young's modulus of sample can be correlated with cantilever amplitudes as follows [37]. The compression ratio is given:

$$\varepsilon = \frac{z_c}{z_f} \tag{5.4}$$

where z_c is the excitation amplitude of the cantilever; and z_f is the amplitude of the cantilever exerting force on a sample with finite stiffness. Then, Young's modulus can finally be determined by

$$E_{sample} = \frac{\varepsilon}{1-\varepsilon} HE_{tip} \tag{5.5}$$

where H is related to apparatus ccoefficient [37]. The force modulation AFM has a separate piezoelectric actuator to independently modulate the probe (Veeco Application Note: Force Modulation Imaging with Atomic Force Microscopy).

For HamoniX™ [36] mode, a T – shape cantilever is vibrated as in tapping mode and twisted by the interaction between the tip and sample. The torsional response signal to noise is much significant than that with flexural response. When the tip hit the sample, the cantilever bends torsionally in proportion to the torque generated by the tip – sample forces. Furthermore, there was an existing transfer function to map the relationship between first torsional response and tip – sample interaction:

$$H_T(\omega) = c_{optical} \frac{\omega_T^2 / K_T}{\omega_T^2 - \omega^2 + i\omega\omega_T / Q_T} \tag{5.6}$$

where ω is the angular frequency, ω_T is the torsional resonance frequency, $c_{optical}$ is a scalar multiplier corresponding to the bending angle of the cantilever for a unit tip displacement in the torsional mode, Q_T is the quality factor of the torsional resonance, and K_T is the effective spring constant of the torsional resonance. Time resolved tapping

force can be calculated based on this equation using the monitored torsional deflection signal. With approximately known vertical position of the tip, the force – displacement curve can be finally obtained and the Young's modulus can be calculated based on DMT model or Hertz model.

These two modes are well complementary to each other. In theory, force modulation can be used for measuring Young's modulus at any order. However, it is still operating in contact mode and easily damages soft samples with low stiffness. Especially in air when there is large capillary force involved, the engagement of soft cantilever on surface is embarrassing. HamoniX^{TM} mode, which works as torsional tapping mode carrying a T – shape cantilever, can measure a large dynamic range of mechanical properties from 1MPa to 10GPa [42]. It is a tapping mode and well suitable for measuring the polymer thin films with very low stiffness.

5.3 MATERIALS AND METHOD

Sample Preparation: A 0.3 wt.% Dotriacontane, $CH_3(CH_2)_{30}CH_3$, solution in hexane was spin coated on to a silicon (100) wafer covered by a native oxide layer. When the coating was performed on a spin coater with 5000 rpm for 1 min, this concentration of doctriacontane solution can form "fractal-like island" monolayer as shown in Figure 5.3. We already carried out topography and phase images at difference sites on the samples and confirmed that under this condition there was only single perpendicular monolayer growing above the parallel layer. Seven samples with different bombardment times were prepared for experiments. Total two runs of experiments were carried for statistical analysis.

Hydrogen Bombardment: The low-energy hydrogen bombardment was performed with a home-built and low-cost mass-separated low energy ion beam system [16, 24, 43, 44], which delivers a hydrogen beam to the target substrate in a high vacuum chamber. Hydrogen gas with the purity of 99.8% was used in the bombardments. The final beam energy was controlled at 10eV and the full width at half maximum of the energy distribution of hydrogen molecules was less than 0.6eV. The fluence was varied from

1×10^{16} cm^{-2} to 1×10^{18} cm^{-2} with the bombardment times from 5 s to 700 s but with other bombardment parameters kept same.

AFM Experiments: The morphology and mechanical properties of the monolayers were investigated on a commercially Dimension V AFM with Nanoscope V controller from Veeco Inc., which was equipped with a quadrant photodetector for detecting the cantilever deflection [45, 46]. All AFM experiments were performed in ambient environment. Rectangular silicon cantilevers from Nanoscience Instruments with nominal spring constant 0.03 N/m and 3.0 N/m were used in contact mode for height measurements and tapping mode for roughness measurements, respectively. A diamond-coated cantilever with calibrated tip radius 52 nm and spring constant 0.23 N/m from Nanoscience Instruments was used in force modulation. The tip used in HarmoniX^{TM} was with T shape and tip radius 8nm as calibrated by blunt method in SPIP software (Image Metrology); and its spring constant of 2.76 N/m was calibrated by thermal fluctuation method [47]. We calibrated the measurements of Young's modulus on PS-LDPE calibration sample (Veeco, Inc.) before, during and after experiments, as reference. There is no significant change on the Young's modulus of PS at ~2 GPa and LDPE ~0.1 GPa. It shows the consistence of our experiments.

5.4 EXPERIMENTS

5.4.1 XPS Results

XPS spectra of thin films as prepared are displayed in Figure 5.2, which were used for determining whether the chemical component have retained after our proposed bombardment. Spectrum of virgin thin films (Figure 2(a)) shows virtual C 1s signal at 285 eV from the $C_{32}H_{66}$ and Si 2s, Si 2p and O 1s signals detected from the substrate. Before hydrogen bombardment, the thin films are soluble in a hexane immersion for 5 min, which is shown by the significant reduction of the C 1s signal in XPS spectrum as in Figure 2(b). However, for the thin films bombarded by a 10 eV hydrogen beam up to 600 s, no visible changes in the intensity of C 1s signal can be found comparing XPS

spectrums before and after immersion in hexane as shown in Figure 2(c) and (d). Therefore, it is reasonable to point out the occurrence of the thoroughly cross-linking on

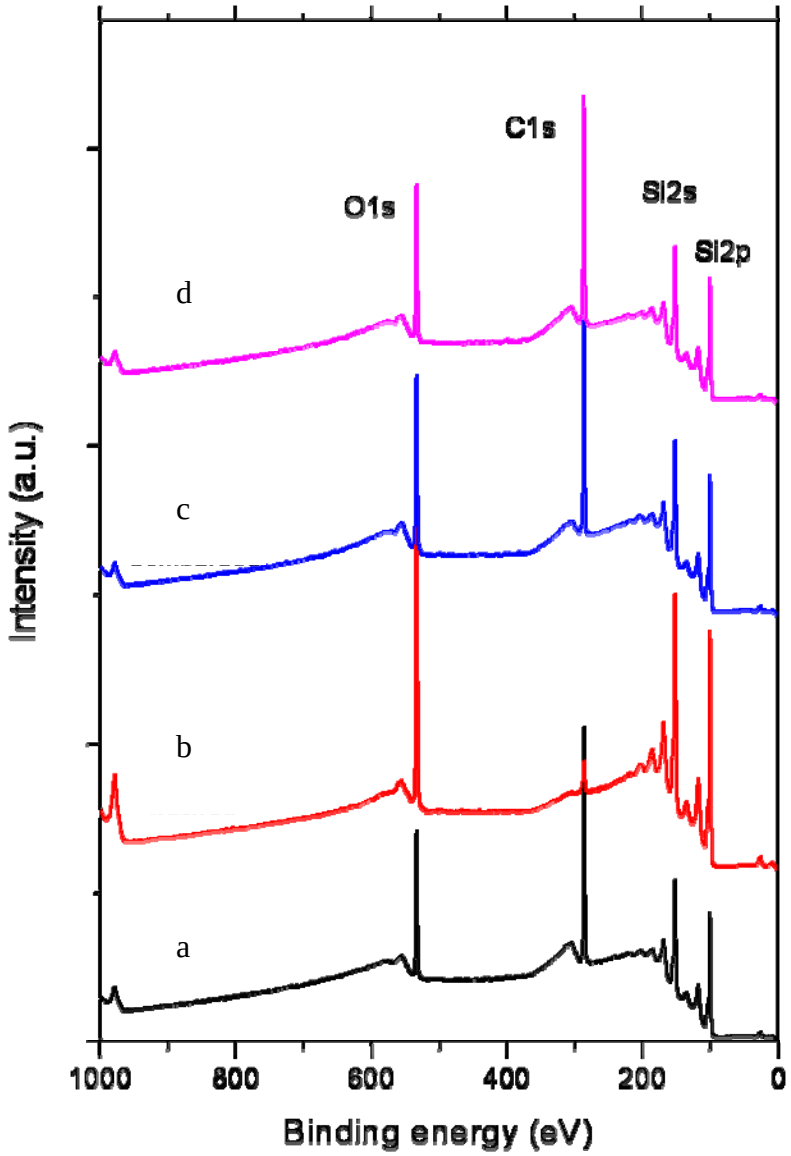

Figure 5.2 XPS survey spectra of (a) virgin $C_{32}H_{66}$ monolayer; (b) sample measured after 5 min hexane immersion; (c) 600 s bombarded $C_{32}H_{66}$ monolayer; (d) 600 s bombarded sample after 5 min hexane.

the bombarded monolayer after 600 s. In addition, the results present that the proposed hydrogen bombardment can not break C – C bonds (C 1s signals) and causes no main chain scission on the thin layers as mentioned before. We will use AFM to further illustrate physical effects of the thorough bombardment based on morphological and mechanical properties of the treated thin films.

5.4.2 Height and Denser Molecule Network by Bombardment

At the microscopic scale, the growth of *n*-alkane layers on SiO_2 surface has attracted increasing interests [27-29, 48-50]. Both of theoretical simulation [50] and experimental measurements [51, 52] confirmed such a structural model: one or two layers of $C_{32}H_{66}$ are immediately adsorbed on the SiO_2 surface with the long axis of the molecule parallel to the interface; and then additional layers are standing upright with the long axis oriented perpendicularly and all-trans length. Due to greatly different adhesion forces of parallel and perpendicular layers acting on AFM tip, amplitude-modulation tapping AFM measured “false step” heights for the all-trans and perpendicular monolayer adsorbed on a SiO_2 substrate. However, contact AFM clarified the height for the all-trans conformation of the *n*-alkane molecular monolayer[51]. We also confirmed the results and therefore utilized the contact AFM measurements for the heights of virgin $C_{32}H_{66}$ perpendicular monolayer and bombarded ones.

Through appropriate sample preparation i.e. 0.3 wt.% dotriacontane and 5000 rpm spin-coating speed in ambient, perpendicular monolayer resembling “fractal-like island” was formed [49] as shown in Figure 3. The height of perpendicular layer was measured as a function of bombardment time (Note: other bombardment parameters were kept same in this paper for our study; so that the different bombardment time corresponds to different bombardment fluence). The measurement results are shown in Figure 5.4. In literature, high-resolution ellipsometry has demonstrated that the height of an all-trans conformation of $C_{32}H_{66}$ monolayer is ~44 *Å* [48, 53]. From our results, the height of the virgin $C_{32}H_{66}$ monolayer was estimated to be 4.56 ± 0.19 nm, consistent with that of an all-trans conformation of the molecular monolayer. Through the hydrogen bombardment, Figure 4 shows that the monolayer height decreases with increase of bombardment time. At and

after bombardment time 600 s, the molecular layer height has become 2.58±0.08 nm, only about 57% of that the virgin layer. However, in our XPS results, the estimated layer

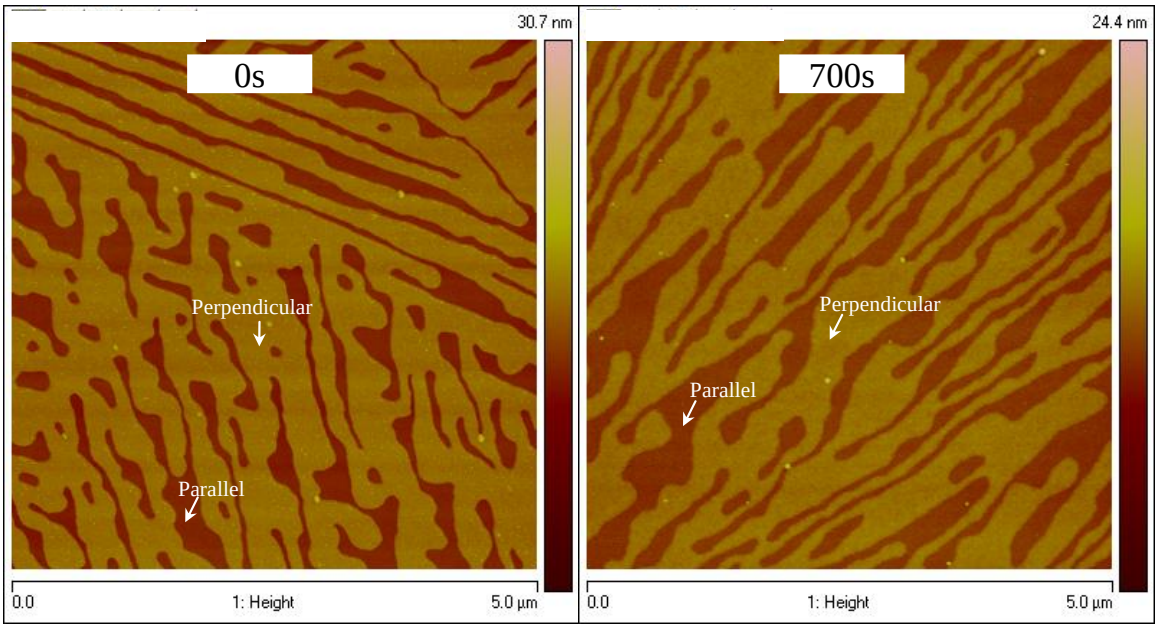

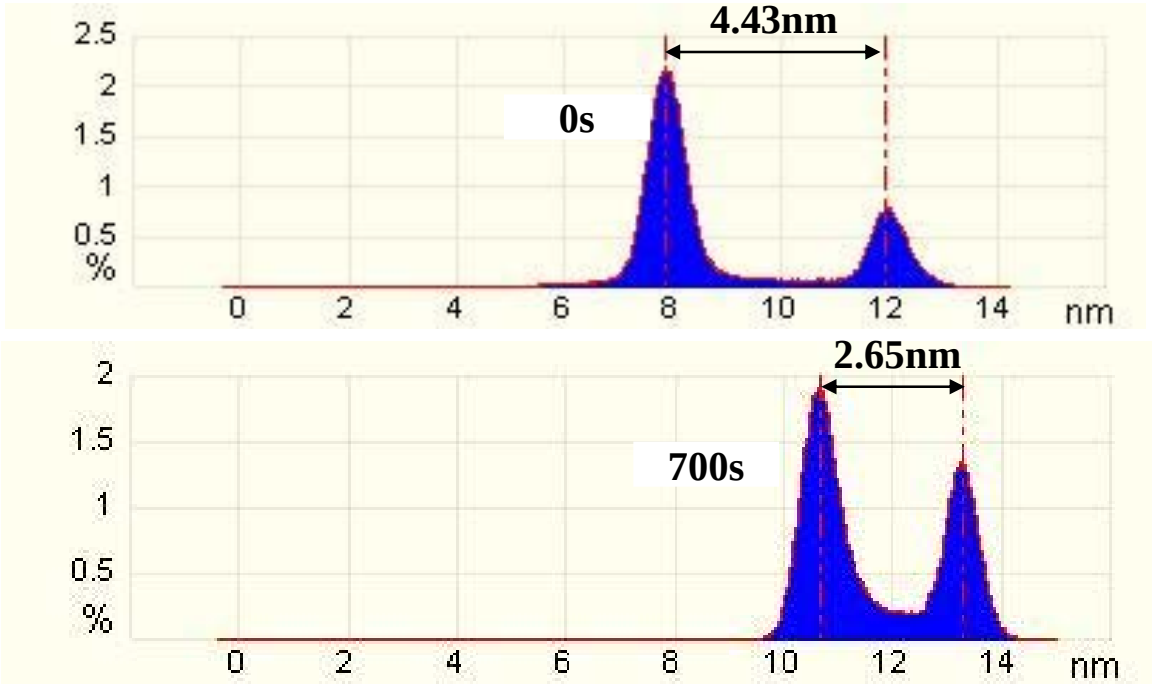

Figure 5.3 Topographic images (top) and heights (bottom) of $C_{32}H_{66}$ monolayer at 0 s and 700 s bombardment

thickness of 4.3±0.3 nm does not change with bombardment time. This comparison between AFM and XPS results suggest that the bombarded thin film becomes tightly cross-linking and forms denser molecular networks as a result of cross-linked C – C bonds between molecular chains. It was also noticed that thorough bombardment brought less variance on the height measurements of the perpedicular layers. Nevertheless, at the partial bombardment time step such as between 50 s and 400 s only random part of film was bombarded but other parts had not been affected. The resultant values of heights as measured could be non-uniform.

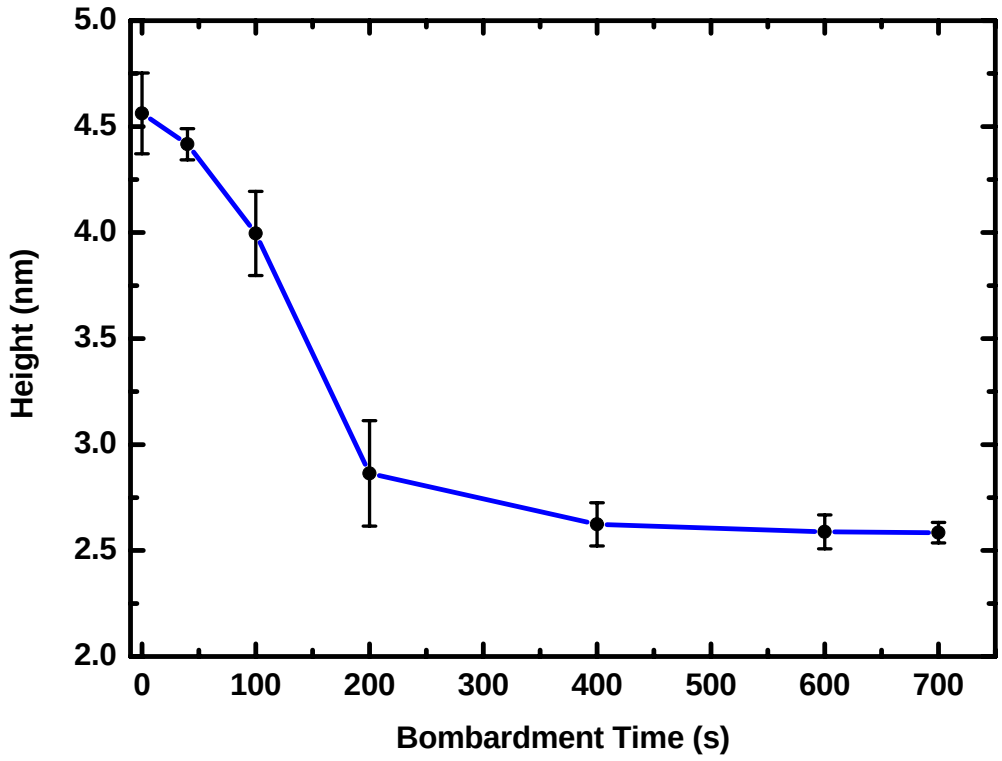

Figure 5.4 Contact AFM mode measurements of height decrease of $C_{32}H_{66}$ monolayer with increasing bombardment time

5.4.3 Roughness and Critical Bombardment Time

In the above discussion, the time at ~400 s represents a critical bombardment time and consequently necessary hydrogen fluence for thorough bombardment on the $C_{32}H_{66}$ thin

film. In this bombardment process, a bundle of hydrogen molecules are projected on the target. It is difficult to control the distribution of projectiles evenly on the sample surface and the collisions between hydrogen and C – H bonds are random. However, the collision average effects could be quantitatively determined based on the roughness measurements through two runs of experiments in our study. The referred roughness is defined as[54]

$$R_a = \frac{1}{NM}\sum_{j=1}^{M}\sum_{i=1}^{N}\left|z_{ij} - z_{average}\right| \tag{5.1}$$

The roughness R_a measurements were carried on the perpendicularly oriented monolayers with a constant scan area of 200 nm × 200 nm for all of samples [54]. Tapping mode was adopted as the characteristic means because it gently tunes the tapping force exerted on the monolayer [55] and owns statistical advantages to provide more reliable results on roughness measurements [56]. As shown in Figure 5.5, virgin $C_{32}H_{66}$ (perpendicular) monolayer has a very smooth surface of R_a = 0.14±0.02 nm, which is very close to the roughness of the supporting silicon substrate ~ 0.1 nm [57]. With increasing bombardment time, we noticed that the roughness on the bombarded surface increases with the increasing bombardment times; and at ~ 200 s, the roughness increased to a peak value at R_a = 0.70±0.04 nm. After further increase of bombardment time > 200 s, the roughness started to decrease and eventually the surface becomes very smooth again from ~ 400 s with a stable R_a at ~ 0.15±0.01 nm.

The results shown above first tell us that the well-bombarded alkane thin film surface can keep the same smooth surface as the virgin film. Secondly, the bombardment time at ~ 400 s specifies sufficient ion fluence required to implement thorough bombardment for the $C_{32}H_{66}$ thin film. Finally, at 200 s there is a maximum value ~ 0.70 nm on the whole roughness measurement plot, nearly five times larger than the roughness of virgin surface. This corresponds to a partially bombarded case (also shown in Figure 5.4) in which only local areas of the thin film surface were bombarded but other areas unaffected. This phenomenon can be further explained in such a way: in this experiment, we have $C_{32}H_{66}$ molecules perpendicularly aligning on substrate with an all-trans length; for a partial bombardment at ~ 200 s, some molecules were cross-linked with each other and then bent down but other intact molecules are still standing perpendicularly with its full length.

The uneven length distribution produced a rugged surface and as a result the roughness is high. Therefore, roughness measurements have been developed in this study as an efficient parameter to determine the bombardment process. This conclusion also confirms that in Figure 5.4 the measured variance of height values at 200 s is largest due to the maximum roughness herein.

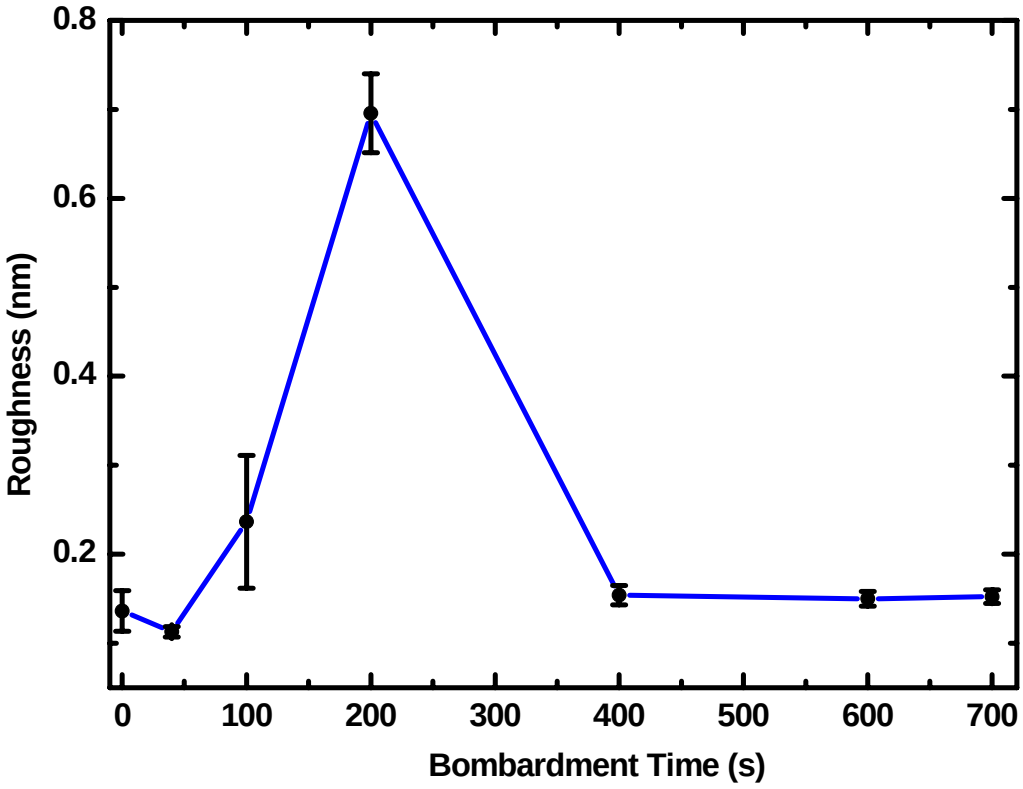

Figure 5.5 Tapping AFM mode measurements of roughness variance of $C_{32}H_{66}$ monolayer with increasing bombardment time.

5.4.4 Enhanced Stiffness of Thin Films by Bombardment

Tapping mode AFM can provide qualitative contrast on mechanical properties of the surface. Tomayo and Garcia [41] theoretically and experimentally demonstrated that the phase shift is not sensitive to stiff materials with larger Young's modulus, approximately

when E > ~1 GPa, even with energy dissipation involved. At present, we only can qualitatively obtain that the Young's modulus of parallel layer or the stiffness of both layers are smaller than 2 GPa before bombardment based on Figure 5.6. After 700 s bombardment as shown in Figure 5.7, such phase contrast can barely be differentiated. And both of these two layers had been stiffened with Young's modulus > ~1 GPa.

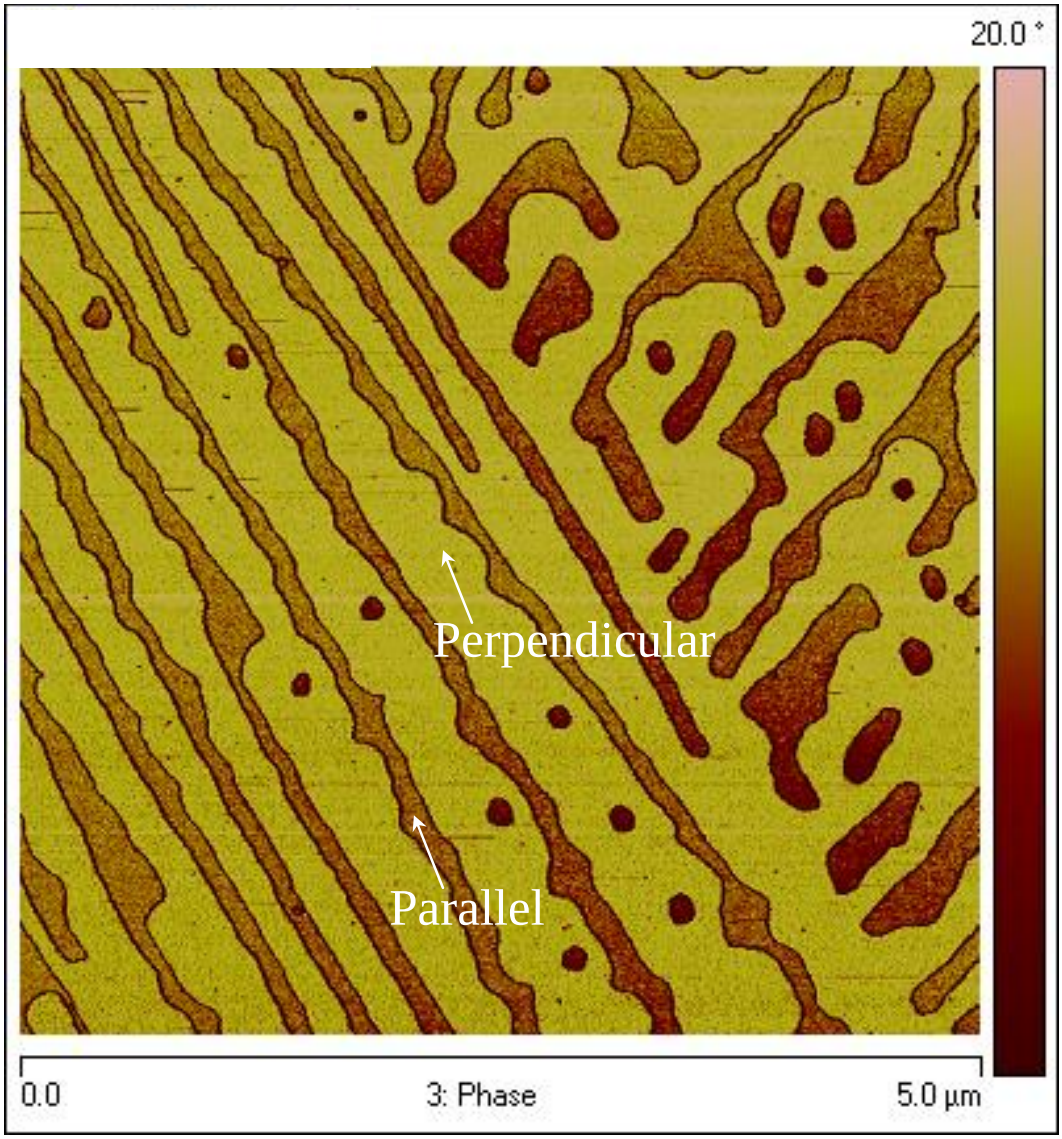

Figure 5.6 Phase contrast of tapping AFM to distinguish virgin (0 s) $C_{32}H_{66}$ perpendicular layer from parallel layer: darker region corresponds to $C_{32}H_{66}$ perpendicular layer; and brighter region corresponds to parallel layer.

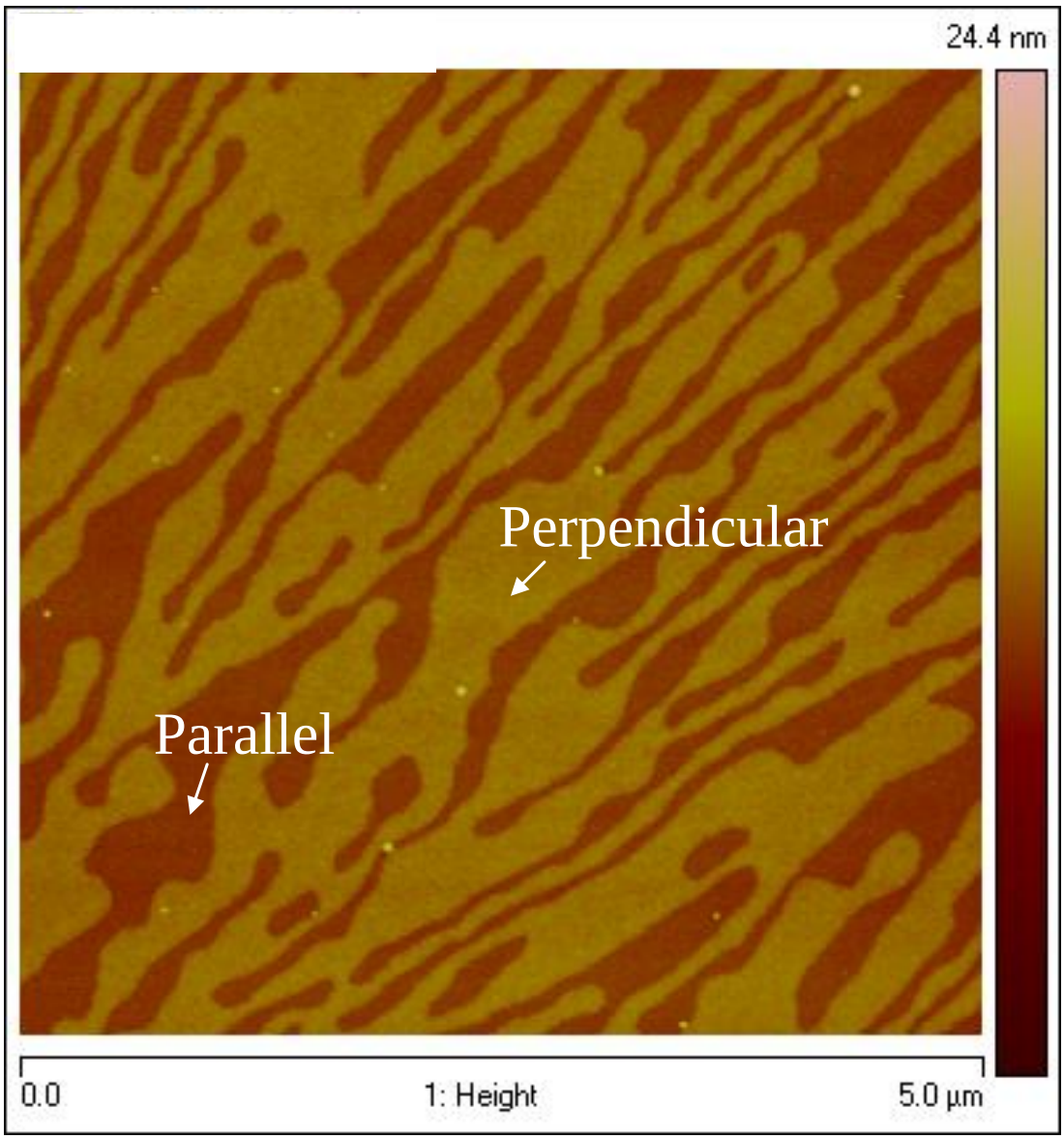

Figure 5.7 (Continued)

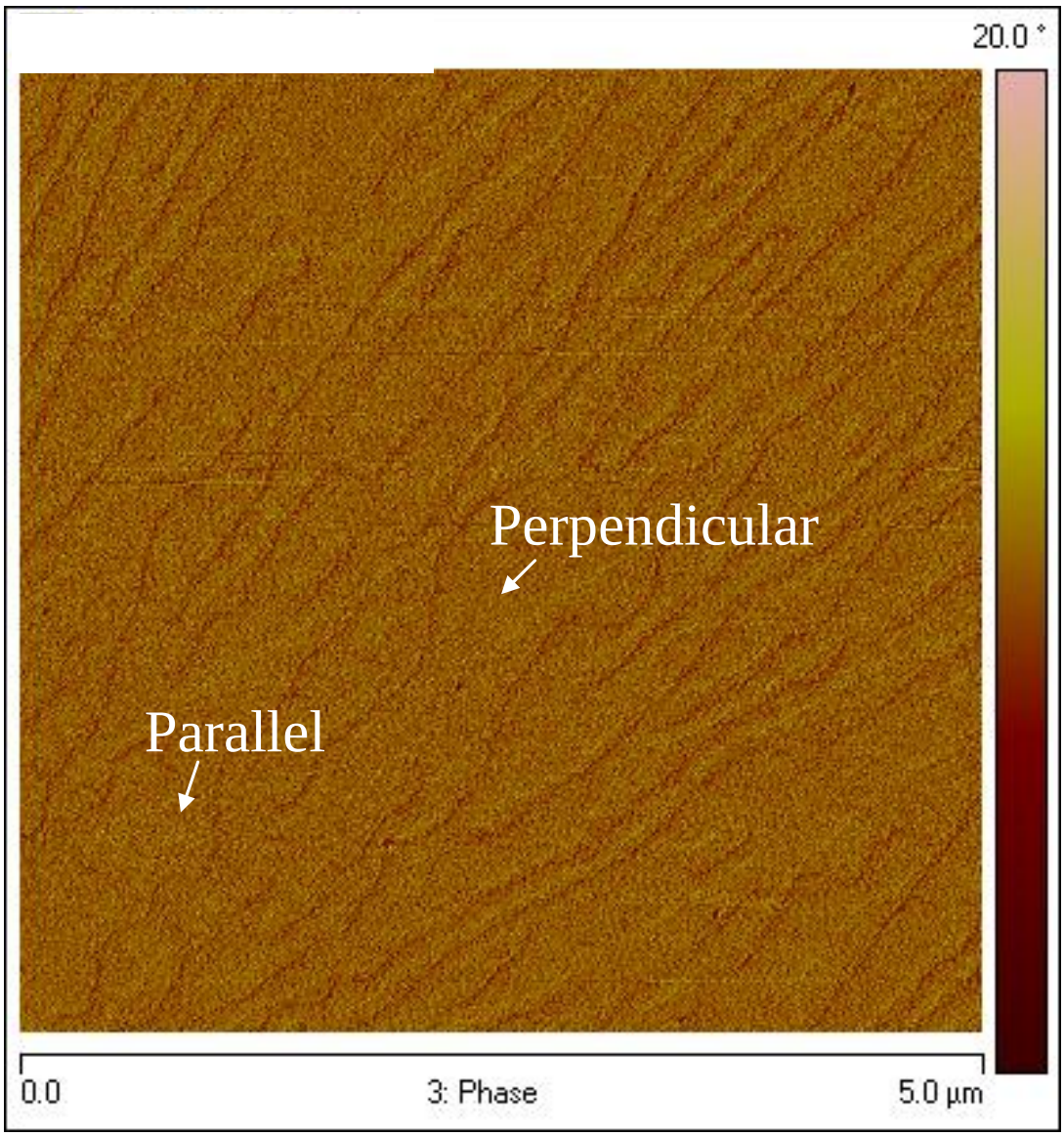

Figure 5.7 Topographic (top) and phase (bottom) images of $C_{32}H_{66}$ perpendicular and parallel layers after 700 s bombardment

To quantitatively measure the Young's moduli of both perpendicular and parallel layers [35-37, 58, 59], HarmoniX™ and force modulation can be both applied. HarmoniX™ mode [36, 60] has been developed as an advanced tapping mode carrying the capability to quantitatively obtain stiffness contrast on heterogeneous surface with high lateral resolution. This mode resolves the tip-sample contact in time domain through analyzing

the difference at higher harmonics on the broarder FFT spectrum of tip-sample interaction, which carry rich information about the mechanical property of the surface. To test the capability of HarmoniX^{TM} mode, as shown in Figure 5.7 we chose representative samples low-density polyethylene (LDPE) ~ 100 MPa, polystyrene (PS) ~ 2 GPa, polypropylene (PP) ~ 1.2 GPa, and mica ~ 50 GPa. The measured results from HarmoniX^{TM} are ~77 MPa, ~1.9 GPa, ~1.5 GPa and ~10.9 GPa, respectively. As to the measurement of mica, HamoniX^{TM} has lost its resolution for the sample with stiffness larger than 10 GPa[42].

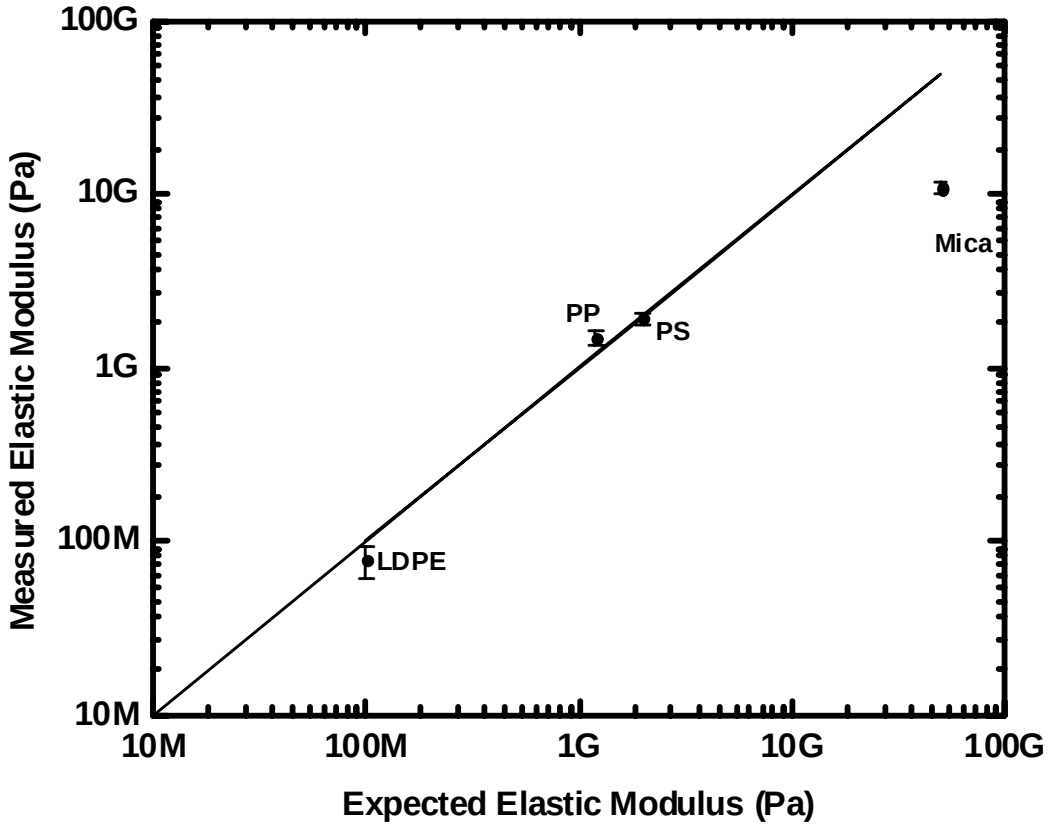

Figure 5.8 Large dynamic range nanomechanical measurements for several reference samples: Low-density polyethylene (LDPE) ~ 100 MPa, Polystyrene (PS) ~ 2 GPa, Polypropylene (PP) ~ 1.2 GPa and Mica ~ 50 GPa.

We applied HarmoniX^{TM} on measuring the Young's moduli of virgin perpendicular layer, virgin parallel layer and 700 s bombarded parallel layer. As shown in Figure 5.9, HarmoniX^{TM} mode can effectively separate these two differently oriented layers, with parallel layer of ~ 0.2 GPa softer than perpendicular of ~ 1.2 GPa. After 700 s bombardment, the parallel layer was stiffened to ~ 1.0 GPa and the perpendicular layer was stiffened to ~ 6.5 GPa.

Force modulation has been also applied to measure the stiffness of both layers. In this study, the excitation amplitude of the cantilever measured on a rigid sapphire (E ~ 435 GPa) and is 10.51 mV, which corresponds to 2.39 nm amplitude of the cantilever with calibrated sensitivity 227.5$\pm$2.0 nm/V. The diamond tip with calibrated spring constant 0.23 N/m was modulated at the frequency of 10.86 kHz and contact deflection with sample was set at 5.23 nN. Representative amplitude curves along scan direction with size 3 μm shown in Figure 5.10, the average amplitudes are 9.17 mV, 10.17 mV and 10.48 mV for 0 s bombarded perpendicular monolayer, 700 s bombarded perpendicular monolayer and SiO_2 layer, respectively. Because the Young's modulus of the SiO_2 is known as ~ 70 GPa, we can successfully obtain the constant value for HE_{tip} in Equation (5.5). Continuously using Equation (5.5), we can easily calculate the Young's moduli for virgin perpendicular and 700 s bombarded perpendicular monolayer are ~ 1.5 GPa and ~ 6.2 GPa, respectively. The measured value for the virgin perpendicular monolayer is in a good match with the value from HarmoniX^{TM} ~ 1.2 GPa in Figure 5.9. They both fall in the range as reported in literature [58, 61]. Through the proposed bombardment, we can enhance stiffness of the thin films up to five times.

Finally, we tested the possible effect of substrate under the very thin film during force modulation measurements. There is a well-known Bückle's rule that the substrate will not significantly affect the mechanical properties of the over layer if the indentation is less than 10% of the layer thickness [62, 63]. From Hertzian contact model with 52nm tip radius characterized by blind reconstruction from the image of porous aluminum (PA01, MicroMasch Inc.), the indented depth on sample was estimated about 0.45 nm which fall within the 10% of our measured perpendicular monolayer height of 4.5 nm. Same way

was used for the 700 s bombarded monolayer, because of the increased Young's modulus of the perpendicular monolayer the indented depth was only 0.18 nm within 10% of the monolayer height. Therefore, we can safely conclude that the substrate has negligible effect on the measured Young's modulus in this study.

Table 5.3 Young's Modulus of C32H66 Thin Films before and after bombardment

	Parallel Layer		Perpendicular Layer	
	0 s	700 s	0 s	700 s
Young's Modulus by HarmoniX (GPa)	~ 0.2	~ 1.0	~ 1.2	~ 6.5
Young's Modulus by Force Modulation (GPa)	N.A.	N.A.	~ 1.5	~ 6.2

5.5 CONCLUSIONS

Direct surface modification of a molecule monolayer has been implemented by selectively breaking C – H bonds of hydrocarbon chains to make carbon radicals leading to formation of C – C bonds between hydrocarbon chains with hyperthermal hydrogen projectile bombardment technology. The chemical property of the monolayer was preserved completely. Through studying morphological and mechanical properties, the bombarded monolayers have been proved to possess cross-linked molecular networks with well-defined smooth surface and the mechanical strength has been enhanced by about five times. A carbon-rich (like amorphous) layer may form in the hydrogen bombardment process. These advantages with this technique are very important in improving tribological properties of modern miniaturized systems and extending their life cycles. Wherein the enhanced stiffness has also been demonstrated on other polymeric systems such as butyl rubber and polylactic acid films, the Young's moduli of which were prompted by ~ 8 times through 30 minutes bombardment, respectively.

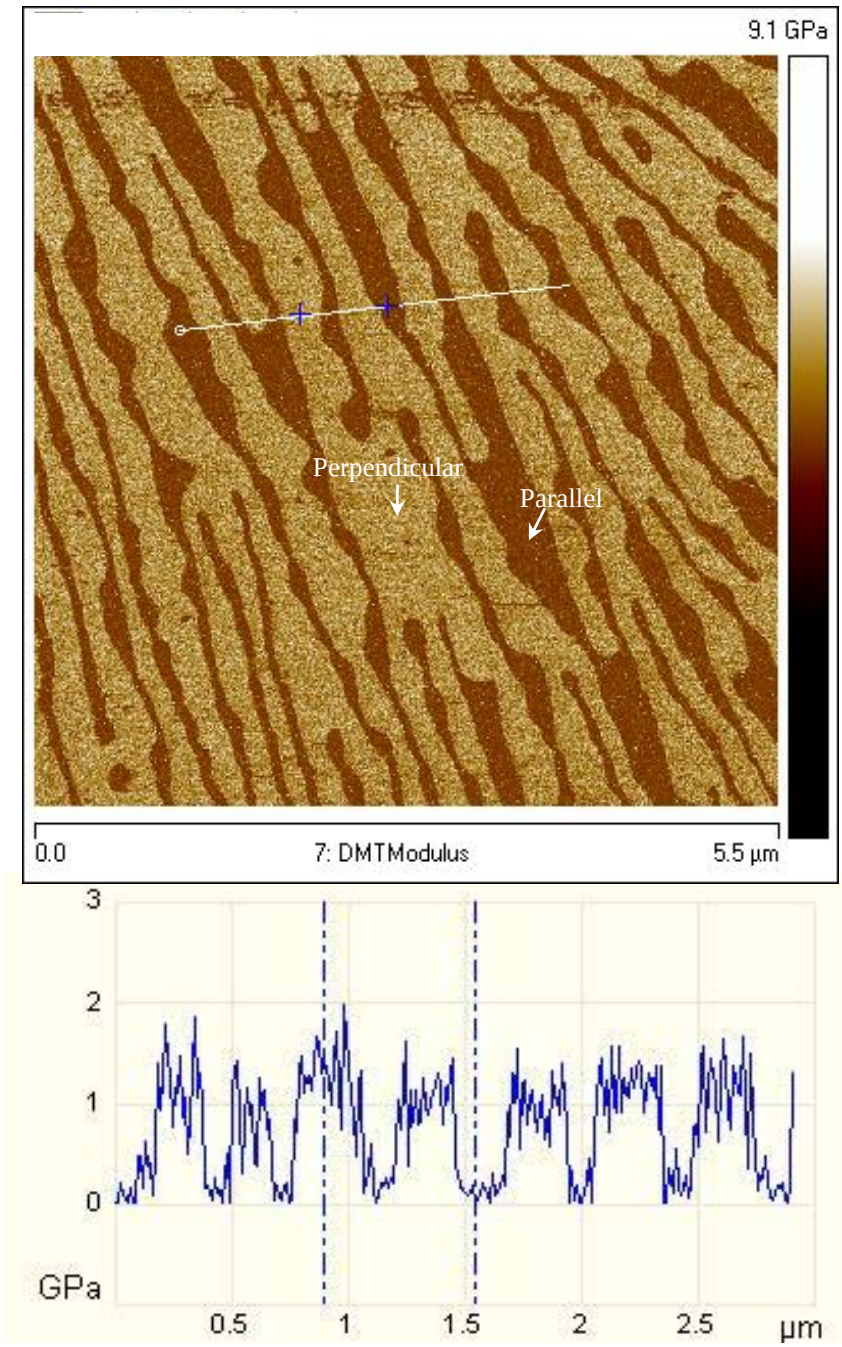

Figure 5.9 Nanomechanical mapping of parallel and perpendicular layers of virgin $C_{32}H_{66}$ thin film in the HarmoniX^{TM} Mode. Upper figure shows whole range of stiffness contrast; lower figure shows a section line profile, where perpendicular layer is ~ 1.2 GPa and parallel layer is ~ 0.2 GPa.

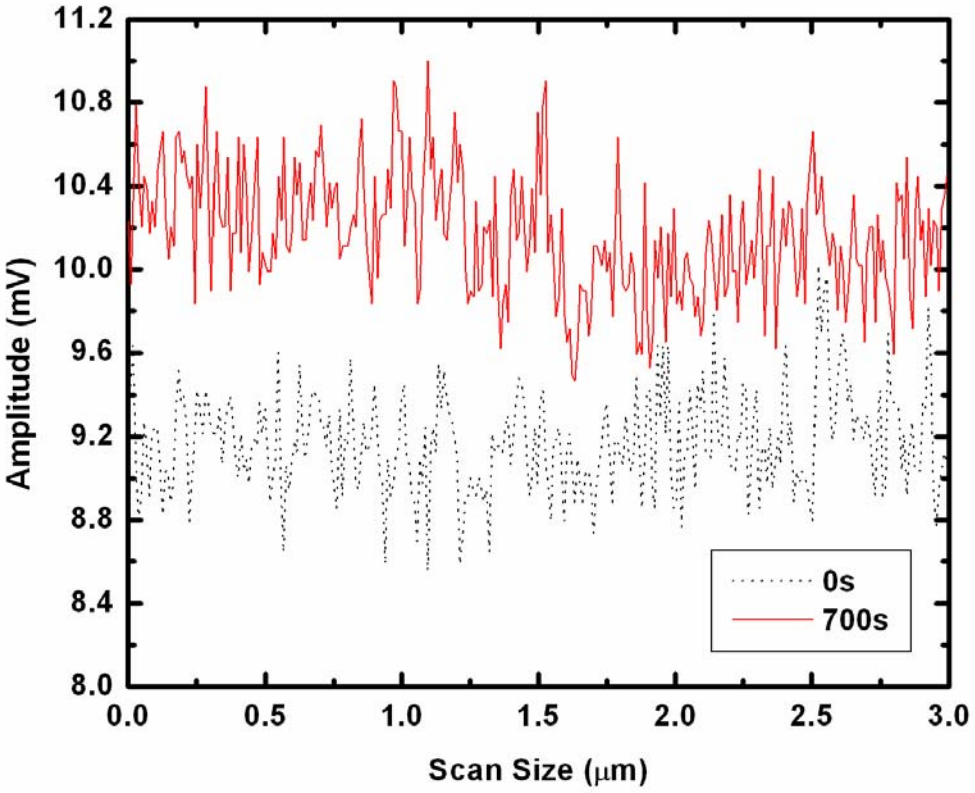

Figure 5.10 Amplitudes of cantilever in force modulation on virgin $C_{32}H_{66}$ perpendicular layer (dot) and 700 s bombarded perpendicular layer (dash) are 9.14 mV and 10.17 mV, respectively.

5.6 REFERENCES

1. Centrone, A., Penzo, E., Sharma, M., Myerson, J.W., Jackson, A.M., Marzari, N., and Stellacci, F., *The role of nanostructure in the wetting behavior of mixed-monolayer-protected metal nanoparticles*. Proceedings of the National Academy of Sciences of the United States of America, 2008. **105**(29): p. 9886-9891.
2. Caruso, F. and Mohwald, H., *Preparation and characterization of ordered nanoparticle and polymer composite multilayers on colloids*. Langmuir, 1999. **15**(23): p. 8276-8281.
3. Muntele, C., *Molecular random-access memory cell demonstrated*. Mrs Bulletin, 2001. **26**(6): p. 432-432.

4. Chen, Y., Jung, G.Y., Ohlberg, D.A.A., Li, X.M., Stewart, D.R., Jeppesen, J.O., Nielsen, K.A., Stoddart, J.F., and Williams, R.S., *Nanoscale molecular-switch crossbar circuits*. Nanotechnology, 2003. **14**(4): p. 462-468.
5. Nalwa, H.S. and Kakuta, A., *Organometallic Langmuir-Blodgett-Films for Electronics and Photonics*. Applied Organometallic Chemistry, 1992. **6**(8): p. 645-678.
6. Talham, D.R., Yamamoto, T., and Meisel, M.W., *Langmuir-Blodgett films of molecular organic materials*. Journal of Physics-Condensed Matter, 2008. **20**(18): p. 184006.
7. Yoshida, S., Ono, T., and Esashi, M., *Conductive polymer patterned media fabricated by diblock copolymer lithography for scanning multiprobe data storage*. Nanotechnology, 2008. **19**(47): p. 475302.
8. Yoshida, S., Ono, T., Oi, S., and Esashi, M., *Reversible electrical modification on conductive polymer for proximity probe data storage*. Nanotechnology, 2005. **16**(11): p. 2516-2520.
9. Kepley, L.J., Crooks, R.M., and Ricco, A.J., *Selective Surface Acoustic Wave-Based Organophosphonate Chemical Sensor Employing a Self-Assembled Composite Monolayer - a New Paradigm for Sensor Design*. Analytical Chemistry, 1992. **64**(24): p. 3191-3193.
10. Kang, T., Hong, S.R., Moon, J., Oh, S., and Yi, J., *Fabrication of reusable sensor for detection of Cu2+ in an aqueous solution using a self-assembled monolayer with surface plasmon resonance spectroscopy*. Chemical Communications, 2005(29): p. 3721-3723.
11. Parnell, A.J., Martin, S.J., Dang, C.C., Geoghegan, M., Jones, R.A.L., Crook, C.J., Howse, J.R., and Ryan, A.J., *Synthesis, characterization and swelling behaviour of poly(methacrylic acid) brushes synthesized using atom transfer radical polymerization*. Polymer, 2009. **50**(4): p. 1005-1014.
12. Ruckenstein, E. and Li, Z.F., *Surface modification and functionalization through the self-assembled monolayer and graft polymerization*. Advances in Colloid and Interface Science, 2005. **113**(1): p. 43-63.
13. Hyun, J. and Chilkoti, A., *Surface-initiated free radical polymerization of polystyrene micropatterns on a self-assembled monolayer on gold*. Macromolecules, 2001. **34**(16): p. 5644-5652.
14. Zhao, B. and Brittain, W.J., *Synthesis of tethered polystyrene-block-poly(methyl methacrylate) monolayer on a silicate substrate by sequential carbocationic polymerization and atom transfer radical polymerization*. Journal of the American Chemical Society, 1999. **121**(14): p. 3557-3558.
15. Lemieux, M., Minko, S., Usov, D., Stamm, M., and Tsukruk, V.V., *Direct measurement of thermoelastic properties of glassy and rubbery polymer brush nanolayers grown by "grafting-from" approach*. Langmuir, 2003. **19**(15): p. 6126-6134.
16. Lau, W.M., *Ion beam techniques for functionalization of polymer surfaces*. Nuclear Instruments & Methods in Physics Research Section B-Beam Interactions with Materials and Atoms, 1997. **131**(1-4): p. 341-349.

17. Andersen, C.A., Roden, H.J., and Robinson, C.F., *Negative Ion Bombardment of Insulators to Alleviate Surface Charge-Up*. Journal of Applied Physics, 1969. **40**(8): p. 3419-3420.
18. Arnold, J.C. and Sawin, H.H., *Charging of Pattern Features during Plasma-Etching*. Journal of Applied Physics, 1991. **70**(10): p. 5314-5317.
19. Kenney, J.A. and Hwang, G.S., *Prediction of stochastic behavior in differential charging of nanopatterned dielectric surfaces during plasma processing*. Journal of Applied Physics, 2007. **101**(4): p. 044307.
20. Chang, J.P. and Coburn, J.W., *Plasma-surface interactions*. Journal of Vacuum Science & Technology A, 2003. **21**(5): p. S145-S151.
21. Abatchev, M.K. and Murali, S.K., *Differential surface-charge-induced damage of dielectrics and leakage kinetics during plasma processing*. Electrochemical and Solid State Letters, 2006. **9**(1): p. F1-F4.
22. Linder, B.P. and Cheung, N.W., *Plasma immersion ion implantation with dielectric substrates*. Ieee Transactions on Plasma Science, 1996. **24**(6): p. 1383-1388.
23. Lau, W.M., Zheng, Z., Wang, Y.H., Luo, Y., Xi, L., Wong, K.W., and Wong, K.Y., *Cross-linking organic semiconducting molecules by preferential C-H cleavage via "chemistry with a tiny hammer"*. Canadian Journal of Chemistry-Revue Canadienne De Chimie, 2007. **85**(10): p. 859-865.
24. Zheng, Z., Xu, X.D., Fan, X.L., Lau, W.M., and Kwok, R.W.M., *Ultrathin polymer film formation by collision-induced cross-linking of adsorbed organic molecules with hyperthermal protons*. Journal of the American Chemical Society, 2004. **126**(39): p. 12336-12342.
25. Sefler, G.A., Du, Q., Miranda, P.B., and Shen, Y.R., *Surface Crystallization of Liquid N-Alkanes and Alcohol Monolayers Studied by Surface Vibrational Spectroscopy*. Chemical Physics Letters, 1995. **235**(3-4): p. 347-354.
26. Wu, X.Z., Sirota, E.B., Sinha, S.K., Ocko, B.M., and Deutsch, M., *Surface Crystallization of Liquid Normal-Alkanes*. Physical Review Letters, 1993. **70**(7): p. 958-961.
27. Schollmeyer, H., Struth, B., and Riegler, H., *Long chain n-alkanes at SiO2/air interfaces: Molecular ordering, annealing, and surface freezing of triacontane in the case of excess and submonolayer coverage*. Langmuir, 2003. **19**(12): p. 5042-5051.
28. Merkl, C., Pfohl, T., and Riegler, H., *Influence of the molecular ordering on the wetting of SiO2/air interfaces by alkanes*. Physical Review Letters, 1997. **79**(23): p. 4625-4628.
29. Yamamoto, T., Nozaki, K., Yamaguchi, A., and Urakami, N., *Molecular simulation of crystallization in n-alkane ultrathin films: Effects of film thickness and substrate attraction*. Journal of Chemical Physics, 2007. **127**(15): p. 154704.
30. Herwig, K.W., Matthies, B., and Taub, H., *Solvent Effects on the Monolayer Structure of Long N-Alkane Molecules Adsorbed on Graphite*. Physical Review Letters, 1995. **75**(17): p. 3154-3157.
31. Marti, O., Ribi, H.O., Drake, B., Albrecht, T.R., Quate, C.F., and Hansma, P.K., *Atomic Force Microscopy of an Organic Monolayer*. Science, 1988. **239**(4835): p. 50-52.

32. Morigaki, K., Schonherr, H., Frank, C.W., and Knoll, W., *Photolithographic polymerization of diacetylene-containing phospholipid bilayers studied by multimode atomic force microscopy*. Langmuir, 2003. **19**(17): p. 6994-7002.
33. Oncins, G., Vericat, C., and Sanz, F., *Mechanical properties of alkanethiol monolayers studied by force spectroscopy*. Journal of Chemical Physics, 2008. **128**(4): p. 044701.
34. Zhong, Q., Inniss, D., Kjoller, K., and Elings, V.B., *Fractured Polymer Silica Fiber Surface Studied by Tapping Mode Atomic-Force Microscopy*. Surface Science, 1993. **290**(1-2): p. L688-L692.
35. Dong, M.D., Husale, S., and Sahin, O., *Determination of protein structural flexibility by microsecond force spectroscopy*. Nature Nanotechnology, 2009. **4**(8): p. 514-517.
36. Sahin, O., Magonov, S., Su, C., Quate, C.F., and Solgaard, O., *An atomic force microscope tip designed to measure time-varying nanomechanical forces*. Nature Nanotechnology, 2007. **2**(8): p. 507-514.
37. Radmacher, M., Tilmann, R.W., and Gaub, H.E., *Imaging Viscoelasticity by Force Modulation with the Atomic Force Microscope*. Biophysical Journal, 1993. **64**(3): p. 735-742.
38. Briggs, D., *Surface Analysis of Polymers by XPS and Static SIMS*. 1998: Cambridge University press.
39. Magonov, S.N., Elings, V., and Whangbo, M.H., *Phase imaging and stiffness in tapping-mode atomic force microscopy*. Surface Science, 1997. **375**(2-3): p. L385-L391.
40. Magonov, S.N. and Reneker, D.H., *Characterization of polymer surfaces with atomic force microscopy*. Annual Review of Materials Science, 1997. **27**: p. 175-222.
41. Tamayo, J. and Garcia, R., *Effects of elastic and inelastic interactions on phase contrast images in tapping-mode scanning force microscopy*. Applied Physics Letters, 1997. **71**(16): p. 2394-2396.
42. Sahin, O. and Erina, N., *High-resolution and large dynamic range nanomechanical mapping in tapping-mode atomic force microscopy*. Nanotechnology, 2008. **19**(44): p. 445717.
43. Lau, W.M. and Kwok, R.W.M., *Engineering surface reactions with polyatomic ions*. International Journal of Mass Spectrometry, 1998. **174**(1-3): p. 245-252.
44. Xi, L., Zheng, Z., Lam, N.S., Grizzi, O., and Lau, W.M., *Effects of hyperthermal proton bombardment on alkanethiol self-assembled monolayer on Au(111)*. Applied Surface Science, 2007. **254**(1): p. 113-115.
45. Alexander, S., Hellemans, L., Marti, O., Schneir, J., Elings, V., Hansma, P.K., Longmire, M., and Gurley, J., *An Atomic-Resolution Atomic-Force Microscope Implemented Using an Optical-Lever*. Journal of Applied Physics, 1989. **65**(1): p. 164-167.
46. Meyer, G. and Amer, N.M., *Novel Optical Approach to Atomic Force Microscopy*. Applied Physics Letters, 1988. **53**(12): p. 1045-1047.
47. Hutter, J.L. and Bechhoefer, J., *Calibration of Atomic-Force Microscope Tips (Vol 64, Pg 1868, 1993)*. Review of Scientific Instruments, 1993. **64**(11): p. 3342-3342.

48. Volkmann, U.G., Pino, M., Altamirano, L.A., Taub, H., and Hansen, F.Y., *High-resolution ellipsometric study of an n-alkane film, dotriacontane, adsorbed on a SiO2 surface*. Journal of Chemical Physics, 2002. **116**(5): p. 2107-2115.
49. Holzwarth, A., Leporatti, S., and Riegler, H., *Molecular ordering and domain morphology of molecularly thin triacontane films at SiO2/air interfaces*. Europhysics Letters, 2000. **52**(6): p. 653-659.
50. Mo, H., Trogisch, S., Taub, H., Ehrlich, S.N., Volkmann, U.G., Hansen, F.Y., and Pino, M., *Structure and growth of dotriacontane films on SiO2 and Ag(111) surfaces: synchrotron X-ray scattering and molecular dynamics simulations*. Physica Status Solidi a-Applied Research, 2004. **201**(10): p. 2375-2380.
51. Bai, M., Trogisch, S., Magonov, S., and Taub, H., *Explanation and correction of false step heights in amplitude modulation atomic force microscopy measurements on alkane films*. Ultramicroscopy, 2008. **108**(9): p. 946-952.
52. Sirringhaus, H., Tessler, N., and Friend, R.H., *Integrated, high-mobility polymer field-effect transistors driving polymer light-emitting diodes*. Synthetic Metals, 1999. **102**(1-3): p. 857-860.
53. Trogisch, S., Simpson, M.J., Taub, H., Volkmann, U.G., Pino, M., and Hansen, F.Y., *Atomic force microscopy measurements of topography and friction on dotriacontane films adsorbed on a SiO2 surface*. Journal of Chemical Physics, 2005. **123**(15): p. 154703.
54. Bhushan, B., *Handbook of Micro/Nano Tribology*. 2nd ed, ed. B. Bhushan. 1999: Boca Raton: CRC Press.
55. Hartig, M., Chi, L.F., Liu, X.D., and Fuchs, H., *Dependence of the measured monolayer height on applied forces in scanning force microscopy*. Thin Solid Films, 1998. **329**: p. 262-267.
56. Simpson, G.J., Sedin, D.L., and Rowlen, K.L., *Surface roughness by contact versus tapping mode atomic force microscopy*. Langmuir, 1999. **15**(4): p. 1429-1434.
57. Tsukruk, V.V., Luzinov, I., and Julthongpiput, D., *Sticky molecular surfaces: Epoxysilane self-assembled monolayers*. Langmuir, 1999. **15**(9): p. 3029-3032.
58. Price, W.J., Leigh, S.A., Hsu, S.M., Patten, T.E., and Liu, G.Y., *Measuring the size dependence of Young's modulus using force modulation atomic force microscopy*. Journal of Physical Chemistry A, 2006. **110**(4): p. 1382-1388.
59. Overney, R.M., Meyer, E., Frommer, J., Guntherodt, H.J., Fujihira, M., Takano, H., and Gotoh, Y., *Force Microscopy Study of Friction and Elastic Compliance of Phase-Separated Organic Thin-Films*. Langmuir, 1994. **10**(4): p. 1281-1286.
60. Solares, S.D. and Holscher, H., *Numerical analysis of dynamic force spectroscopy using the torsional harmonic cantilever*. Nanotechnology, 2010. **21**(7): p. 075702.
61. DelRio, F.W., Jaye, C., Fischer, D.A., and Cook, R.F., *Elastic and adhesive properties of alkanethiol self-assembled monolayers on gold*. Applied Physics Letters, 2009. **94**(13): p. 131909.
62. Fischer-Cripps, A.C., *A review of analysis methods for sub-micron indentation testing*. Vacuum, 2000. **58**(4): p. 569-585.
63. Clifford, C.A. and Seah, M.P., *Modelling of nanomechanical nanoindentation measurements using an AFM or nanoindenter for compliant layers on stiffer substrates*. Nanotechnology, 2006. **17**(21): p. 5283-5292.

CHAPTER 6
SUMMARY AND FUTURE WORK

6.1 SUMMARY

Main motivation of this thesis work is to better probe the surface properties at the nanometer scale. Both of theoretical and experimental studies have demonstrated several improvements in development and application of AFM.

Chapter 2 and Chapter 3 demonstrate the calibration and optimization of sensitivity at normal direction for both of static and dynamic modes. First, for the static AFM mode as applied in liquid environment, a theoretical model has been developed for the detection sensitivity. The enhancement or degradation of AFM sensitivity in liquid environment as compared with sensitivity in air is determined by the coupling effects of laser spot size, spot location, and refractive indices of mediums which laser beam is transmitted through. In most of liquid applications, such sensitivity is enhanced. However, if low refractive index mediums such as gas are involved, the sensitivity may be degraded depending on the spot location and spot size. Based on the proposed model, the sensitivity as calibrated by force curve in air can be applied to predict the sensitivity in liquid. This is important for experiment designs and sensitivity improvement in advanced applications, including single molecule force, cell – cell interaction, interface & colloid force, confined liquid at nanoscale, et al.

However, the detection sensitivity from force curve in static mode is can not be applied as the sensitivity on dynamic AFM modes including tapping mode and higher – order mode. This is mainly due to that the optical – lever AFM is detecting the slope of the cantilever rather than its end deflection. The slope of the cantilever is further dependent on beam shape of the cantilever in vibration. Chapter 3 provides the detailed discussion on optimization and calibration of sensitivity in dynamic mode, which is completely affected by spot size, spot location, and tip – sample interaction in vibrating process. Higher – order AFM mode is more immune to the effect of tip – sample interaction and

has higher sensitivity and stability. This can partially explain the reason that higher – order AFM mode can provide more stable and accurate image. We established a method to calibrate the sensitivity of higher – order AFM mode.

Different from calibration of the sensitivity at normal direction, the sensitivity at lateral direction is difficulty to be implemented, in that there has not been any standard process to introduce exactly known displacement at lateral direction. The method in Chapter 4 applies a T – shape cantilever, with its tip offset by a distance from its main axis, in lateral contact scanning to benefit the simplification and accuracy of measurement of friction coefficient. We discussed the basic principle, algorithm, and its implementation on a chemical force microscopy.

In Chapter 5, the effects of hydrogen bombardment on surface properties of alkane thin films were studied. We discussed the excellence of applying AFM to characterize the bombardment process and relevant results can explain the principle of hydrogen bombardment. The study mainly focused on tapping mode, force modulation mode and HarmoniX mode for measuring stiffness of thin films before and after bombardment. Successful results demonstrate the induced cross-linking between alkane molecules by bombardment and the Young's modulus of thin film is increased by 5 times as well as the smooth surface is retained.

6.2 Thesis Contributions

The contributions of this thesis are summarized as below:

- Based on a developed model, the sensitivity as calibrated by force curve in ambient can be applied for the sensitivity calibration in liquid environment, although they are different. To improve the detection sensitivity in biological applications, operation environment, laser spot size and laser spot location should be integrated for consideration.
- The optimization of the sensitivity in dynamic mode has been discussed, which is well beneficial for resolving details of AFM tip – sample interactions. AFM dynamic sensitivity is dependent on the significance of tip – sample interaction as compared to

the cantilever stiffness. An important conclusion has been obtained that, when laser spot is located at normalized position $x/L_{eff} = 0.6$, the sensitivity is same to the sensitivity from force curve and is least affected by the tip – sample interaction. It is critical for calibration of dynamic sensitivity at different resonance modes. The $x/L_{eff} = 0.6$ is also useful for calibration of AFM spring constant based on the thermal method, which utilizes the spectrum information at the vicinity of tapping frequency.

- New nanotribology method based on T – shape cantilever has been developed to bypass the difficulty of calibrating lateral spring constant and lateral sensitivity. T – shape cantilever as applied in lateral scanning mode can decouple the effect of normal load from that of lateral load on the lateral signal. Two steps of individual calibrations save conventional efforts relying on complex accessories and procedures. It has been applied as chemical force microscopy to quantitatively distinguish chemical groups at nanoscale.

6.3 FUTURE WORK

AFM has been becoming one of most powerful tools to study phenomena at nanometer scale. The present work on AFM sensitivity can be applied to: (1) optimize and calibrate the sensitivity of AFM in applications, and therefore provide more accurate force information between tip and sample. We will apply these results in explanation of surface properties, with more focus on higher – order AFM mode; (2) optimize the design of nanomechanical cantilever sensors, which are being increasingly developed for measuring minute weights, pH value, hydrogen concentration, and so on. The relevant methodologies are also applicable for designing MEMS beam system as accelerator in aerospace and automotives.

Our lateral friction force microscopy based on T – shape cantilever is simple and accurate. It has been successfully demonstrated on chemical force microscopy to distinguish chemical groups. We are applying this method to study tip – sample interaction through modifying the cantilever tip with specified chemical group. Furthermore, with the

recently increasing interests on nanotribology, this method could be extended in lubricate coating on MEMS/NEMS devices, friction force to move nanotube on substrates, and tribological properties of nanowire / nanobelt / nanorod / nanosheet and even graphene.

Curriculum Vitae

Name: Yu Liu

Post-secondary Education and Degrees:

The University of Western Ontario
London, Canada
2006-2010 Ph.D.

Kyungpook National University
Daegu, China
2003-2005 M.E.

Harbin Institute of Technology
Harbin, China
1999-2003 B.E.

Honours and Awards:

Ontario Graduate Scholarship
2009-2010

Related Work Experience

Teaching Assistant / Research Assistant
The University of Western Ontario
2006-2010

Facility Maintenance and Measurement Equipment Engineer
2005-2006

Research Assistant
Kyungpook National University
2003-2005

Publications

Articles published or accepted in refereed journals

1. Y. Liu, K.M. Leung, H.Y. Nie, W.M. Lau, and J. Yang, "A New AFM Nanotribology Method Using a T – Shape Cantilever With An Off-Axis Tip For Friction Coefficient Measurement with Minimized Abbé Error", Tribology Letters, 2010.
2. X.L. Jin, X.P. Fan, Z.B. Liu, Z.Q. Kuang, J. Cheng, J. Chen, Y. Liu, and J. Yang,

"Measurement of High Sensitivity and Low Crosstalk of Zero Space Microlens for 2.8mm Pitch Active Pixel Sensor", *IEEE Transactions on Electron Devices*, 57, 415–421, 2010.

3. Y. Liu, Q.Q. Guo, H.Y. Nie, W.M. Lau and J. Yang, "Optimization and Calibration of Atomic Force Microscopy Sensitivity in Terms of Tip-Sample Interactions in High-order Dynamic Atomic Force Microscopy", *Journal of Applied Physics*, 106, 124507, 2009.
4. S. Naeem, Y. Liu, H.Y. Nie, W. M. Lau and J. Yang, "Revisiting AFM Force Spectroscopy Sensitivity for Single Molecule Studies", *Journal of Applied Physics*, 104, 114504, 2008. (Selected by *Virtual Journal of Nanoscale Science & Technology*, 24, 2008; Also cited by *Virtual Journals of Biological Physics Research*, 16, issue 12, 2008)
5. Y. Liu and J. Yang, "Coupling Effects of Refractive Index Discontinuity, Spot Size and Spot Location on the Deflection Sensitivity of Optical-Lever Based Atomic Force Microscopy", *Nanotechnology*, 19, 235501, 2008. (highlighted on http://nanotechweb.org/cws/article/lab/34399, May 28, 2008)
6. Y. Liu and J. Yang, "Higher-order lattice Boltzmann Simulation of Energy Conversion of Electrokinetic Nanobatteries", *The European Physical Journal Special Topics*, 171, 99–104, 2009.
7. M. Liu, Y. Liu, Q.Q. Guo and J. Yang, "Modeling of Electroosmotic Pumping of Nonconducting Liquids and Biofluids by a Two-phase Flow Method", *Journal of Electroanalytical Chemistry*, 636, 86–92, 2009
8. Q.Q. Guo, Y. Liu and J. Yang, "Design of a Relaying Electroosmosis Pump Driven by Low-Voltage DC", *Microsystem Technologies*, 2009, DOI 10.1007/s00542-009-0840-3.
9. J.L Zhang, Y. Liu, J.F. Zhang and J. Yang, "Study of force-dependent and time-dependent transition of secondary flow in a rotating straight channel by lattice Boltzmann method", *Physica A*, 388, Issue 4, 288, 2009.
10. Y. Liu and J. Yang, "Where there is a valley, there is a peak: Study of ion size and image effects on nano-electroosmotic pumping", *Journal of Chemical Physics*, 128, 174708, 2008. (Selected by Virtual Journal of Nanoscale Science &

Technology, May 19, 2008).

11. M. Liu, J. L. Zhang, Y. Liu, W. M. Lau and J. Yang "Modeling of Flow Burst, Flow Timing in Lab-on-a-CD Systems and its Application in Digital Chemical Analysis", *Chemical Engineering and Technology*, Vol. 31, No. 9, 1–9, 2008.
12. J. L. Zhang, Y. Liu, M. Liu, W. M. Lau and J. Yang "Modeling of Nanotube Based Nanopumps, Nanoactuators and Nanooscillators Using Lattice Boltzmann Method", *Journal of Computational and Theoretical Nanoscience*, Vol. 5, 1-5, 2008.
13. Y. Liu, M. Liu, W. M. Lau and J. Yang, "Ion Size and Image Effect on Electrokinetic Flows", *Langmuir*, Vol.24, 2884-2891, 2008.

Articles Submitted

1. Y. Liu, D.Q. Yang, H.Y. Nie, W.M. Lau, and J. Yang, "Study Of Hydrogen Bombardment Induced Molecular Cross-Linking within Alkane Thin Films", Submitted, 2010.

Papers published in conference proceedings

1. Y. Liu, Q. Guo and J. Yang, "Meso – Level Modeling of Nanoscale Water Battery", CFD Society of Canada 18th Annual Conference, London, Canada, May 18 – 19, 2010.
2. Y. Liu, H.Y. Nie, D.Q. Yang, C. Bonduelle, E. Gillies, W.M. Lau and J. Yang, "Flexural and Torsional Atomic Force Microscopy for Imaging Copolymer and Elastomer Blends", in 6th Annual Student Colloquium during the 176th Technical Meeting & Rubber Expo of the Rubber Division ASC 100th Anniversary, Pittsburgh, Pennsylvania, USA, October 13 – 15, 2009.
3. Y. Liu, D.Q. Yang, H.Y. Nie, W.M. Lau and J. Yang, "Nanoscale Stiffness, Adhesion and Friction of Lubricant Thin Film Engineered by Low-energy Hydrogen Ion Beam Bombardment", in 92nd Canadian Chemistry Conference, Hamilton, Ontario, Canada, May 30 – June 3, 2009.
4. S. Karamdoust, Y. Liu, E.R. Gillies, J. Yang, G. Davidson, G. Stojcevic and W.M. Lau, "Towards cationic antimicrobial surfaces via hyperthermal hydrogen

bombardment”, in 92nd Canadian Chemistry Conference, Hamilton, Ontario, Canada, May 30 – June 3, 2009.

5. Y. Liu, Q.Q. Guo and J. Yang, “Modeling and Optimal Design of an In-vivo Low-voltage DC Electrokinetic Pump”, in Canadian Society for Mechanical Engineering Forum 2008, Ottawa, Ontario, Canada, June 5-8, 2008.
6. Y. Liu and J. Yang, "Modeling of nanochannel based electricity generator", 16th discrete simulation of fluid dynamics: micro, nano and multiscale physics for emerging techniques, Calgary, Alberta, Canada, July 23–27, 2007.
7. J. Zhang, Y. Liu, M. Liu and J. Yang, "Modeling of nanofluidics-based nanoresonators", 16th discrete simulation of fluid dynamics: micro, nano and multiscale physics for emerging techniques, Calgary, Alberta, Canada, July 23–27, 2007.
8. J. Zhang, Y. Liu, M. Liu and J. Yang, "Transition of secondary flow in a rotating straight microchannel in a MEMS system", 16th discrete simulation of fluid dynamics: micro, nano and multiscale physics for emerging techniques, Calgary, Alberta, Canada, July 23–27, 2007.
9. J. Yang, Y. Liu, "Modeling electrokinetic battery made of nanochannel array", ChinaNano2007, Beijing, China, June 4 - 6, 2007.